Unsteady Boundary Layer Transition Measurements with Infrared Thermography

Development of Improved Measurement Schemes

by

Christoph Mertens

to obtain the degree of Master of Science
at the Delft University of Technology,
to be defended publicly on Tuesday December 11, 2018 at 09:30 AM.

Student number:	4633547	
Project duration:	March 1, 2018 – November 30, 2018	
Thesis committee:	Dr. ir. B. W. van Oudheusden,	TU Delft (Chair)
	Dr. ir. F. F. J. Schrijer,	TU Delft
	Dr. F. Avallone,	TU Delft
	Dr. habil. A. D. Gardner,	DLR Göttingen
	Prof. M. Raffel,	DLR Göttingen

TU Delft

DLR

Abstract

The boundary layer transition location is a crucial design parameter in aerodynamics. The computational prediction of boundary layer transition in engineering applications is typically based on empirical models. These models require experimental measurements for calibration and validation purposes. For unsteady aerodynamic processes, the range of suitable boundary layer transition measurement techniques is traditionally limited to fast-response discrete sensor techniques, e.g. hot-film anemometry. Introduced in 2014, differential infrared thermography is an alternative approach to measuring unsteady boundary layer transition using thermal images acquired with an infrared camera. The application of this optical measurement technique reduces the experimental effort, but problems emerge when the temperature response of the surface under investigation is slower than the aerodynamic unsteadiness. The idea of differential infrared thermography is to evade this problem by subtracting subsequent thermographs and accrediting the largest difference to the moving boundary layer transition location. The working principle of the technique has been demonstrated in various experimental setups. In a heat transfer simulation, it has been shown that the image separation time between the subtracted thermographs should be as small as possible to avoid systematic measurement errors. An experimental validation of these results is performed in the present study, conducted at the DLR in Göttingen. In this study, the infrared radiation from a pitching airfoil model suction surface in the wind tunnel at $Ma = 0.15$ and $Re = 1 \cdot 10^6$ is measured with an infrared camera. The pitching frequencies f and amplitudes α_1 are varied in a range from $f = 0.25\,\text{Hz}$ to $f = 8\,\text{Hz}$ and $\alpha_1 = 1°$ to $\alpha_1 = 8°$ to study their effects on the boundary layer transition measurements. The differential infrared thermography technique is applied with several different image separation time steps to confirm the findings of the heat transfer simulation. The time step size is optimized as a compromise between the measurement error and the signal strength. In the next step, two alternative boundary layer transition measurement schemes using infrared thermography are developed, based on a quasi-steady model and a heat transfer simulation result. The first newly developed approach involves the automated selection of the appropriate image separation time step for each data point over the motion period when applying differential infrared thermography. This adaptive approach outperforms the conventional fixed time step approach when applied to experimental data from the wind tunnel test. The second newly developed approach is termed local infrared thermography. When analyzing the thermographic measurement results at fixed model locations, the extraction of the extrema of the measured radiation signal yields instants of the motion period that correlate with the occurrence of boundary layer transition. It is demonstrated that the local infrared thermography approach can be extended to measuring two-dimensional boundary layer transition fronts. The analysis of these results provides insight into the origins of the differences between the results of differential infrared thermography and the reference measurements of the unsteady boundary layer transition location with a fast-response technique.

Contents

List of Figures

List of Tables

Nomenclature

Latin symbols

Symbol	Unit	Description
a	m/s	Speed of sound
A	m^2	Surface area
b	m	Span width
c	m	Chord length
C	-	Certainty parameter
C_f	-	Skin friction coefficient
C_ℓ	-	Lift coefficient
C_p	-	Surface pressure coefficient
C_P	J/(kg K)	Heat capacity
D	m^2/s	Molecular diffusion coefficient
e	-	Euler's number
f	Hz	Motion frequency
f_s	Hz	Sampling frequency
h	$\mathrm{W/(K\,m^2)}$	Heat transfer coefficient
H_L	W	Lamp heat flux
I	$\mathrm{W/m^2}$	Radiation intensity
k	-	Dimensionless motion frequency
L	m	Length
n	K or $\mathrm{W/m^2}$	Noise level
N	-	Amplification factor
p_i	-	Gaussian probability density function
P	-	Normalized probability density
$\dot{Q}$	W	Heat transfer rate
s	-	Skewness
S	K or $\mathrm{W/m^2}$	Signal
S^*	$\mathrm{W/m^2}$	Pseudo-signal
SNR	-	Signal-to-noise ratio
t	s	Time
t/T	-	Phase
t_n	K or $\mathrm{W/m^2}$	Signal threshold
T	s	Motion period
T'	K	Temperature
T'_w	K	Wall temperature
T'_∞	K	Freestream temperature
u	m/s	Flow velocity in x-direction
U	V	Voltage magnitude
U_∞	m/s	Freestream velocity
x	m	Streamwise coordinate
x_{tr}	m	Boundary layer transition location
y	m	Vertical coordinate

Greek symbols

Symbol	Unit	Description
α	°	Geometric angle of attack
α_0	°	Mean pitch angle
α_1	°	Pitch motion amplitude
α'	$\mathrm{m^2/s}$	Thermal diffusivity
δ	m	Boundary layer thickness
ΔI	$\mathrm{W/m^2}$	DIT signal
$\Delta t/T$	-	DIT image separation time step
ΔT	-	Phase lag
$\Delta T'$	K	DIT signal
ϵ_{RMS}	-	RMS transition measurement error
$\epsilon_{RMS,amp}$	-	Amplitude measurement error
$\epsilon_{\Delta T}$	-	Phase lag error
κ	W/(m K)	Thermal conductivity
μ	Pa s	Dynamic viscosity
μ'	-	Statistical mean
ν	$\mathrm{m^2/s}$	Kinematic viscosity
ρ	$\mathrm{kg/m^3}$	Mass density
σ	-	Standard deviation
τ	rad	Phase angle
τ_w	Pa	Wall shear stress
Ψ	°	Azimuth angle

Dimensionless numbers

Notation	Description	Definition
Bi	Biot number	$\frac{L \cdot h}{\kappa}$
Fo	Fourier number	$\frac{\alpha' \cdot t}{L^2}$
Ma	Mach number	$\frac{u}{a}$
Pr	Prandtl number	$\frac{C_P \cdot \mu}{\kappa}$
Re	Reynolds number	$\frac{U_\infty \cdot L}{\nu}$
Sc	Schmidt number	$\frac{\mu}{\rho \cdot D}$
St	Strouhal number	$\frac{h}{\rho \cdot U_\infty \cdot C_P}$

Abbreviations

Abbreviation	Meaning
1MG	“1-Meter-Göttingen” wind tunnel
ADIT	Adaptive differential infrared thermography
AEDC	Arnold Engineering Development Complex
CFD	Computational fluid dynamics
DIT	Differential infrared thermography
DLR	Deutsches Zentrum für Luft- und Raumfahrt (German Aerospace Center)
DGLR	Deutsche Gesellschaft für Luft- und Raumfahrt
FEM	Finite-element method
HF/HFA	Hot-film/Hot-film anemometry
IRT	Infrared thermography
LIT	Local infrared thermography
NASA	National Aeronautics and Space Administration
RMS	Root-mean-square
URANS	Unsteady Reynolds-averaged Navier-Stokes equations
σC_p	Pressure signal analysis technique

1

Introduction

The location of the laminar-turbulent boundary layer transition (also referred to as “transition” in the following) is a crucial design parameter for the aerodynamics of airfoils and aerodynamic vehicles in general. This is mainly due to the increased friction drag and increased heat exchange properties of turbulent boundary layers, and to the different separation and reattachment behavior of the two flow states, see Ch. 5 in Ref. [1]. For the simplified two-dimensional aerodynamics of airfoils, the boundary layer on the suction and on the pressure side of the airfoil is initially laminar and typically transitions to turbulence at some location over the chord length c, the boundary layer transition location x_{tr}. The mathematical prediction of the transition location has been subject to a large body of research for a long period of time, consider e.g. Ref. [30]. The solution of the full mathematical problem by solving the Navier-Stokes equations is impractical for high Reynolds number Re flow around airfoils, as the required computational power is increased beyond reason, see Sec. 1.3 in Ref. [46]. A complete mathematical explanation for two-dimensional transition to turbulence was established by Walter Tollmien as early as 1929 [52], but the calculation of the practically relevant three-dimensional transition process remains very complex as it is highly sensitive to a large set of parameters. Until today, valid analytical solutions exist only for simplified flow configurations, see Ch. 5 in Ref. [57] for an overview of the problem and Ch. 5 in Ref. [47] for the available solutions. Transition prediction in high Re problems relevant for engineering is therefore nowadays performed with calculation models including empirical factors, most prominently the e^N-method [54]. As an example, Fig. 1.1 shows the simulated boundary layer transition location normalized with the chord length x_{tr}/c on a helicopter rotor in forward flight from Heister [24]. The transition location is shown for the top and bottom side of the rotor, over the revolution in terms of the azimuth angle Ψ. The simulation includes empirical modeling of various transition mechanisms: cross-flow induced transition (CF), Tollmien-Schlichting waves (TS), transition over a laminar separation bubble (LS) and bypass transition (Byp).

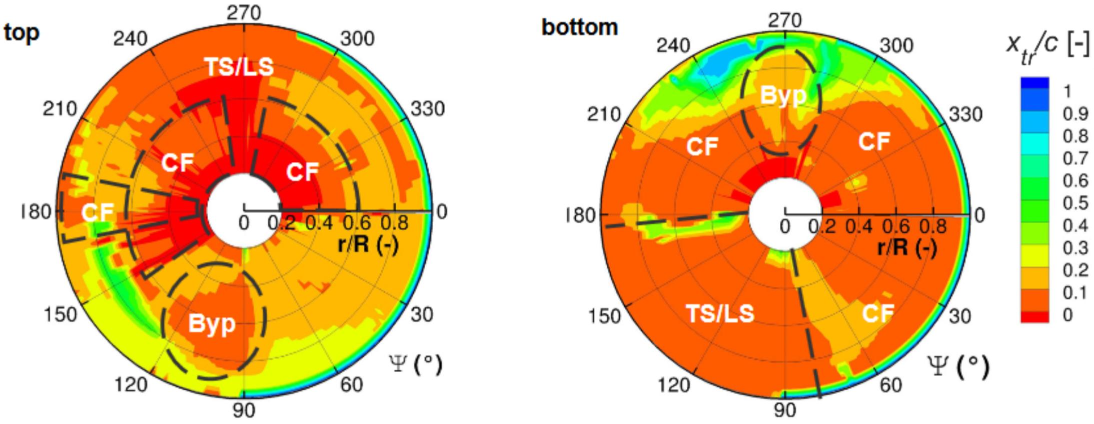

Figure 1.1: Simulated boundary layer transition on a helicopter rotor in forward flight, adapted from Heister [24], Fig. 21

The shown example illustrates that the prediction of boundary layer transition in technically relevant aerodynamic processes is a complex problem. It is clear that empirical calculation models for transition prediction need to be calibrated and validated with experimental data, which requires appropriate measurement techniques. A large variety of experimental techniques for measuring boundary layer transition exists, most of these techniques rely on measuring the different laminar or turbulent properties of either the momentum boundary layer (shear stress sensitive crystals [2], micropillar sensors [9], or oil flow interferometry [34]) or the temperature boundary layer (temperature-sensitive paint [3], hot film anemometry, see Sec. 2.2.1, and infrared thermography). Infrared thermography for transition detection is treated in this study. The history of its application in aerodynamics research is presented in the next section. The following section discusses the unsteady aerodynamics of helicopter rotors, a vital example for the technical relevance of unsteady aerodynamics as seen in Fig. 1.1. The last section of this introduction provides an overview of the research study documented in this report.

1.1. Infrared thermography for aerodynamics research

Infrared thermography (IRT) is an optical measurement technique, which means that measurements are performed with a camera. Using state of the art infrared cameras, the technique facilitates high accuracy, high spatial and temporal resolution temperature measurements of the object under investigation. For the physical background and information on the basic functioning principle of infrared cameras, the reader is referred to Ch. 2 and Ch. 3 of Ref. [4] for a comprehensive overview. The first results for aerodynamics research with IRT were produced in the year 1967 in Sweden by Thomann and Frisk [51] for a hypersonic $Ma = 7$ flow. The further development of the infrared cameras for aerodynamics research in the following years was fueled by the space exploration efforts in the 1970's, particularly at the Arnold Engineering Development Complex (AEDC), see e.g. Refs. [10] and [35]. IRT played an important role in the design of the first reentry vehicles, most notably the space shuttle, where it was used in wind tunnel design experiments [49] and also on the shuttle in flight [12]. In the 1980's, the main focus of aerodynamics research with IRT was shifted from hypersonic flows towards aerodynamics efficiency research, particularly boundary layer diagnostics in subsonic flows. The first time that boundary layer transition was investigated with an infrared camera was as early as 1977 by Peake et al. [37], and the improving camera accuracy over the following years allowed various boundary layer studies in wind tunnels as well as free flight experiments [8] and even cryogenic wind tunnels [22], where the setup with low thermal energy emission inherently works against the measurement principle of IRT. The IRT measurement technique has overcome the development stage in the 1990's [21] and became an established measurement technique for experimental aerodynamics with a wide range of applications available today, many of these reviewed by Carlomagno and Cardone in Ref. [11]. For boundary layer diagnostics, IRT nowadays allows a detailed investigation of various aspects, two examples are given in Figs. 1.2 and 1.3.

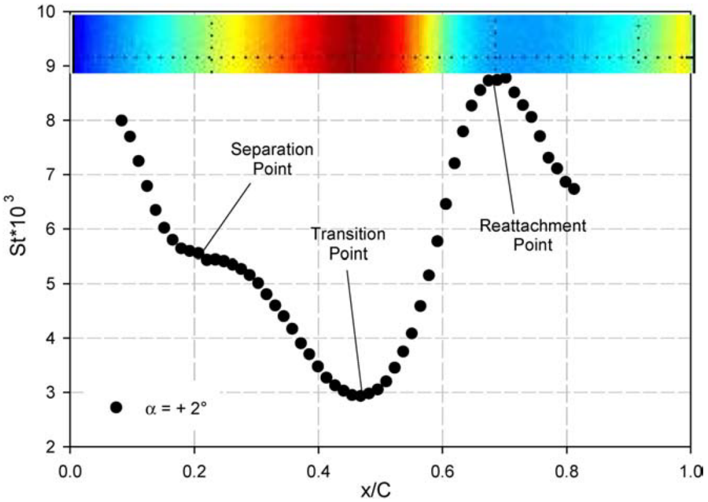

Figure 1.2: Boundary layer transition over a laminar separation bubble measured with infrared thermography, from Ricci and Montelpare [41], Fig. 13

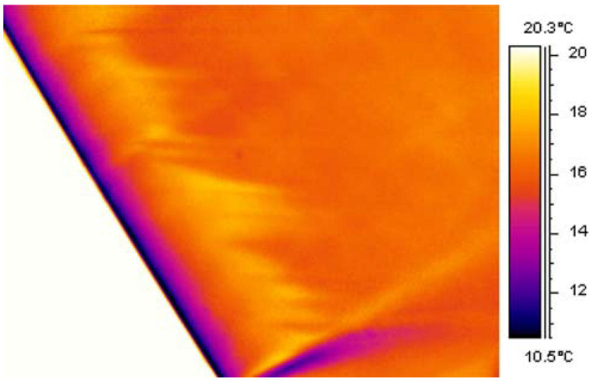

Figure 1.3: Boundary layer transition on a swept wing in supersonic flow measured with infrared thermography, from Zuccher and Saric [60], Fig. 10

Figure 1.2 shows the transition process over a laminar separation bubble for a RR3823HL airfoil at $Re = 200\,000$ with laminar separation, detached transition and turbulent reattachment measured by Ricci and Montelpare [41]. The second example for advanced boundary layer diagnostics with IRT shown in Fig. 1.3 is from Zuccher and Saric [60]. The transition front on a swept wing in $Ma = 2.4$ flow conditions is measured in a level of detail that allows the observation of the typical “saw-tooth” transition front for cross-flow induced transition. Besides boundary layer diagnostics, the applications of IRT include e.g. evaluating the efficiency of film cooling setups [13], measuring convective heat transfer maps resulting from jets impinging on a flat plate [45], and measurements of heat transfer on rotating surfaces [5]. An example that demonstrates the scalability of IRT to complex large-scale aerodynamic experiments is given by Richter and Schülein [42], who applied IRT to a full-scale *EC 135* helicopter in hover, see Fig. 1.4 below. In conclusion, IRT is a highly serviceable measurement technique for aerodynamics research in general and for boundary layer diagnostics in particular, because it is accurate, versatile and scalable for a wide range of applications in aerodynamic experiments.

Figure 1.4: Infrared thermography measurements on a helicopter rotor blade in hover, from Richter and Schülein [42], Fig. 18

1.2. Unsteady aerodynamics of helicopter rotors

The analysis of the aerodynamics experienced on helicopter rotors in forward flight is a particularly challenging problem. Even when the aerodynamic problem is strongly simplified to the analysis of the typical section by neglecting three-dimensional effects, the cyclically varying inflow conditions increase the complexity compared to steady aerodynamic problems. The geometric angle of attack α of the rotor blade against the flow is varied during one rotor revolution with the swash plate and pitch links, see Fig. 1.5. This is necessary to compensate for the uneven aerodynamic loading from the varying inflow velocity, depending on whether the rotor blade is on the advancing or retreating part of the rotor revolution, see Ch. 2 in Ref. [29]. This pitching motion introduces unsteady aerodynamic effects.

Research on the topic of unsteady subsonic aerodynamics has received considerable attention in the past century, with notable early works from Theodorsen [50] and from von Kármán and Sears [56] in the 1930's. The motivation for investing in this complex and costly research field is particularly fueled by the requirement of avoiding the typical catastrophic events assigned to unsteady aerodynamic effects on aircraft, like flutter for fixed wing aircraft or dynamic stall for rotary wing aircraft, see Ch. 5 in Ref. [15]. Both phenomena are associated with the occurrence of aerodynamic forces that are large enough to lead to structural failure of the aircraft wings or parts of the rotor head. A way to investigate these unsteady aerodynamic effects in wind tunnel experiments is to vary the angle α of an airfoil model cyclically. The produced aerodynamic forces on the pitching airfoil are not identical to those on a rotor, but have some similarities through the cyclic variation. Consequently, the harmonically pitching airfoil has been treated extensively in the literature and many important findings have been derived from this case historically, many of these reviewed by McCroskey in Ref. [31].

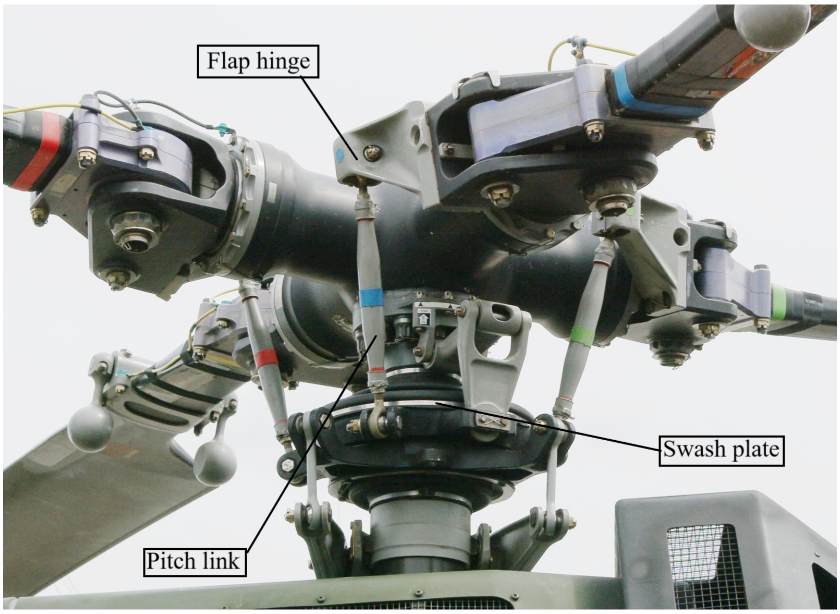

Figure 1.5: Rotor head of the *Bo 105*, adapted from Ref. [58]

Apart from investigating flutter or dynamic stall, research on unsteady aerodynamics is also directed towards aerodynamic shape optimization. An example for this is the recent development of a new helicopter rotor prototype at Airbus Helicopters [27], see Fig. 1.6. The study documented in this report is conducted at the helicopters department of the Institute of Aerodynamics and Flow Technology at the German Aerospace Center (DLR) in Göttingen. A harmonically pitching helicopter blade airfoil is investigated the wind tunnel, with the intention to develop an appropriate boundary layer transition measurement scheme that can be used for validation and calibration purposes in the design optimization process of new helicopter rotors.

Figure 1.6: *GRC1* five-bladed helicopter rotor prototype, from Kus et al. [27]

1.3. Structure of this report

The research question driving the studies documented in this report is: "*Can the unsteady boundary layer transition location on a pitching airfoil model be determined efficiently under various motion amplitude and frequency conditions by using infrared thermography?*". The structure of this report is visualized in Fig. 1.7 and discussed in the following.

In Ch. 2, the currently available experimental techniques for measuring unsteady boundary layer transition are introduced. The unsteady aerodynamics on a pitching airfoil limit the range of transition measurement techniques to three techniques that can be considered as the current state of the art: Hot-film anemometry, σC_p pressure signal analysis and differential infrared thermography (DIT). Two of these techniques are used in this report. Results from the σC_p-technique are used as reference for the measurement schemes based on infrared thermography that are developed in the studies documented in this report.

The following Ch. 3 describes the experimental setup that is used to produce the data that is analyzed in this report. The experiments have not been performed by the author. The chapter also includes the description of a computational setup, where the unsteady thermal behavior of the same airfoil model in a similar experiment was modeled for a previous study. Results from this setup are analyzed in this study as well. Both setups include a periodically pitching airfoil at subsonic ($Ma \leq 0.3$), high Reynolds number ($Re \geq 1 \cdot 10^6$) flow conditions. The experimental test matrix includes a large range of test parameters for the pitching frequency f and amplitude α_1, results from the numerical simulation are limited to a single pitching motion case.

The goal of the studies documented in this report is to extend the range of experimental methods for measuring unsteady boundary layer transition. For that, two approaches are followed: the optimization of differential infrared thermography along recommendations from the literature in Ch. 4 and the development of two new transition measurement schemes based on infrared thermography measurements in Ch. 5. The first new development is an automated selection of the image separation time step for the application of differential infrared thermography, termed adaptive differential infrared thermography (ADIT). The second development is local infrared thermography (LIT), a transition measurement scheme that is based on the analysis of the temperature over time at fixed locations on the model surface.

The new approaches are developed and tested on a quasi-steady model of the DIT method and on the numerical simulation results. The confirmed procedures are then applied to the experimental data from the wind tunnel tests in Ch. 6. This includes a demonstration of the capabilities of the LIT approach for analyzing the entire airfoil model suction surface, thus measuring the two-dimensional transition front. The newly developed schemes are compared with the optimized DIT results of Ch. 4 and found to be an improvement over that approach. Section 6.2 includes a comparison of the improved measurement schemes with the reference transition measurements from the σC_p-technique. Ultimately, the conclusions of the performed studies are derived in Ch. 7. The final component of the conclusions of this report is the answer to the research question.

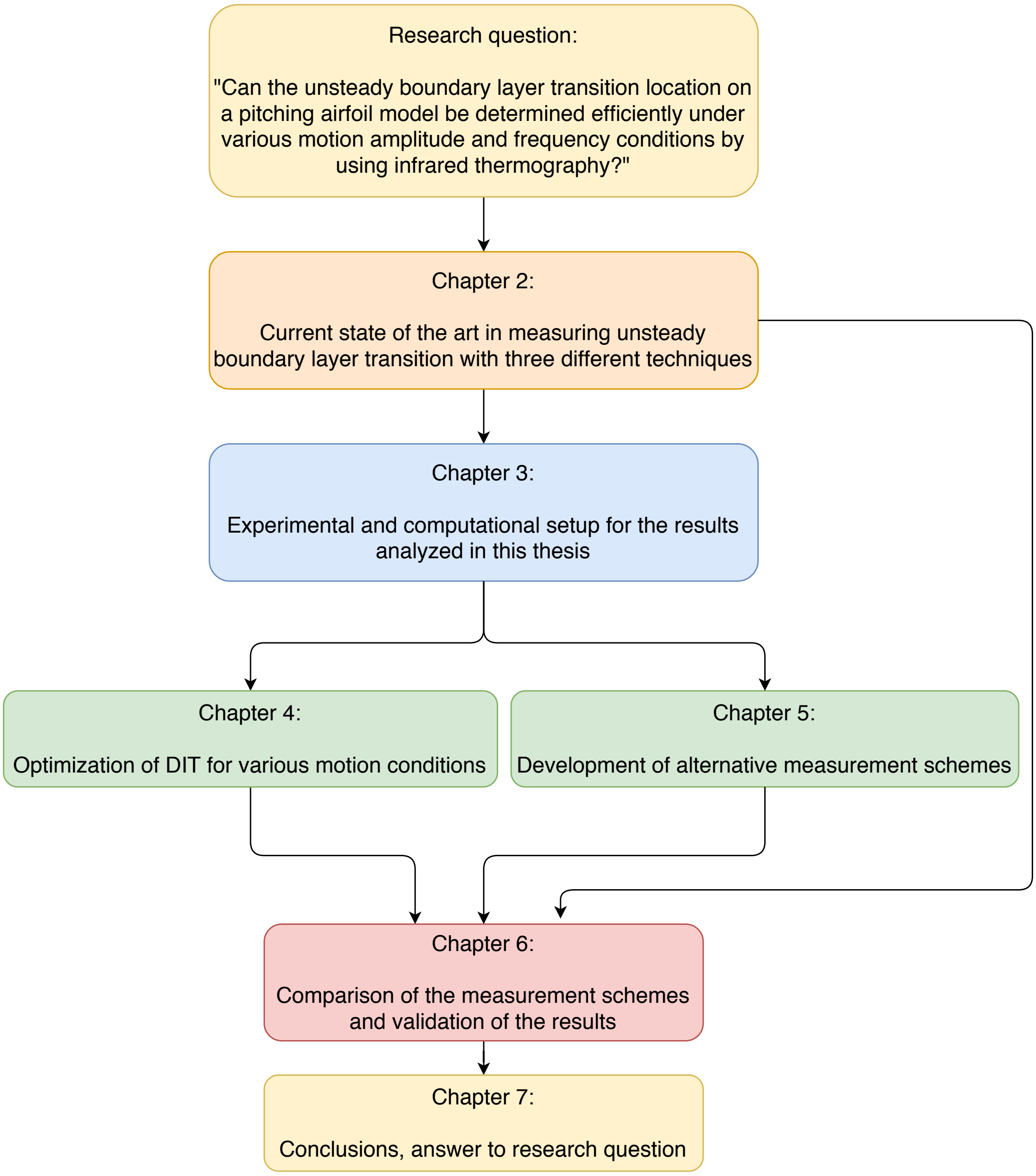

Figure 1.7: Illustration of the structure of this report

2

Unsteady boundary layer transition measurements: State of the art

In this chapter, the underlying principles for measuring boundary layer transition and the problems that emerge for applications with unsteady aerodynamics are discussed. After that, three experimental techniques that are applicable to unsteady subsonic boundary layer transition measurements are introduced and compared.

2.1. Theoretical background

Since the concept of the boundary layer has been introduced by Ludwig Prandtl in 1904 [38], the investigation of the phenomenon of boundary layer transition has been a major research field in aerodynamics. For engineers, it is not the primary interest to investigate the transition process in detail, as long as the prediction of its occurrence can be done with sufficient accuracy. Transition prediction can be done based on observations, thus existing measurements of the transition location. To be able to measure transition, the main features of the transition process as well as the different properties of laminar and turbulent boundary layers need to be known. When referring to boundary layers in aerodynamics, typically the momentum boundary layer is addressed, i.e. the fluid retarded by viscosity near solid walls. Additional to the properties of the momentum boundary layer, this section treats the thermal boundary layer that develops when the wall has a different temperature than the flow. It is shown that the two boundary layers are analogous in typical aerodynamic problems. A schematic of the flat plate boundary layer is shown below in Fig. 2.1. The boundary layer flow is initially laminar and then transitions to turbulence. Outside of the transitional region, the boundary layer on a flat surface is self-similar and exhibits qualitatively identical velocity profiles. The boundary layer thickness δ grows with x in the direction of the freestream U_∞ in the laminar and turbulent region respectively, see Ch. 7 in Ref. [47]. The boundary layer velocity profile is distinctively different for laminar and turbulent boundary layers and varies throughout the transition process, as illustrated in Fig. 2.2.

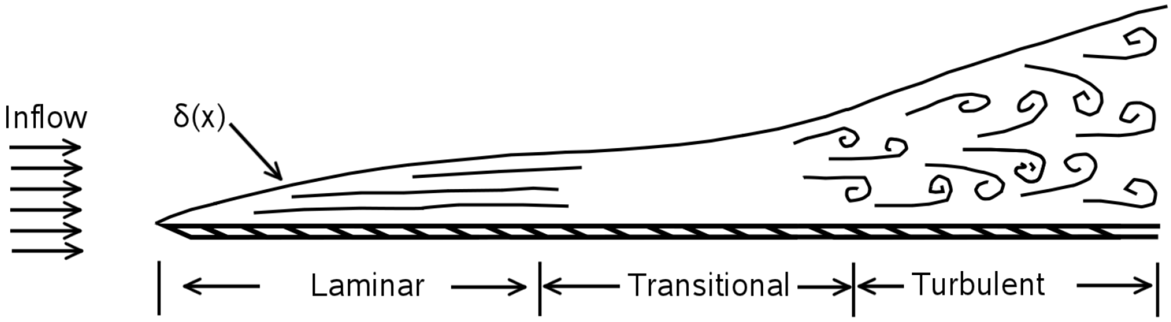

Figure 2.1: Schematic of the flat plate boundary layer, adapted from Schlichting and Gersten [47], Fig. 15.5

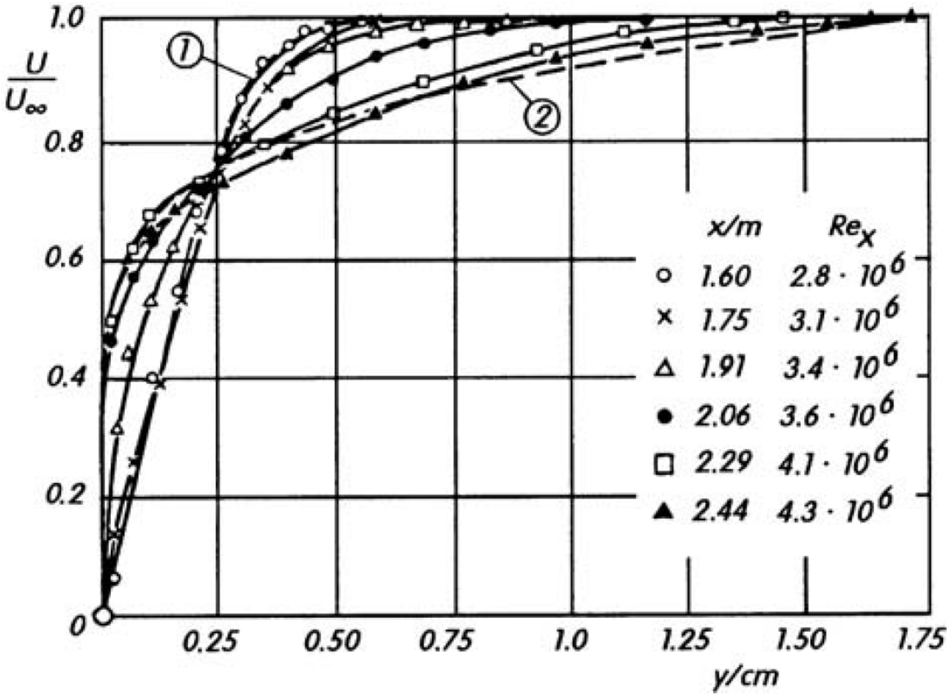

Figure 2.2: Boundary layer velocity profiles for (1) laminar, transitional and (2) turbulent boundary layers, from Schlichting and Gersten [47], Fig. 15.7

A key difference in the velocity profiles of laminar and turbulent boundary layers is the velocity gradient at the wall $(\partial u/\partial y)_{y=0}$, which is larger for turbulent flows. The velocity gradient relates to the shear stress on the wall τ_w with the fluid's dynamic viscosity μ.

$$\tau_w = \mu\left(\frac{\partial u}{\partial y}\right)_{y=0} \tag{2.1}$$

The wall shear stress τ_w is typically normalized with the dynamic pressure of the freestream $\frac{1}{2}\rho U_\infty^2$ and expressed in terms of a dimensionless parameter, the skin friction coefficient C_f.

$$C_f = \frac{\tau_w}{\frac{1}{2}\rho U_\infty^2} \tag{2.2}$$

C_f is a highly relevant parameter in aerodynamic shape design, because it relates to the friction drag that is produced by an object in the flow. It is therefore a crucial design parameter for airfoils.

The boundary layer velocity profiles on airfoils resemble those of the flat plate boundary layer, as such they are approximately self-similar and the boundary layer thickness $\delta(x)$ grows monotonously with x from the stagnation point. Near the stagnation point, the boundary layer is thin which results in a large value of the velocity gradient $(\partial u/\partial y)_{y=0}$. Consequently, C_f is large near the leading edge and then decreases with the increasing boundary layer thickness $\delta(x)$. A distinct increase in C_f is then observed when the boundary layer transitions to turbulence, resulting from the qualitative changes in the velocity profiles with an increased $(\partial u/\partial y)_{y=0}$ and from Eq. 2.1. Downstream of the boundary layer transition location, C_f decreases again with increasing x and $\delta(x)$.

The described behavior has been explored in theory for the flat plate by Blasius in 1908 [7] and was confirmed with several experiments. Figure 2.3 shows results for the laminar and turbulent flat plate boundary layer. Note that the argument only holds for attached flow. When the flow separates from the surface, the velocity profiles are qualitatively significantly different, see Sec. 2.6 in Ref. [47].

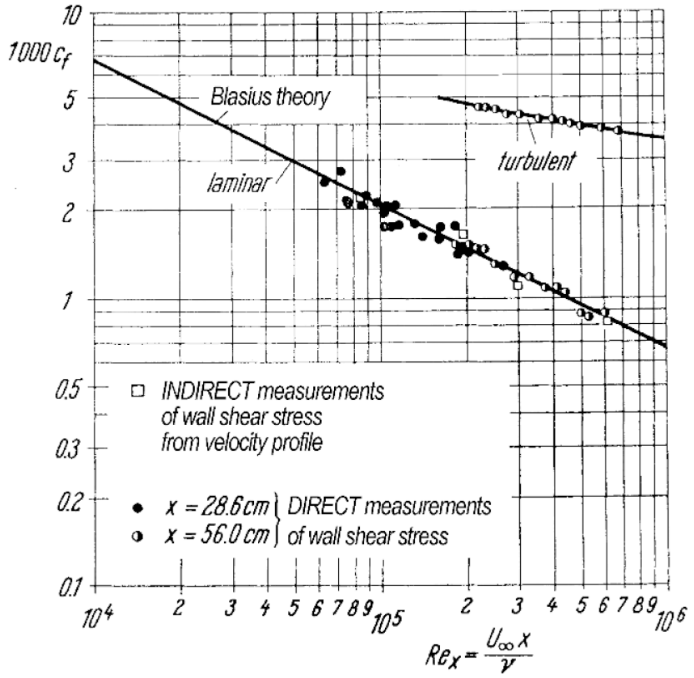

Figure 2.3: Theoretical and measured values of the skin friction coefficient C_f for laminar and turbulent boundary layers, from Schlichting and Gersten [47], Fig. 6.8

When a temperature difference between the flow and the surface exists in aerodynamics, heat exchange between the two is dominated by convective heat transfer. Newton's law of cooling describes the heat transfer rate $\dot{Q}$ from the surface with area A to the flow as proportional to the difference in the temperature T' between the surface and the flow $\Delta T' = T'_w - T'_\infty$ through a single parameter, the convection heat transfer coefficient h.

$$\dot{Q} = h \cdot A \cdot (T_w - T_\infty) \tag{2.3}$$

The convective heat transfer is typically expressed in dimensionless numbers. The dimensionless number relevant for aerodynamic flows is the Stanton number St. It relates the convective heat transfer h to the freestream velocity U_∞ and the thermal capacity of the fluid $\rho \cdot C_P$.

$$St = \frac{h}{\rho \cdot U_\infty \cdot C_P} \tag{2.4}$$

As result of the occurrence of convective heat transfer, a temperature boundary layer can be observed around the object, that describes the temperature profile near the wall until the temperature is constant away from the wall at the freestream temperature T'_∞. The previously discussed momentum boundary layer and the thermal boundary layer are analogous in typical aerodynamic flows, which means that they are governed by the same dimensionless parameters and produce the same qualitative behavior. In the case of the thermal and momentum boundary layers, this analogy is called the Reynolds analogy and the most prominent result is the equivalence of the Stanton number St and the skin friction coefficient C_f divided by two, see Sec. 10.4 in Ref. [47].

$$\frac{C_f}{2} = St \tag{2.5}$$

Note that the analogy is not a general law, but an approximate relation that is valid as long as the Prandtl number Pr and Schmidt number Sc are close to unity (equivalence of viscous diffusion rate and thermal diffusion rate $Pr = \frac{C_P \cdot \mu}{\kappa} \approx 1$ and equivalence of viscous diffusion rate and molecular diffusion rate $Sc = \frac{\mu}{\rho \cdot D} \approx 1$), as well as no large pressure gradients occur, see Sec. 6.7.3 in Ref. [26]. These assumptions are typically valid for the aerodynamics of airfoils, such that the analysis of the local convective heat transfer allows the extraction of information about the skin friction at the surface.

The observable temperature distribution on an airfoil model surface results from a combination of the convective heat transfer at the surface and the phenomenon of thermal conduction within the model material. In the simplest case of thermal conduction, in the absence of all sources and sinks of heat, the phenomenon is governed by the heat equation in Eq. 2.6:

$$\frac{\partial T'}{\partial t} = \alpha' \nabla^2 T', \tag{2.6}$$

where T' is the temperature and α' is the thermal diffusivity:

$$\alpha' = \frac{\kappa}{\rho \cdot C_P}, \tag{2.7}$$

where κ is the thermal conductivity, ρ is the density and C_P is the heat capacity of the material.

Equation 2.6 shows that thermal conduction is a time dependent phenomenon. For the entire history of aerodynamics research with infrared thermography, the unsteady heat conduction in the investigated structure has been a known problem. Hypersonic wind tunnels are of the blow down type and therefore no steady state measurements of the temperature can be performed. This issue is resolved by solving the unsteady heat conduction equation since the first applications of IRT for aerodynamics research until today [6]. Because the flow problem is typically steady for a small time scale and the resulting temperature changes on the model are considerable in hypersonic flows, simplifying assumptions of the calculation have a negligible influence on the results. The problem is amplified in subsonic unsteady aerodynamic flows, because the aerodynamics and therewith the heat transfer are time-dependent, and the temperature difference between the model and the flow as well as the magnitude of C_f are relatively small. Hence, the observed temperature differences are small, typically at the order of magnitude of the noise equivalent temperature difference of modern infrared cameras. Unsteady heat transfer problems are typically described using dimensionless numbers. The Fourier number Fo characterizes the degree of unsteadiness of a heat transfer problem with the ratio of the heat conduction rate and the heat storage rate:

$$Fo = \frac{\alpha' \cdot t}{L^2}, \tag{2.8}$$

where t is the time scale of the unsteadiness, e.g. the pitching motion period T, and L is the conduction penetration length, e.g. the thickness of the airfoil surface. Low Fourier numbers $Fo \ll 1$ signal a high level of unsteadiness.

The Biot number Bi is the ratio of the resistance to heat conduction inside a body and the resistance to convection of heat to a fluid at its surface:

$$Bi = \frac{L \cdot h}{\kappa}. \tag{2.9}$$

In typical aerodynamics problems, the resistance to convection is small compared to the resistance to conduction, so the Biot number is large, which yields large temperature gradients in the direction of the material in unsteady flows with varying C_f.

2.2. Experimental techniques

2.2.1. Hot-film anemometry

Hot-film anemometry (HFA) is a quantitative, high accuracy direct heat transfer measurement technique with excellent temporal resolution, see Sec. 5.2 in Ref. [53]. The working principle of HFA can be summarized as one or more thin metal films that are installed on the model surface and kept at a constant temperature much larger than the flow temperature through resistive heating. The amount of voltage that needs to be supplied to maintain the constant temperature is measured. Through a calibration, the measured voltage signal U can used to calculate the amount of convective heat transfer at the surface of the film sensor with very short response times, as $L \rightarrow 0$ and thus $Fo \gg 1$. Consider Fig. 2.4 from Lee and Basu [28] as an example for the application of HFA to unsteady boundary layer measurements on a pitching airfoil model.

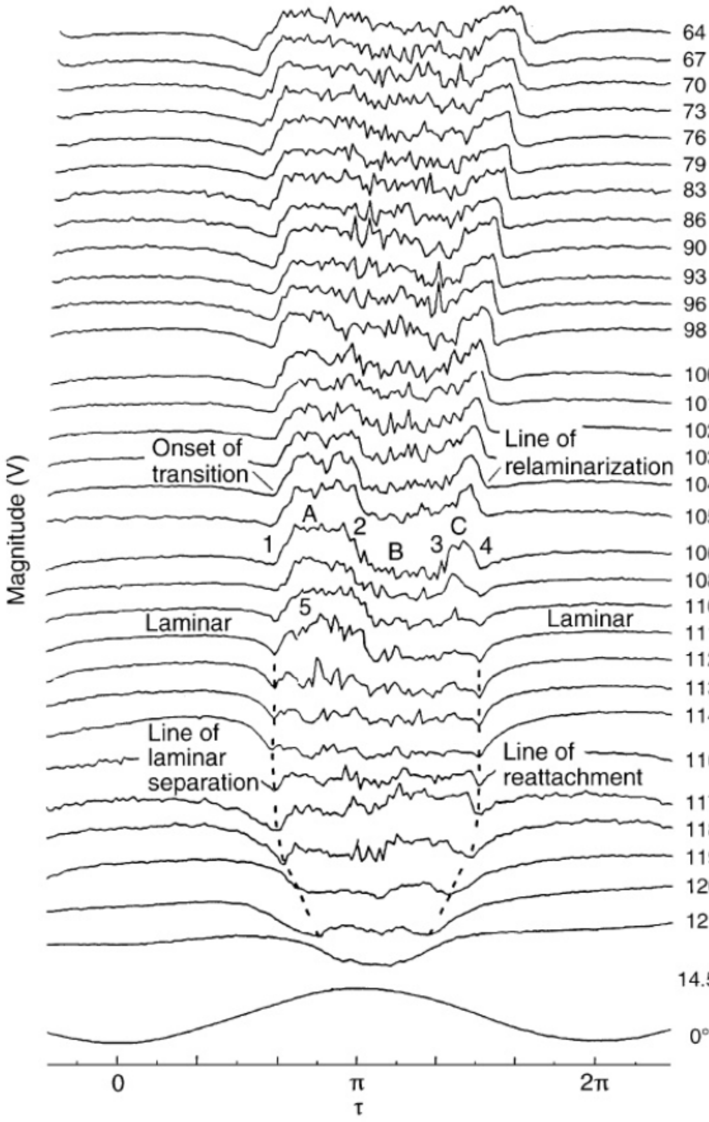

Figure 2.4: Voltage signal of multiple hot-film sensors over the chord length of a pitching airfoil, from Lee and Basu [28], Fig. 11b

The example shown in Fig. 2.4 nicely illustrates the information that can be obtained from HFA measurements, but also demonstrates the disadvantages of the technique. The graph shows the voltage magnitude U measured on ca. 40 hot-film sensors for a sinusoidal pitching motion of a NACA 0012 airfoil model at mean angle $\alpha_0 = 7.5°$, pitch amplitude $\alpha_1 = 7°$, reduced pitching frequency $k = 0.109$, and inflow at $Re = 169\,000$. The sensors are located on the model suction surface from the leading edge to approximately mid-chord (see Fig. 1 in Ref. [28]). While laminar flow can be identified as low noise region, the transition to turbulence causes an increase in the measured voltage, as seen for the downstream sensors with the lower indices. Near the leading edge, laminar separation occurs and the signal of the affected sensors drops to a lower level and becomes noisy. For the sensors in between, transition (1), turbulent flow (A+C), separation (2), separated flow (B), turbulent reattachement (3), and relaminarization (4) all can be identified in the shown voltage signal. This analysis shows that HFA is an appropriate tool for unsteady boundary layer transition measurements. An observed advantage is that a quantitative calibration of the sensors is not necessary to perform boundary layer diagnostics. However, a major disadvantage of HFA emerges from the shown data as well. To produce the shown result and derive the observations, over 100 sensors had to be installed, measured, and then analyzed. This is connected to a significant experimental effort and several difficulties, e.g. the installation of the heated sensors on the model surface without notably affecting the boundary layer flow.

Recently, there have been advances in the automated analysis of HFA data proposed by Richter et al. [43]. Statistical analysis of the data from a pitching airfoil ($\alpha_0 = 4°$, $\alpha_1 = 6°$, $f = 6.6$ Hz, $Re = 1.8 \cdot 10^6$) where laminar and turbulent flow both occur on a sensor location ($x/c = 0.07$ on the upper side) is shown in Fig. 2.5. The analysis of the skewness s of the signal allows the extraction of the transition onset and end as well as the 50% intermittency location (often considered as *the* transition location, see e.g. Refs. [42] and [48]). While the automated approach is instrumental for the data analysis of unsteady hot film data, several problems remain. Firstly, the automated approach fails or needs to be updated when laminar or turbulent flow separation occurs. Secondly, while the data analysis is improved, the instrumentation effort remains unchanged. It becomes apparent, that the more information is needed from the flow, the more experimental effort is necessary with HFA. In an industry development environment, this can generally be tolerated, as flow measurements are typically only used to investigate one certain parameter. In research, more fundamental questions are asked and the effort quickly becomes prohibitive.

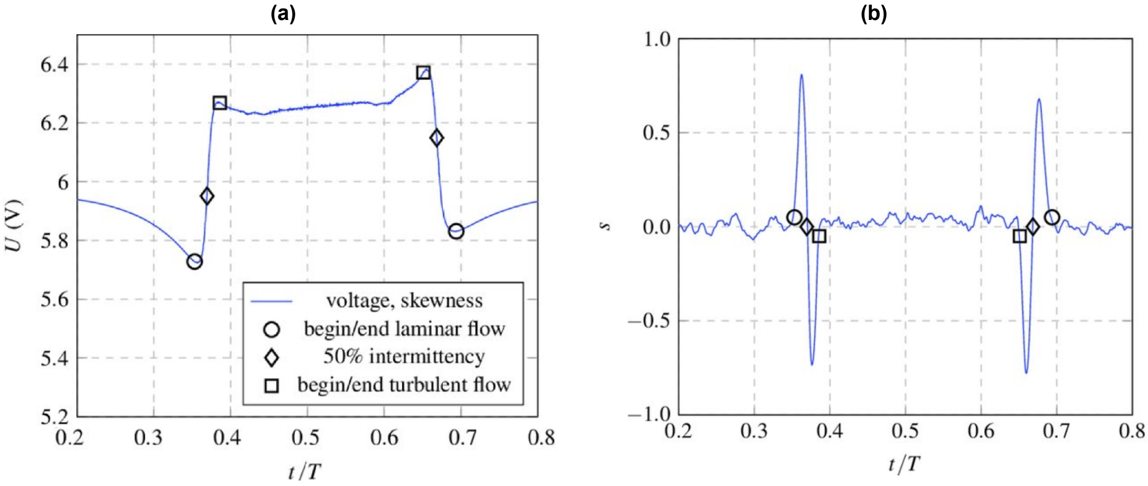

Figure 2.5: Methodology for an automated analysis of HFA data, (a): Voltage signal over the period at $x/c = 0.07$, (b): skewness of the voltage signal, adapted from Richter et al. [43], Fig. 4

2.2.2. σC_p Pressure signal analysis

Pressure signal analysis is an alternative to HFA that has been developed at the helicopters group at DLR Göttingen by Gardner et al. [18] specifically for boundary layer transition measurements in unsteady periodic processes like the pitching airfoil. The technique measures the occurrence of boundary layer transition by analyzing surface pressure fluctuations. It is based on measurements acquired with fast-response pressure sensors installed under the model surface. The similar analysis of surface pressure fluctuations measured with microphones to identify boundary layer transition is an established experimental technique in steady aerodynamics problems, which has been in use for decades e.g. at AEDC [14]. In these steady aerodynamics applications, the level of pressure fluctuations over the model surface is compared and typically, the location of the sensor with the largest fluctuations ("σC_p-peak") is detected as the transition location in subsonic flow. For measuring the boundary layer transition location in unsteady processes with σC_p pressure signal analysis, the signals over time from all pressure sensors on the model are analyzed individually. The working principle of the σC_p-technique for a pitching airfoil is described in the following.

It was shown in Sec. 2.1 that the boundary layer transition process has a major effect on the velocity gradient at the wall and on the boundary layer thickness. Accordingly, the transition to turbulence on the suction surface of an airfoil goes along with a kink in the surface pressure distribution C_p, see Fig. 2.6a. Because the transition location is always moving back and forth on a very small scale, a pressure sensor located within the transitional region will measure a highly fluctuating signal [18]. When analyzing the standard deviation σ of the local pressure coefficient C_p for one sensor location over the motion period of a pitching airfoil as shown in Fig. 2.6b, the angles α at which the transition location is at the sensor location (here $x/c = 0.19$) can be identified as distinct peaks. The same procedure can be performed for all pressure sensor locations where boundary layer transition occurs. The results from the σC_p pressure signal analysis are in good agreement with transition measurements with HFA for a periodically pitching airfoil. Similar to HFA, the σC_p-technique is intrusive and suffers from a low spatial resolution, proportional to the number of pressure taps and pressure sensors installed under the surface of the experimental model. An advantage of σC_p over HFA is that pressure sensors are already installed on most airfoil models for wind tunnel testing and their measurement system is typically an inherent part the experimental setup. This reduces the experimental effort compared to HFA. For the designated application, the technique is useful and reliable and has been applied by other researchers recently [17].

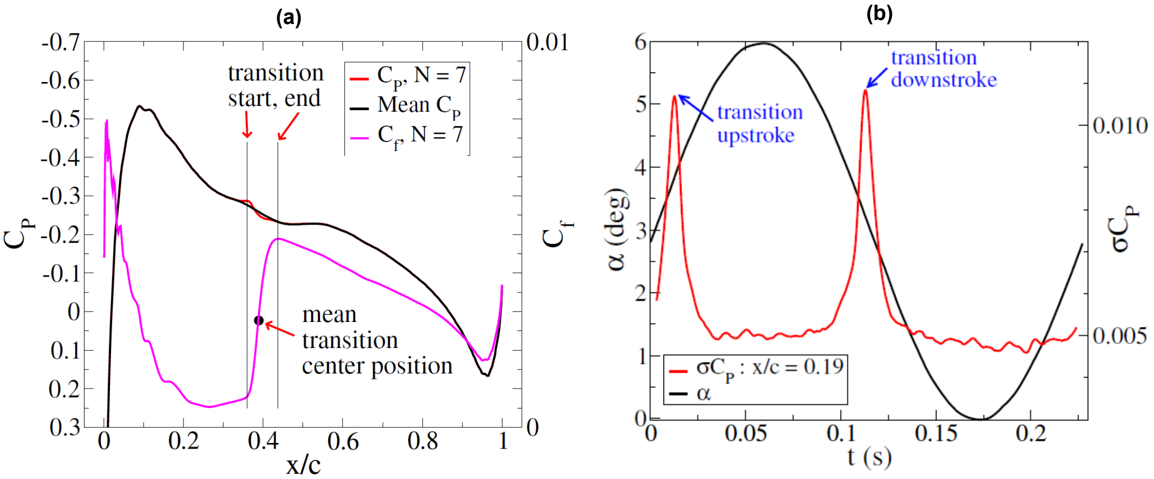

Figure 2.6: (a): Effect of boundary layer transition on the surface pressure distribution, (b): Methodology of σC_p pressure signal analysis, from Richter et al. [44], Figs. 5 and 6

2.2.3. Differential infrared thermography

Differential infrared thermography (DIT), first introduced in 2014 by Raffel and Merz [39], aims to be the extension of IRT for boundary layer transition measurements in unsteady aerodynamic processes. The idea of DIT is to avoid the slow temperature response of the surface material to the changing aerodynamics in low Fo problems by subtracting subsequent infrared camera measurements. It is suggested that the largest difference between the two subtracted thermographs can be accredited to the most distinct aerodynamic difference between them; the moving boundary layer transition location. The DIT methodology is described in the following for the example case of a pitching airfoil in subsonic flow.

The methodology of DIT is based on evaluating temperature differences, in the example of a pitching airfoil the difference between the two temperature distributions on the airfoil measured at the similar incidence angles α_A and α_B, where $\alpha_A < \alpha_B$ as illustrated in Fig. 2.7a. This subtraction scheme is the key novelty of the DIT technique, since conventional differential techniques used in IRT measurements use fixed reference temperature distributions for subtraction, as first introduced by Gartenberg and Wright [22]. The subtracting of similar temperature distributions has the goal to identify unsteady boundary layer transition as the phenomenon that causes the largest temperature differences in a short time frame. This is justified from the St-curve for the turbulent boundary layer lying significantly above the laminar curve, as shown in Fig. 2.3 in Sec. 2.1. In the example case illustrated in Fig. 2.7b, the higher angle α_B triggers transition at an earlier stage than at α_A, resulting in a smaller value of Re_x for the onset and end of the transition for α_B compared to α_A. When the surface temperature distributions for the two α are subtracted as done first in Ref. [39], a distinct $\Delta T'$-peak can be observed in the temperature difference data. From the discussion of convective heat transfer in aerodynamics of Sec. 2.1, it is justified to relate this peak to the occurrence of boundary layer transition. In the methodology of DIT, this peak is the transition measurement result associated to the average angle of the angles α_A and α_B from the two subtracted thermographic measurements.

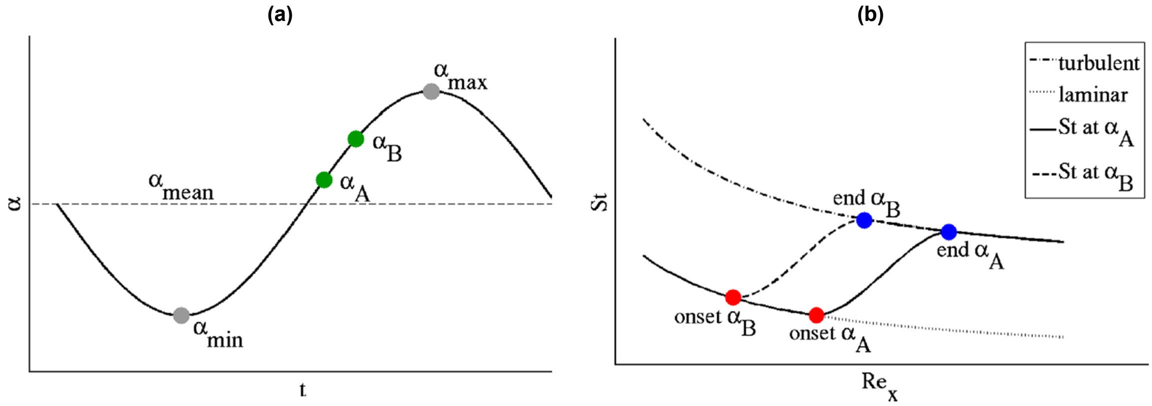

Figure 2.7: (a): Sinusoidal airfoil pitching motion schematic,
(b): Idealized St-number curves for two different α, from Raffel et al. [40], Figs. 1 and 2

When comparing results for the unsteady boundary layer transition obtained with DIT to transition locations measured by the two established techniques HFA and σC_p as done by Richter et al. [44] (see Fig. 2.9), a systematic time lag of DIT is observed, meaning that the found temperature difference peak is not necessarily identical to the moving transition location, but is also affected by the transient thermal properties of the surface under investigation. Furthmore, it was found by Raffel et al. [40] that the DIT technique cannot be applied in the parts of the motion cycle near the turning points α_{min} and α_{max}, where the transition location is not moving fast enough. The next step in the development of DIT was the modeling of the unsteady thermal conduction effects by Gardner et al. [20] with a coupled thermal finite-element method (FEM) and unsteady computational fluid dynamics (CFD) simulation. The used FEM model considers a constant heat input by radiation, heat output by convection based on skin friction distributions calculated with the URANS[1] CFD simulation and conduction of heat in vertical stacks with adiabatic wall boundary conditions. The motion parameters for the URANS simulation are selected to reproduce the experiment of Richter et al. [44]. The thermal FEM model neglects horizontal conduction and simplifies the model surface to a two-dimensional cross section to save computational effort. This is justified because the temperature gradients in the direction of the material are much larger ($Bi \gg 1$) than the horizontal and tangential temperature gradients. Furthermore, for the sources and sinks of heat only the most strongly contributing terms have been modeled. A strong simplification is the assumption of uniform material parameters, as the airfoil model is made out of a composite material of carbon fiber (ca. $\kappa = 190\,\mathrm{W/m \cdot K}$, $C_P = 700\,\mathrm{J/kg \cdot K}$, see Tab. A.2 in Ref. [26]) and epoxy (ca. $\kappa = 0.5\,\mathrm{W/m \cdot K}$, $C_P = 2300\,\mathrm{J/kg \cdot K}$, see Tab. 2 in Ref. [20]). The computational setup for the simulation is further discussed in Sec. 3.3. The key finding of the study by Gardner et al. [20] is that the agreement between the temperature difference peak and the boundary layer transition location can be improved by reducing the image separation time step between the subtracted infrared images. In Fig. 2.8a, temperature difference plots for various time steps are shown. The subtracted temperature distributions are selected such that the average angle of the two images is identical for all shown curves. The distance of the temperature difference peak from the transition position decreases with smaller image time separations $t_2 - t_1$. Figure 2.8a shows an additional trend in the temperature difference data with the decreasing time step size; the plots are similar qualitatively but the smaller time steps result in a smaller temperature difference signal and therefore also the prominence of the temperature difference peak is declining. These two key parameters can be extracted from Fig. 2.8a as shown in Fig. 2.8b, where both the measurement lag of the temperature peak with respect to the transition location (“Relative delay”) and the signal strength are plotted over the image separation time step size. All values in Fig. 2.8b are normalized with the values for the lag and DIT peak at the data point with $t_2 - t_1 = 5.3\,\mathrm{ms}$. Gardner et al. [20] suggest to decrease the image separation time step as much as possible, just before the sought peak cannot be detected anymore, to decrease the systematic time lag as much as possible. Another relevant finding of this study is the detailed behavior of the temperature difference near the motion turning points, which can be used to define the expected sign of the DIT signal and by that remove erroneous data points.

---

[1] Unsteady Reynolds-Averaged Navier-Stokes Equations

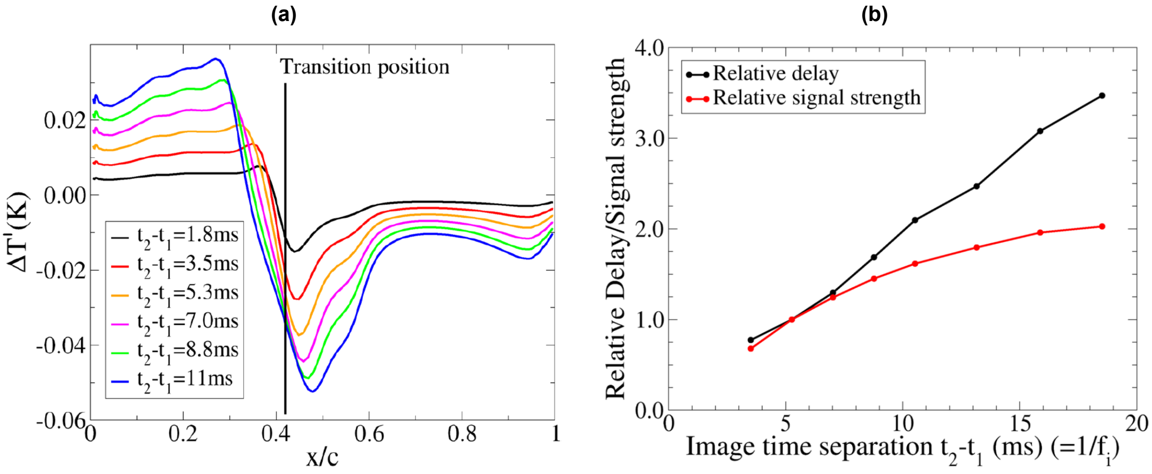

Figure 2.8: (a): Temperature difference distributions for different DIT image separation time steps, (b): Systematic time lag and signal strength versus image separation time step, from Gardner et al. [20], Figs. 22 and 23

2.2.4. Summary

Richter et al. [44] performed an experiment where HFA, σC_p and DIT have been applied simultaneously to compare the transition measurement results. An example result for the comparison is shown in Fig. 2.9 for a DSA-9A helicopter airfoil model at $\alpha_0 = 5^\circ$, $\alpha_1 = 6^\circ$, $Re = 1.8 \cdot 10^6$, $Ma = 0.3$ and $k = 0.06$. The differences between HFA and σC_p are aerodynamic differences, resulting from the pressure taps and hot film sensors intruding the boundary layer flow on different spanwise locations for the two sensor types. In the DIT results, many data points are missing near the motion turning points. In this example, a comparison to the results from the σC_p-technique suggests that the DIT technique only resolves the unsteady transition movement over ca. 60% of the chord region that experiences boundary layer transition. In the region where DIT yields valid results, the data points are spaced more densely than for the other two techniques. The DIT results shown in Fig. 2.9 exhibit the discussed systematic time lag with respect to the other techniques. All findings about the three experimental techniques from the previous three subsections are summarized in Tab. 2.1.

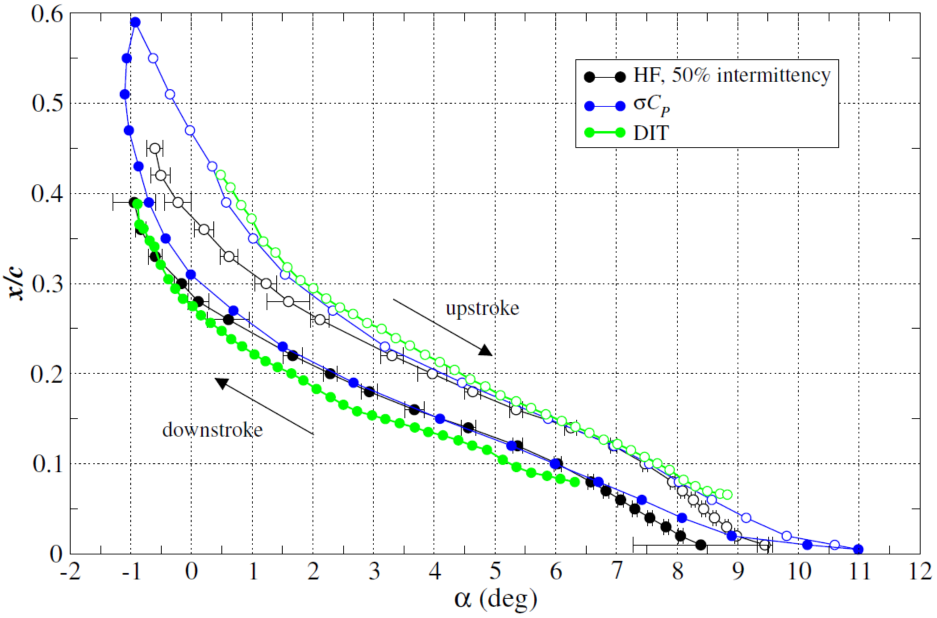

Figure 2.9: Comparison of a preliminary DIT result with hot film (HF) anemometry and σC_p results, from Richter et al. [44], Fig. 16

Technique	Applications	Advantages	Disadvantages
HFA	All boundary layer diagnostics	Universal use, high temporal resolution	Intrusive, large experimental effort, hence low spatial resolution
σC_p	Steady and unsteady transition	High temporal resolution sensors inherent part of typical setup	Intrusive, sensor number fixed hence low spatial resolution
DIT	Steady and unsteady transition, static and dynamic stall	Non-intrusive, low experimental effort, high spatial resolution	Current development, Systematic measurement errors

Table 2.1: Overview unsteady boundary layer transition measurement techniques

In conclusion, the state of development of DIT as unsteady boundary layer transition detection technique is beyond the proof of concept, but not sufficient to promote a wide-spread use. Since it was first introduced to the field in 2014, the technique has been used in different experimental setups by the same research group at DLR. It has additionally been adapted to detect static and dynamic stall by Gardner et al. [19]. In recent years, the idea of the technique has also been seized by other researchers, who have used a similar approach by applying the differential technique to infrared camera measurements in experiments with declining temperatures on a helicopter fuselage [23] and static airfoils [55]. Overmeyer et al. [36] exploited the scalability of the technique by detecting unsteady transition on a large scale model helicopter rotor in forward flight with DIT in the wind tunnel at NASA Langley, see Fig. 2.10.

Figure 2.10: Large-scale helicopter model wind tunnel experiment for the application of DIT, from Overmeyer et al. [36]

The first study where the DIT image time separation step is systematically varied over a large range to verify the findings from the heat transfer simulation by Gardner et al. [20] is documented in this report, beginning with a presentation of the experimental setup in the upcoming Ch. 3. An optimization of the DIT time step can be performed along the recommendations discussed in Sec. 2.2.3. This optimization is documented in Ch. 4 of this report and has been published by the author in a related study (Wolf et. al [59]: C. C. Wolf, C. Mertens, A. D. Gardner, C. Dollinger and A. Fischer. Optimisation of differential infrared thermography for unsteady boundary layer transition measurement. In *44th European Rotorcraft Forum*, Delft, Netherlands, September 2018). Further contributions to the development of unsteady transition measurement schemes based on infrared camera measurements are provided in Ch. 5 and Ch. 6 of this report. Parts of the findings of this study have been published as well (C. Mertens et al. [32]: C. Mertens, C. C. Wolf and A. D. Gardner. Unsteady boundary layer transition detection with local infrared thermography. In *21st DGLR STAB symposium*, Darmstadt, Germany, November 2018).

3

Experimental and computational setup

The experimental setup that was used in January 2018 (the experiment was not performed by the author) to produce the data which is analyzed in this report is introduced and an overview of the preliminary data processing activities that are connected to the analysis of the experiment is provided. Furthermore, the analysis of experimental data from the static test cases is performed and the σC_p-technique is applied to the dynamic test cases. In the last section of this chapter, the computational setup that was used in a different study to model the unsteady heat transfer in the airfoil model is described. The results from this simulation are analyzed in this study.

3.1. Wind tunnel experiment

A DSA-9A helicopter airfoil model with chord length $c = 0.3\,\mathrm{m}$ and span width $b = 0.997\,\mathrm{m}$ is measured in the open test section, closed-return "1MG" wind tunnel at DLR Göttingen. The freestream velocity is $U_\infty = 50\,\mathrm{m/s}$, corresponding to $Ma = 0.15$ and $Re = 1 \cdot 10^6$. The model is made of carbon-fibre reinforced epoxy and is pitching around its quarter-chord axis, driven from one side by an electric actuation mechanism, developed by Merz et al. [33]. The pitching motion is described by the equation $\alpha(t) = \alpha_0 - \alpha_1 \cdot \cos(2\pi \cdot f \cdot t)$ throughout this study. The airfoil model is equipped with circular end plates to improve the two-dimensionality of the flow. Additional components of the experimental setup are a spotlight with a power output of up to $H_L = 1500\,\mathrm{W}$ mounted next to a high-speed FLIR® *SC 7750L* infrared camera. Furthermore, the airfoil model is equipped with 50 fast-response Kulite® pressure sensors installed under the model surface that are sampled at $f_s = 200\,\mathrm{kHz}$ with a Dewetron® data acquisition sytem that simultaneously measures the current geometric angle of attack α with a laser triangulator system. The experimental setup is shown in a sketch and a photo in Fig. 3.1 below. The DSA-9A airfoil geometry and the locations of the pressure sensors are shown in Fig. 3.2.

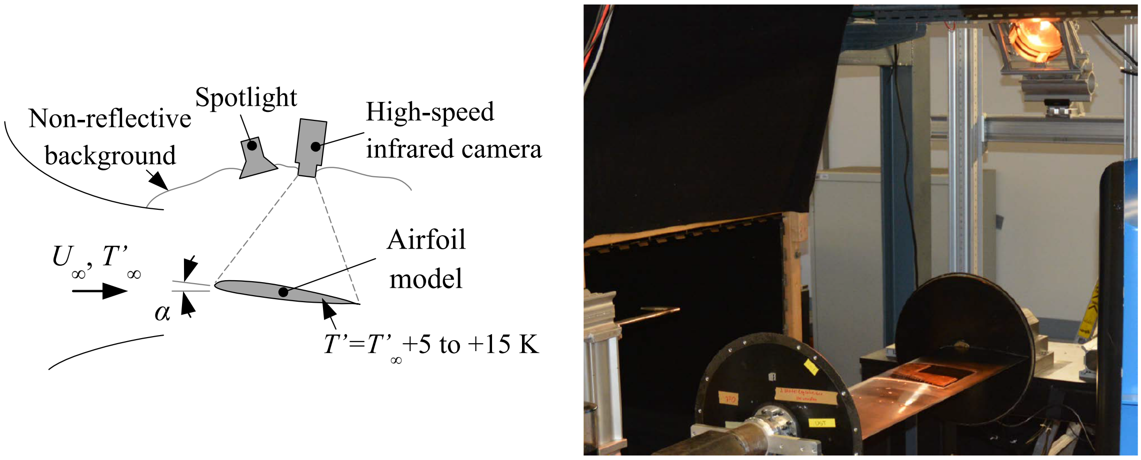

Figure 3.1: Experimental setup sketch (adapted from Wolf et al. [59], Fig. 2) and photo

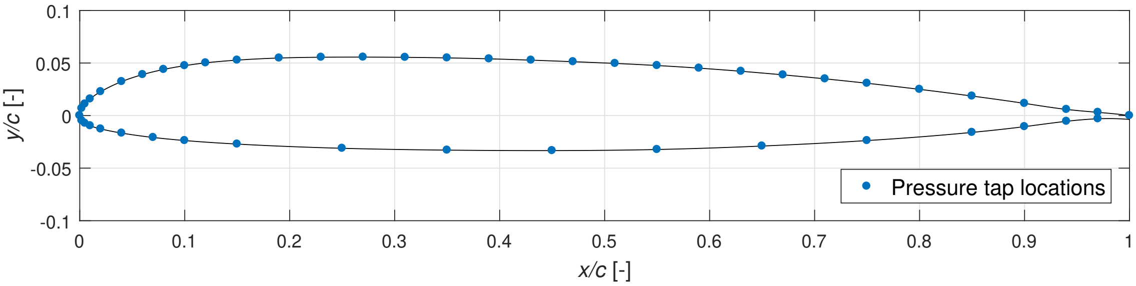

Figure 3.2: DSA-9A airfoil geometry with pressure tap locations

The positions of the pressure sensors were optimized with respect to the lift coefficient discretization error and are therefore more densely spaced near the leading edge, where the largest changes in the surface pressure gradient occur. The pressure taps are aligned diagonally with respect to the flow direction at an angle of 11° to reduce the influence of the surface roughness of the upstream taps on the measurements further downstream. For the static and dynamic test cases, the boundary layer transition location is determined from the pressure sensor signals with the σC_p-technique. The parameters for the static and dynamic experiments are summarized in Tab. 3.1. The calculation of the Fo-number is based on the material parameters of the airfoil model in Tab. 3.3. Note that five dynamic test cases could not be achieved, due to the limitations of the pitching mechanism. This concerns the highest frequency $f = 8$ Hz at the largest α_1 and the lowest f with $\alpha_1 = 4°$ and $\alpha_1 = 5°$. The test time for the dynamic experiments is 50 s, during which 5000 infrared images (511 × 636 pixels) of the model's suction surface are taken at an acquisition frequency of $f_s = 99.98$ Hz, slightly de-tuned from the integral multiples of the motion frequency. This allows the resolution of the motion period T with 5000 data points, when neglecting the differences between the individual motion periods. For the static test cases, the test time is 10 s and 1000 infrared images are taken. The high–speed infrared camera features a cadmium–mercury–telluride sensor, sensitive in the spectral range 8.0 µm to 9.4 µm. The camera was mounted 2 m above the airfoil model and equipped with a 50 mm focal length lens. The image integration time was set to 190 µs. For merging the infrared camera data with the data from the Dewetron® system, both devices are supplied with a reference voltage signal that is synchronized in post-processing so that the infrared images can be ordered ascending in phase. The airfoil model is externally heated with the spotlight to establish a temperature difference between the model and the flow. The radiative heat flux was measured with a power meter and is roughly $H_L = 1500\,\mathrm{W/m^2}$ over the upstream half of the chord and reducing to $H_L = 420\,\mathrm{W/m^2}$ near the trailing edge. This results in a temperature difference between the airfoil's upper surface and the freestream temperature of $T' - T'_\infty = 10$ K to 15 K for the dynamic test cases. The heating was reduced to a temperature difference between 5 K and 6 K in the static test cases. The radiation intensity I measured with the infrared camera on the airfoil's surface is typically around 10 000 counts. The conversion factor varies between 8.4 mK/count at $T' = 299$ K and 50 mK/count at $T' = 320$ K with a typical noise equivalent temperature difference of 35 mK given by the manufacturer [25]. However, the camera images were not temperature–calibrated for this study, since the employed measurement schemes do not rely on absolute temperature levels.

Parameter	Value or range
Freestream velocity U_∞	50 m/s
Freestream temperature T'_∞	302 K
Heating $T' - T'_\infty$	dynamic: 10 K ... 15 K, static: 5 K ... 6 K
Number of infrared images	dynamic: 5000, static: 1000
Mean angle α_0	dynamic: 4°, static: −4.5° ... 12.5°, $\Delta\alpha = 0.5°$
Pitch amplitude α_1	1°, 2°, 3°, 4°, 5°, 6°, 7°, 8°
Pitching frequency f	0.25 Hz, 0.5 Hz, 1 Hz, 2 Hz, 4 Hz, 8 Hz
Reduced frequency $k = (f \cdot \pi \cdot c)/U_\infty$	0.005, 0.009, 0.019, 0.038, 0.075, 0.151
Fourier number Fo	0.016, 0.008, 0.004, 0.002, 0.001, 0.0005

Table 3.1: Test matrix of the wind tunnel experiments

A single infrared image for the static test case with $\alpha = 1.5°$ is shown in Fig. 3.3. The flow direction is from left to right, darker regions are cooler. The leading edge and trailing edge can be identified as vertical lines against the cooler background ($\Delta I \approx -1500$ counts). An automated detection of the edges is used to map the streamwise coordinate x and scale it to the chord length c. In Fig. 3.3, the boundary layer transition region is identified with a blue rectangle. In this region, the radiation intensity gradually decreases due to the increased convective heat transfer of the turbulent boundary layer. The transition location is further upstream in three spanwise regions indicated by black arrow markers, this is expected to result from an increased surface roughness due to the pressure taps (central region) or silver-paint fiducial markers (upper/lower region). The area that is primarily analyzed in this study is marked by two green lines, it covers 30 pixels (ca. 1.6 cm) in the spanwise direction. The transition front is quasi-one-dimensional in this area, therefore the infrared signal is averaged along the spanwise direction to reduce the camera noise.

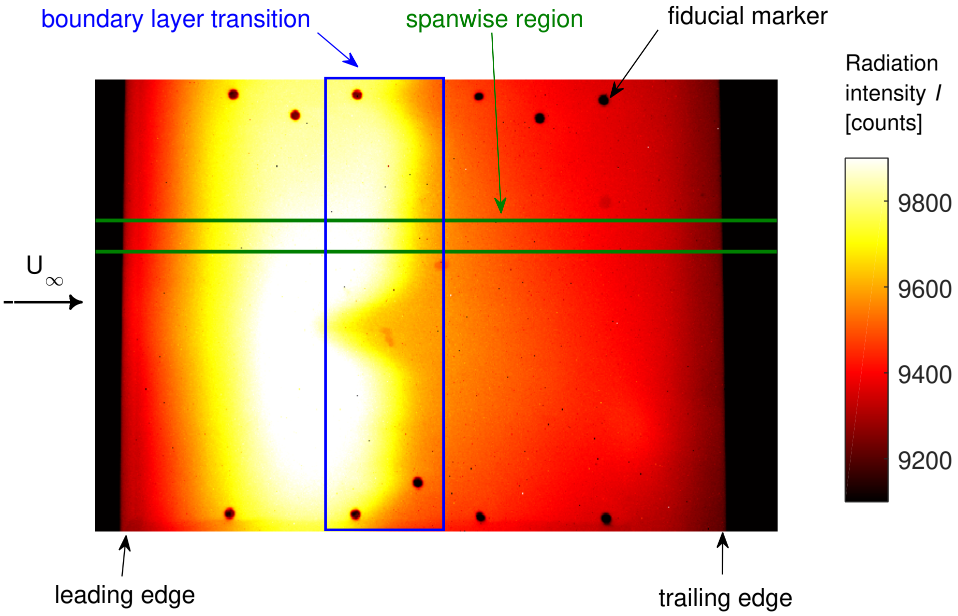

Figure 3.3: Sample static infrared image at $\alpha = 1.5°$, adapted from Wolf et al. [59], Fig. 3

The image processing procedure of the infrared images to streamwise intensity vectors $I(x/c)$ is described with the following five steps. For the static cases, these steps are performed on the temporal average over the 1000 images. For the dynamic cases, the steps are performed for each individual infrared image.

1. Treating erroneous pixels by replacing pixels with an intensity offset of more than $\Delta I > 40$ counts from the local median intensity with the value of the local median
2. Spanwise averaging of 30 pixel arrays in the model center (green lines in Fig. 3.3)
3. Model edge detection with minimum and maximum of the streamwise intensity gradient
4. Map the intensity vector to x/c with a linear spacing of 561 points from 0 to 1, equivalent to the average number of pixels over the chord length c in the infrared images
5. Smoothing of the intensity vector $I(x/c)$ with a moving average over $\pm 1\%$ of the chord length c

For the static test cases, the image processing procedure is completed after these steps. Five example intensity vectors $I(x/c)$ for different α are shown in Fig. 3.4. For the dynamic pitching cases, the level of camera noise in the processed intensity vectors is found to be larger by a factor of approximately 30. A factor of $1/\sqrt{1000} = 31.62$ would be expected for a normally distributed random error because of the temporal averaging of the static images. The random error in the intensity vectors from the dynamic cases is treated further in the next subsection. A systematic error is identified and corrected in the following.

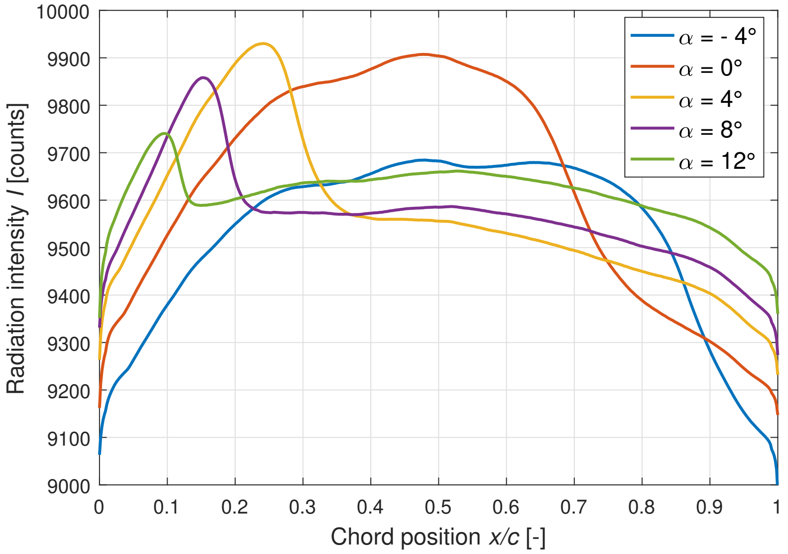

Figure 3.4: Static infrared image data processed to intensity vectors for five example α

The detuning of the camera acquisition frequency from the pitching frequencies means that the motion period T can be resolved with 5000 infrared images, equally spaced between $t/T = 0$ and $t/T = 1$, thus resulting in a resolution of $\Delta t/T = 1/4999 \approx 2 \cdot 10^{-4}$. This sampling rate would not be possible without the detuning and reordering. This procedure causes that subsequent points in the reordered signal have a large wall–clock time difference, and the signal is affected by a temperature drift. Figure 3.5 shows the temperature drift as function of x/c and the test time t for the dynamic test case with $\alpha_1 = 7°$ at $k = 0.075$. The drift was determined using a temporal low–pass filter which applies a sliding average window twice as large as the pitching period. The area between $x/c = 0.1$ and $x/c = 0.2$ cools down, whereas the area between $x/c = 0.3$ and $x/c = 0.9$ heats up. This non-uniform temperature drift is compensated for all dynamic test cases through the subtraction of a linear curve fit to the intensity data for each chordwise location over time.

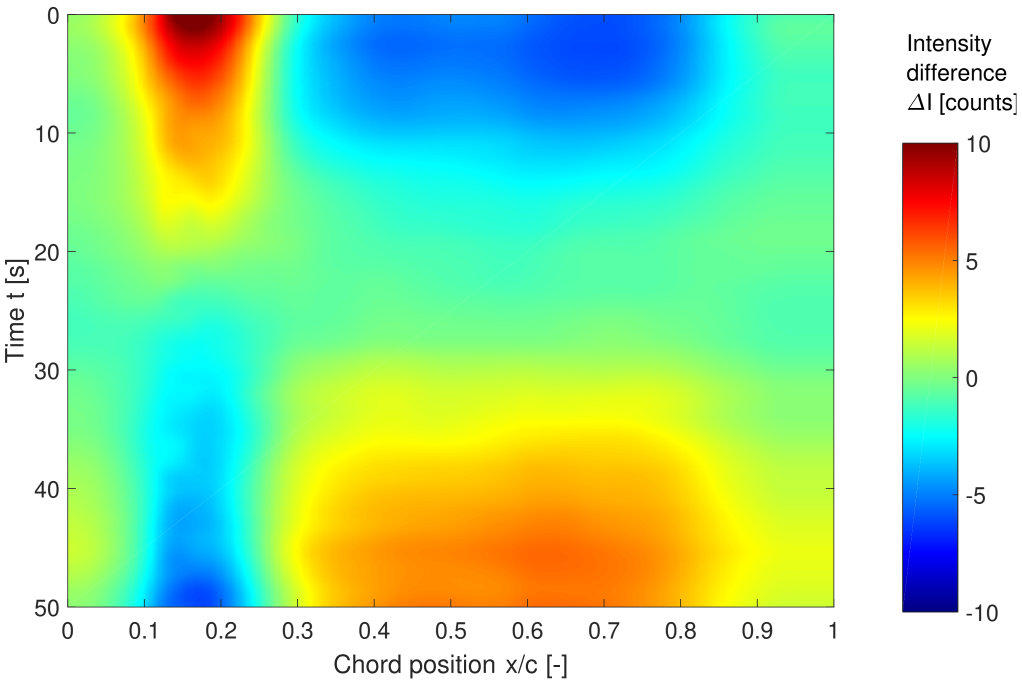

Figure 3.5: Non-linear temperature drift over time, adapted from Wolf et al. [59], Fig. 13

3.2. Static and dynamic airfoil behavior

The static boundary layer transition behavior for the DSA-9A airfoil in the “1MG” wind tunnel is determined with two different experimental techniques, σC_p and IRT. For the IRT measurements, the transition location is the x/c-position with the minimum of the radiation intensity gradient $\partial I/\partial(x/c)$. The results for both techniques are shown in Fig. 3.6. The IRT data points are fitted with a seventh order polynomial expression for α with x_{tr}/c as the indeterminate. The uncorrected geometric wind tunnel angles of attack α are used. Also shown are the transition onset and end obtained from the IRT data with a methodology after Schülein [48], where the interceptions of the tangent through the transition point in the intensity curve with the values of the nearest upstream and downstream local extremum or inflection point are extracted as transition onset and end, respectively. The σC_p data in Fig. 3.6 is in good agreement with the IRT data, however a systematic difference is observed when $x_{tr}/c > 0.6$. There, the σC_p-transition location is shifted upstream by around $\Delta x/c \approx -0.05$, compared to the IRT data. This is suspected to be caused by early triggered transition by upstream pressure taps. The σC_p data is located in the transitional region as identified with IRT for all α.

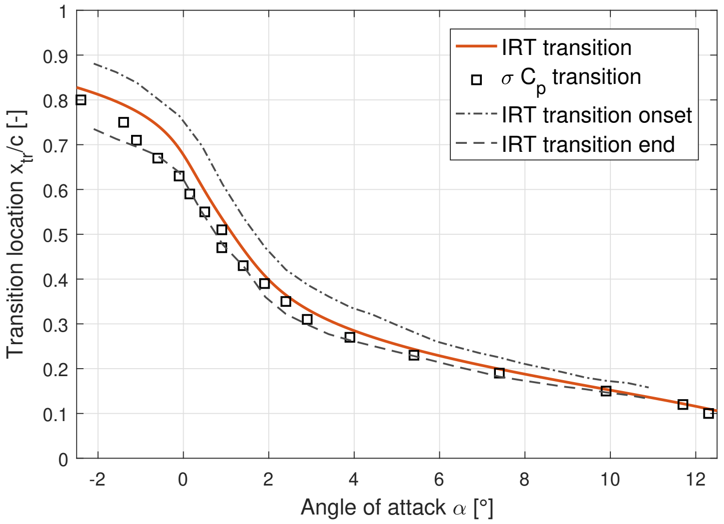

Figure 3.6: Static transition polar for the DSA-9A airfoil model in the “1MG” wind tunnel

The quasi-steady boundary layer transition locations can be obtained from the polynomial fitted to the static IRT measurements. Figure 3.7 shows the idealized pitching motion and the quasi-steady boundary layer transition results over the period for the eight pitching amplitudes α_1.

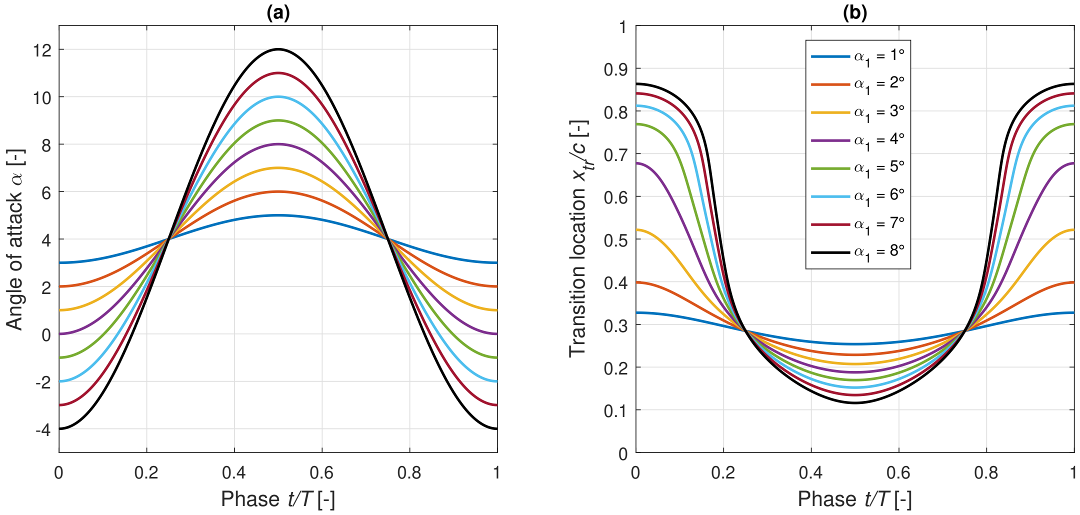

Figure 3.7: (a): Idealized $\alpha(t)$ for the dynamic test cases, (b): Corresponding quasi-steady transition locations

The measurement of the unsteady boundary layer transition location of the dynamic test cases with the σC_p-technique is following the procedure discussed in Sec. 2.2.2. For each of the 5000 IRT data points, the mean and the standard deviation σ of the surface pressure coefficient can be computed for each pressure sensor. The pressure sensors are sampled at a higher frequency than the infrared camera, such that 2000 pressure sensor measurements contribute to these statistics for each data point. The results for σC_p over the period for the dynamic test case with $\alpha_1 = 6°$ at $k = 0.075$ at the sensor location $x/c = 0.31$ is shown in Fig. 3.8. The transition instants can be detected as peaks in the signal. The measurement procedure is applied to all dynamic test cases for all sensor locations, the transition locations are saved whenever one or two peaks in the σC_p-signal can be identified.

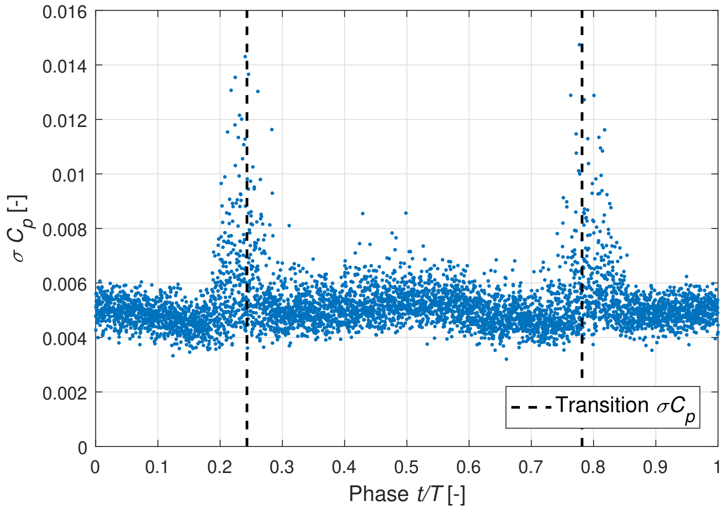

Figure 3.8: Application of the σC_p-technique to the pressure sensor located at $x/c = 0.31$ for the motion case with $\alpha_1 = 6°$ and $k = 0.075$

Figure 3.9 shows the frequency and amplitude effects of the dynamic pitching motion on the boundary layer transition location measured with the σC_p-technique. When compared to the quasi-steady results shown in Fig. 3.7b, the σC_p-results with different α_1 confirm that the quasi-steady analysis can give a good qualitative estimate of the expected unsteady transition behavior. The unsteady aerodynamics produce a phase lag of the transition movement with respect to the pitching motion, which increases with k. The σC_p-results are used as reference points for the unsteady boundary layer transition measurements with schemes based on the infrared thermography measurements. The comparison between the measurement schemes is performed in Sec. 6.2.

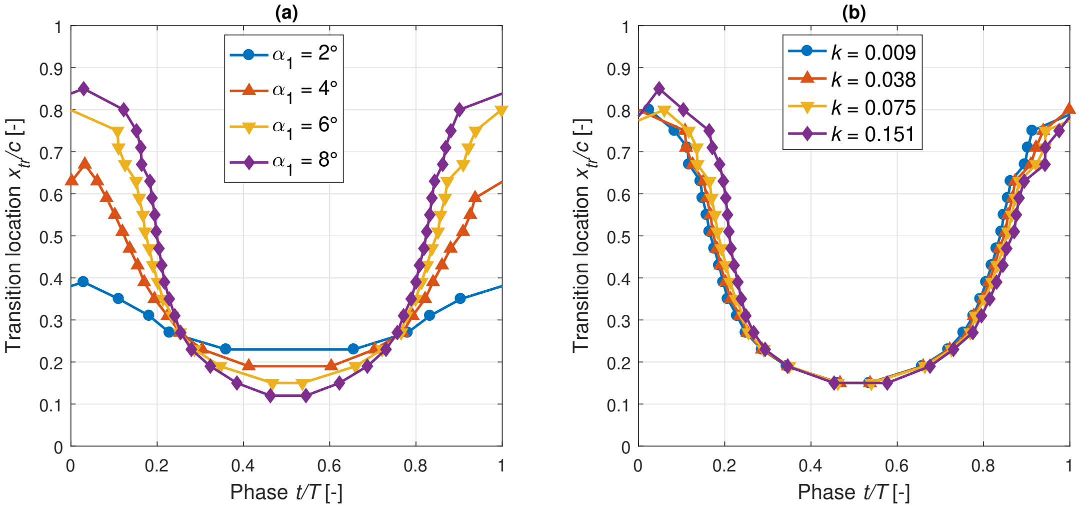

Figure 3.9: (a): Amplitude effects at $k = 0.038$ and (b): Frequency effects at $\alpha_1 = 6°$ on the unsteady boundary layer transition measured with the σC_p-technique

The last topic of this discussion of the dynamic airfoil behavior is the analysis of the signal-to-noise ratio $SNR = S/n$ of the infrared camera measurements. For the determination of the noise level n in the infrared camera measurements, two subsequent images at a static angle of attack are subtracted and the root-mean-square value (RMS) of the intensity difference image is computed. This value was found to be around 5 counts for several sample image pairs. Assuming that the spanwise averaging is performed over a region with identical aerodynamics and material properties, this noise level can be reduced by a factor of ca. $1/\sqrt{30} \approx 0.18$, therefore the noise level in the intensity vectors can be assumed to be ca. $n = 1$ count. The reference signal S for the dynamic pitching cases is determined by first taking the time trace of the processed intensity vectors $I(x/c)$ and computing the standard deviation σ over time for each chordwise entry. The average over the chord between $x/c = 0.05$ and $x/c = 0.95$ is then multiplied by two to account for the up- and downstroke of the motion and rounded to the nearest integer. The $SNR = S/1$ count is shown for all dynamic pitching cases of the test matrix in Tab. 3.2. A trend of increasing SNR with increasing α_1 and decreasing SNR with increasing k is observed for the entire range of parameters in this study.

	$k = 0.005$	$k = 0.009$	$k = 0.019$	$k = 0.038$	$k = 0.075$	$k = 0.151$
$\alpha_1 = 1°$	20	14	11	10	8	7
$\alpha_1 = 2°$	39	26	21	17	14	12
$\alpha_1 = 3°$	59	39	31	24	19	17
$\alpha_1 = 4°$	-	51	40	31	24	21
$\alpha_1 = 5°$	-	-	47	36	28	23
$\alpha_1 = 6°$	84	66	51	38	30	24
$\alpha_1 = 7°$	89	69	53	40	31	-
$\alpha_1 = 8°$	94	72	55	41	32	-

Table 3.2: SNR of the infrared data for the dynamic experiments

3.3. Unsteady heat transfer simulation

The simulation results analyzed in this study are produced with a coupled simulation of the unsteady aerodynamics of a pitching airfoil and a thermal FEM model of the airfoil's suction surface. The simulations are loosely coupled, which means that the CFD solution is computed first and the results are used as input to the thermal FEM model. The simulations have been set up and performed by Gardner et al. [20] and Eder [16], to whose works the reader is referred for more detailed information about the computational setup. The results of their study has been discussed in Sec. 2.2.3. Figure 3.10 shows the results for the lift coefficient C_ℓ and the transition location x_{tr}/c produced with this setup.

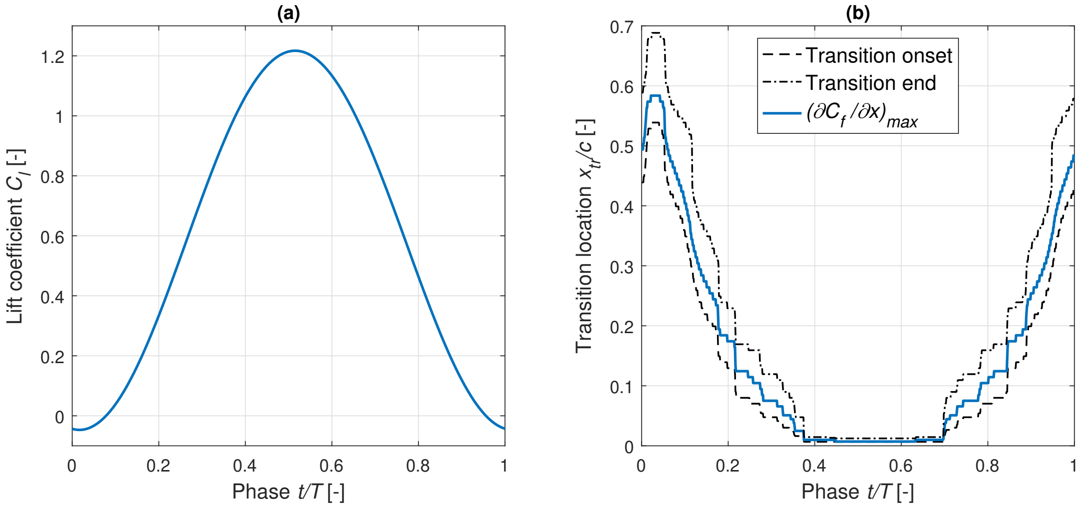

Figure 3.10: URANS simulation results for (a): Unsteady lift coefficient C_ℓ and (b): Unsteady boundary layer transition location

The CFD simulations with the DLR-TAU URANS code were performed to match and experiment described in detail by Richter et al. [44], which uses the same airfoil model as this study in a different wind tunnel. The flow conditions are $Ma = 0.30$ and $Re = 1.8 \cdot 10^6$ and the pitching motion is described with $f = 6.6\,\text{Hz}$, $\alpha_0 = 4.3°$ and $\alpha_1 = 6°$ in the CFD simulation. The unsteady boundary layer transition is modeled with an external solver based on the e^N-method with an amplification factor of $N = 10$, and then fed back to the flow solver for each time step. The C_p and C_f distributions are saved as results from the CFD simulation. The unsteady transition location is determined from the skin friction result $C_f(x)$, it corresponds to the location of the maximum gradient $(\partial C_f/\partial x)_{max}$. The transition onset and end are the nearest points where $\partial C_f/\partial x$ is zero. As visible in Fig. 3.10b, the way the occurrence of unsteady boundary layer transition is modeled in this setup together with the chosen discretization of the airfoil makes the transition propagate in steps corresponding to the grid discretization. The C_f-results are used to calculate the heat transfer by convection as input for the thermal FEM model. To represent the incoming heat flux from the spotlight H_L in the model, a constant heat source is modeled at the top element in the thermal model. The parameters for the thermal FEM simulation are summarized in Tab. 3.3 and the setup of the model is illustrated in Fig. 3.11. Following the discussion of Sec. 2.2.3, the major limitation of the thermal model is the simplification of the airfoil model composite material to a uniform material with the thermal properties of epoxy. The reference signal S for the simulation data is computed as $S = 0.1168\,\text{K}$.

Parameter	Value
Cells in vertical direction	800
Wall thickness	5.5 mm
Simulation time step	$5 \cdot 10^{-5}$ s
Thermal conductivity κ	0.5 W/(m K)
Heat capacity C_P	2300 J/(kg K)
Material density ρ	1180 kg/m^3
Lamp heat flux H_L	2000 W/m^2

Table 3.3: Thermal FEM simulation parameters, adapted from Gardner et al. [20], Tab. 1

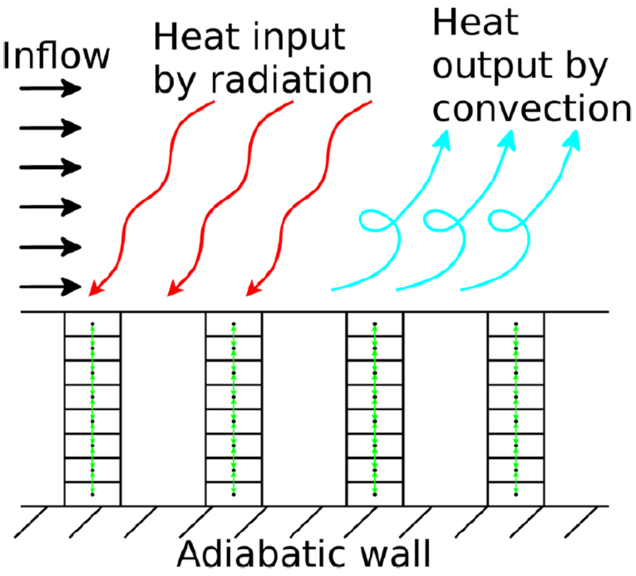

Figure 3.11: Schematic of the thermal FEM model, from Gardner et al. [20], Fig. 5

4

Optimization of differential infrared thermography

In the first section of this chapter, the application of differential infrared thermography (DIT) is briefly discussed for one example case. For the optimization of DIT documented in the third section of this chapter, the image separation time step $\Delta t/T$ is varied over a large range for every motion parameter combination in the test matrix. This requires the implementation of an automated post-processing procedure for the DIT results, which is introduced in the second section.

4.1. Application of DIT

After the image processing activities of the previous chapter are completed, the result is one intensity vector $I(x/c)$ per phase instant. The first step for applying DIT is selecting an image separation time step $\Delta t/T$. Then, the intensity vectors corresponding to the selected $\Delta t/T$ are subtracted. The value of the absolute maximum of the difference vector between $x/c = 5\,\%$ and $x/c = 95\,\%$ ("DIT peak") is saved as DIT signal ΔI and the respective chord position is saved as transition location x_{tr}/c. This procedure is illustrated for the example motion case with $\alpha_1 = 3°$ and $k = 0.038$ in Fig. 4.1. In Fig. 4.1a, two intensity distributions from the motion upstroke are shown. The $\Delta t/T$ is around 3 %, so that the instantaneous incidence angles are $\alpha_a = 4°$ (solid line) and $\alpha_b = 4.5°$ (dashed line). The analysis of the intensity difference in Fig. 4.1b allows to identify the distinct DIT peak.

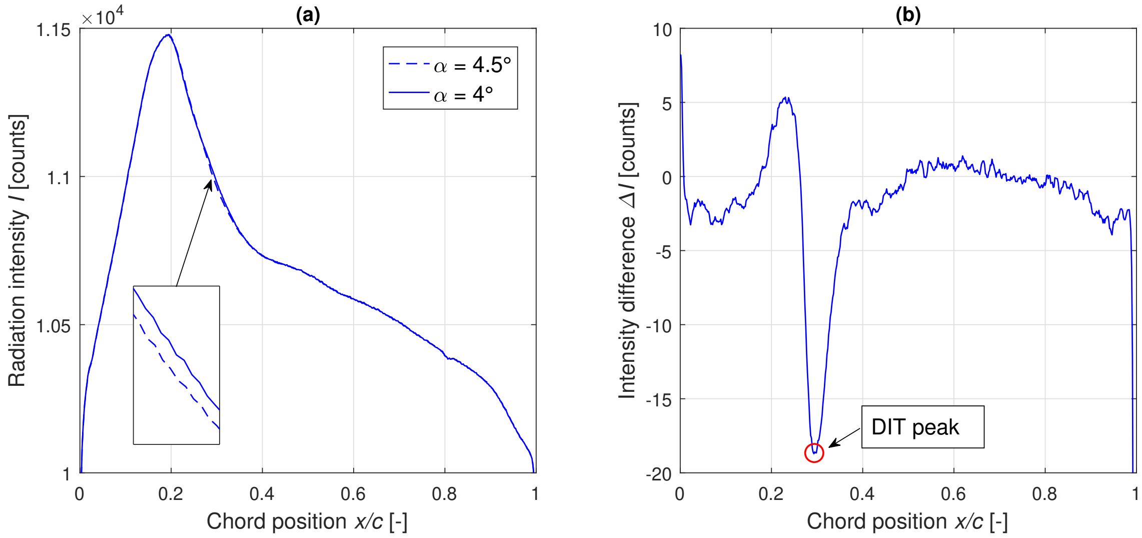

Figure 4.1: Example case for the application of DIT with $\alpha_1 = 3°$ at $k = 0.038$:
(a) two intensity distributions with $\Delta t/T \approx 0.03$, (b) intensity difference with DIT peak

The resulting values for the DIT signal ΔI and the transition location x_{tr}/c from the detected DIT peak are allocated to the average value of the phase t/T of the two subtracted intensity distribution, producing 4999 evenly distributed data points. This is a slight modification of the original DIT procedure from the literature, where the values of α are averaged. The selection of $\Delta t/T$ determines the signal strength ΔI of the DIT peak and also has a considerable effect on the transition measurement. In the literature discussed in Sec. 2.2.3, it is suggested that the ideal value of $\Delta t/T$ and thus ΔI would be as small as possible, with a still discernible DIT peak. In Fig. 4.1b, it can be observed that a lower limit for ΔI exists, after which the location of the DIT peak is randomly and/or systematically different from the boundary layer transition location x_{tr}/c.

4.2. DIT post-processing procedure

The setup of the automated post-processing procedure of the DIT data points is discussed in this section for an example motion case in the center of the test matrix, where $\alpha_1 = 4°$ and $k = 0.038$. In all figures, the steps of the procedure are illustrated for two example image separation time steps, for $\Delta t/T = 0.005$ and for $\Delta t/T = 0.05$. Figure 4.2 shows the raw (unprocessed) transition measurement result over phase t/T obtained from DIT with the two example image separation time steps. Each dot represents the x_{tr}/c result for one image pair.

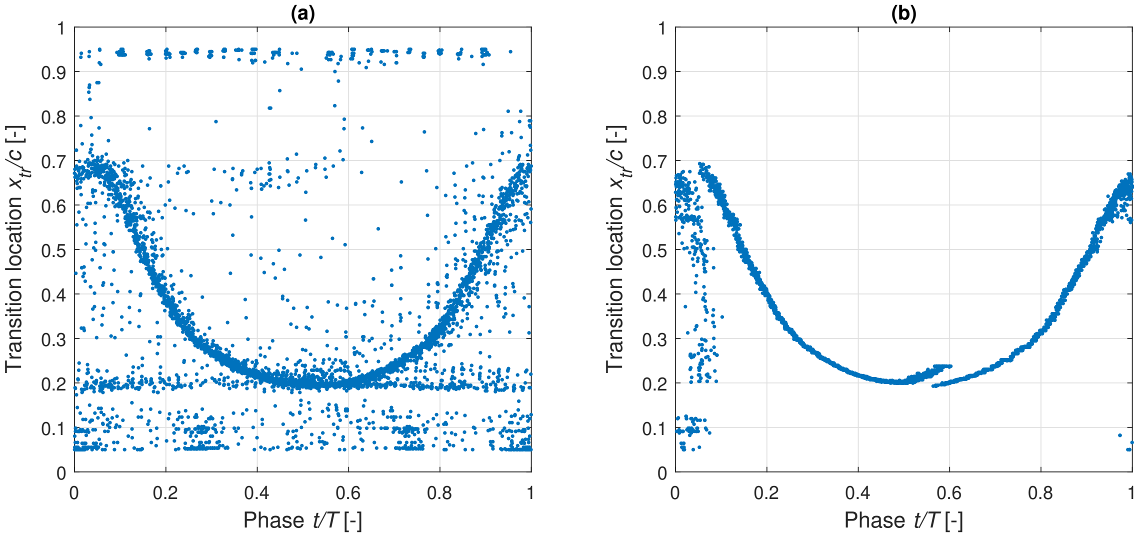

Figure 4.2: Unprocessed DIT transition measurement results over phase:
(a) time step $\Delta t/T = 0.005$, (b) time step $\Delta t/T = 0.05$

The two graphs of Fig. 4.2a and b reveal that the result obtained with the smaller $\Delta t/T$ is flawed mostly by random measurement errors, whereas the result with the larger $\Delta t/T$ is mostly flawed by systematic errors near the motion turning points. For $\Delta t/T = 0.005$, the erroneous data points are spread across the entire period and the entire chord length, and many data points yield a transition location on the first 20 % of the chord. Some data points also accumulate far downstream near the trailing edge. The observations can be explained by the reducing signal strength of the DIT peak signal for small $\Delta t/T$. The clearly erroneous data points for $\Delta t/T = 0.05$ in Fig. 4.2b are limited in phase to the motion turning points around $t/T = 0$ and $t/T = 0.5$.

The DIT signal strength ΔI is shown over the period for the two example time step sizes in Fig. 4.3. For the small $\Delta t/T$, the value of ΔI is at the order of magnitude of the random measurement error, which can be identified in Fig. 4.3a as the edges of a “white belt” around $\Delta I = 0$. The value of ΔI is expected to be negative for the forward moving transition during the motion upstroke $t/T < 0.5$ and positive for $t/T > 0.5$.

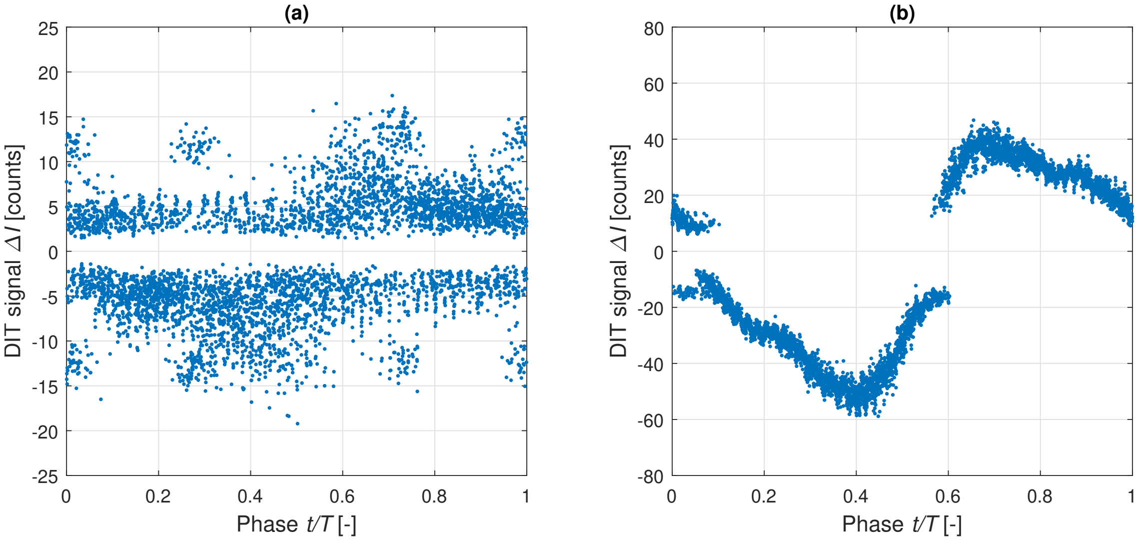

Figure 4.3: Unprocessed DIT signal measurement results over phase:
(a) time step $\Delta t/T = 0.005$, (b) time step $\Delta t/T = 0.05$

The following five steps are performed to filter the erroneous data points from the DIT results:

1. Identify the two segments of the period where the transition front is moving forward or backward manually from a small $\Delta t/T$ raw DIT transition measurement result
2. Remove the DIT data points where the two subtracted data points are not from the same segment
3. Remove results where the sign of ΔI is not matching the transition movement
4. Sanity check the produced x_{tr}/c result with the quasi-steady transition location from Sec. 3.2. Maximum allowed difference: $\Delta x_{tr}/c = \pm 0.25$
5. Apply signal threshold for the DIT data points: Minimum signal in the data set plus 5 counts

The filtered transition measurement results following this procedure and the corresponding DIT signal are shown in Figs. 4.4 and 4.5.

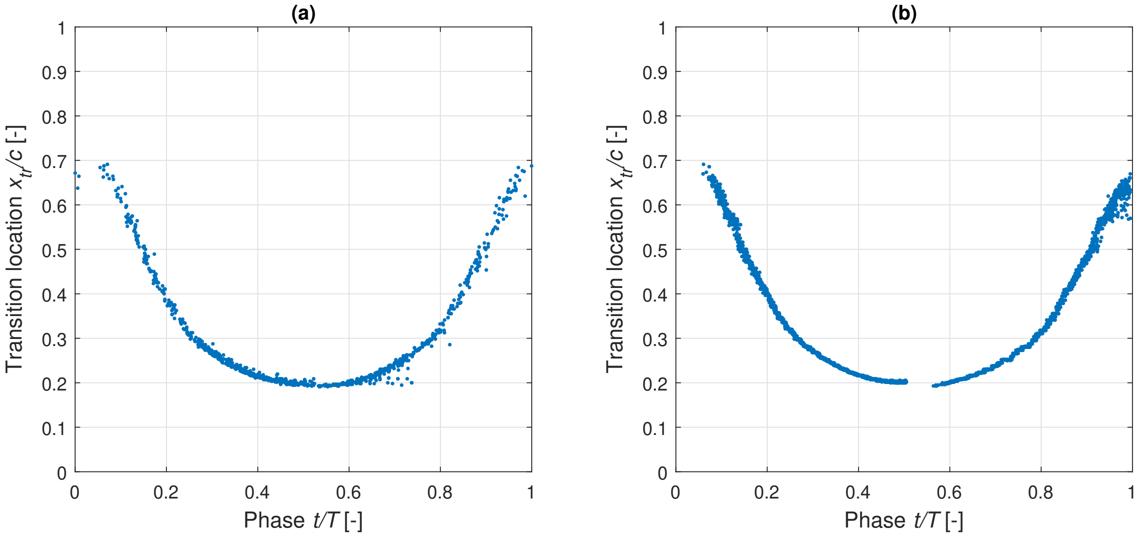

Figure 4.4: Filtered DIT transition measurement results over phase:
(a) time step $\Delta t/T = 0.005$, (b) time step $\Delta t/T = 0.05$

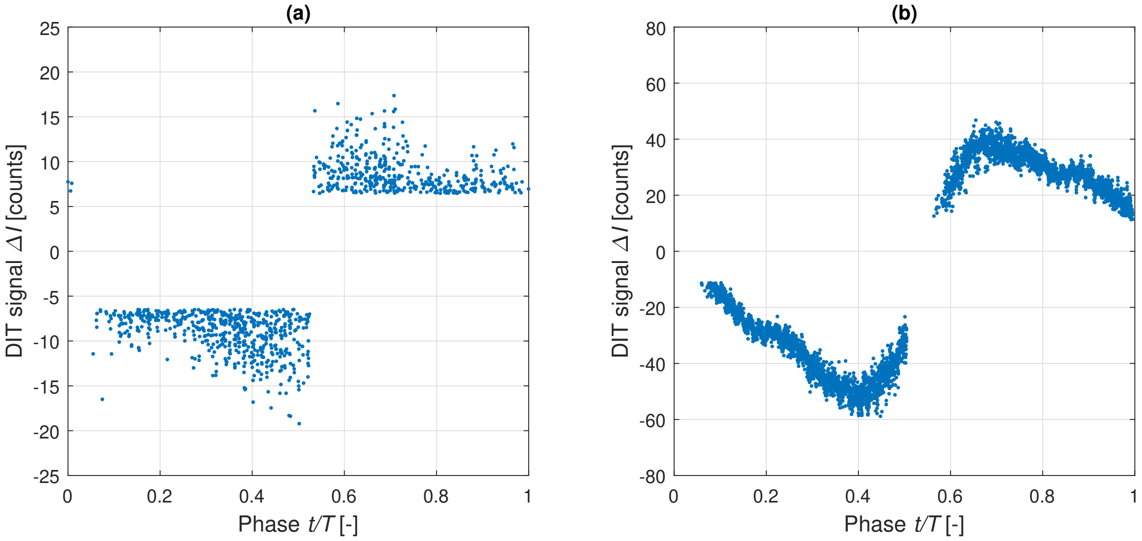

Figure 4.5: Filtered DIT signal measurement results over phase:
(a) time step $\Delta t/T = 0.005$, (b) time step $\Delta t/T = 0.05$

The filtered DIT transition measurement results are grouped into 100 bins, equally spaced over the period from $t/T = 0$ to $t/T = 0.99$ with a span of ± 0.005. A discrete-continuous transformation is applied to the filtered DIT transition measurement data points, each individual data point is assigned to a Gaussian probability density function p_i:

$$p_i(x \mid \mu', \sigma^2) = \frac{1}{\sqrt{2\pi\sigma^2}} e^{-\frac{(x-\mu')^2}{2\sigma^2}}$$

with the statistical mean being the respective DIT result for the data point $\mu' = x_{tr}/c$ and a fixed standard deviation of $\sigma = 0.01$ for all data points. All functions p_i are summed for each individual bin to a function $P(x/c)$ and normalized such that the theoretical maximum value of P for each bin is $P = 1$, if all DIT data points were valid (no effect of the filtering) and at the exact same location x/c. Figure 4.6 shows the resulting normalized probability density functions $P(x/c)$ for five example bins, applied to the two example $\Delta t/T$.

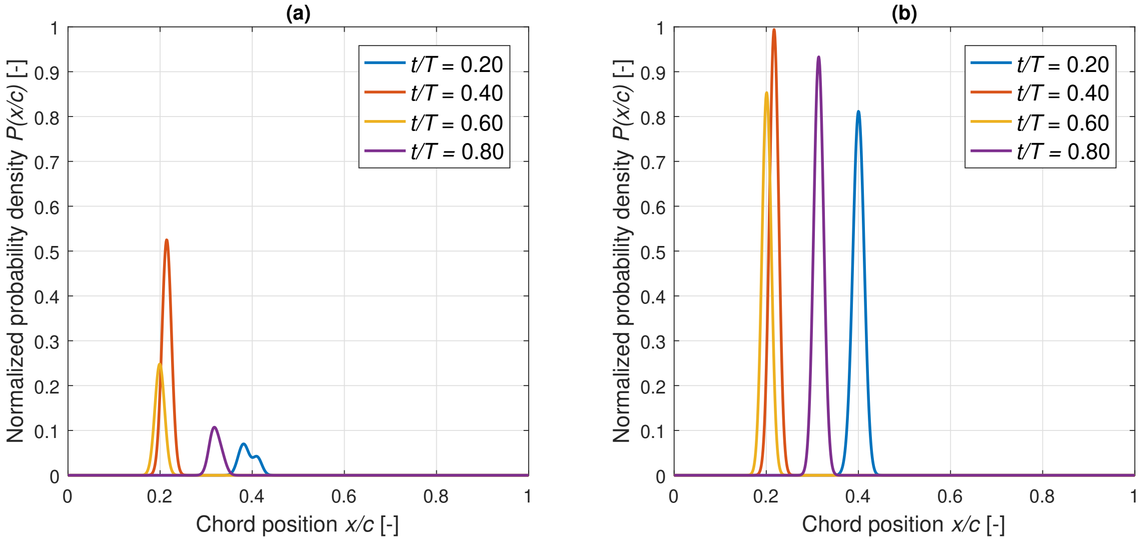

Figure 4.6: Normalized probability density functions for five bins:
(a) time step $\Delta t/T = 0.005$, (b) time step $\Delta t/T = 0.05$

The post-processed DIT transition locations $x_{tr}/c(t/T)$ produced with this approach are the x/c-locations with the maximum value of $P(x/c)$ for each of the 100 bins. No value for x_{tr}/c is saved when the value of $P_{max}(t/T)$ is smaller than 10% of the median value of P_{max} over the period for the respective $\Delta t/T$. A median filter with window size 3 is applied to the $x_{tr}/c(t/T)$ result to remove single outliers. The final processed result for the transition location over phase is shown for the two example $\Delta t/T$ in Fig. 4.7 below. The quasi-steady boundary layer transition location over phase for the case $\alpha_1 = 4°$ is shown in the plots as a reference.

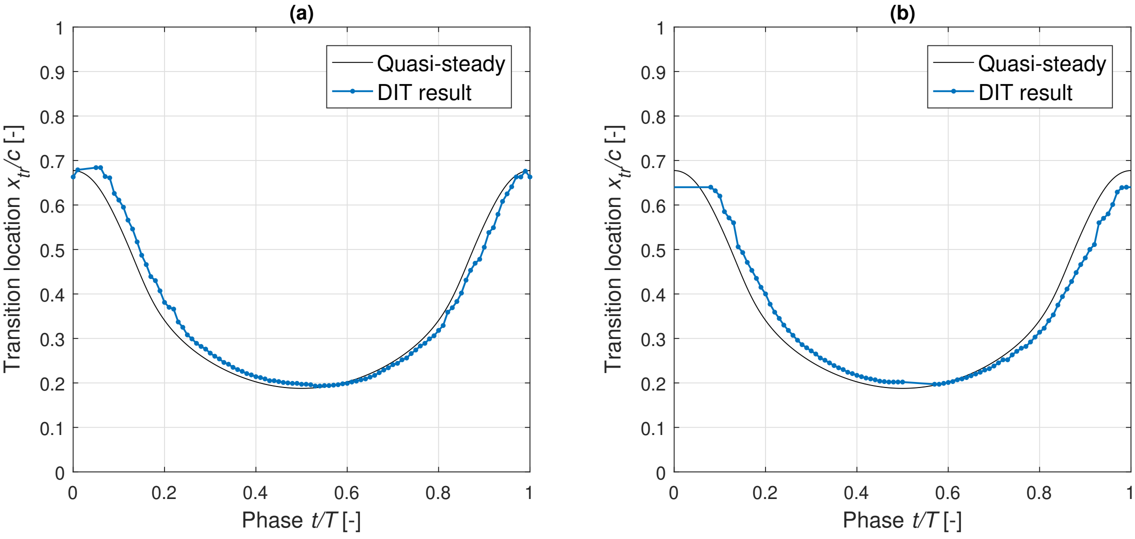

Figure 4.7: Post-processed DIT transition measurement results over phase, with quasi-steady transition for reference: (a) time step $\Delta t/T = 0.005$, (b) time step $\Delta t/T = 0.05$

The values of the peaks P_{max} of the normalized probability density $P(x/c)$ that correspond to the transition measurement for each bin are shown in Fig. 4.8 for the two example $\Delta t/T$. Considerably more valid data points (approx. by a factor of 4) are found for the larger $\Delta t/T$. This observation is quantified with the certainty parameter C, defined as the average of P_{max} over the period. The parameter C is therefore related to the DIT signal strength ΔI for the respective test case and the chosen image separation time step $\Delta t/T$.

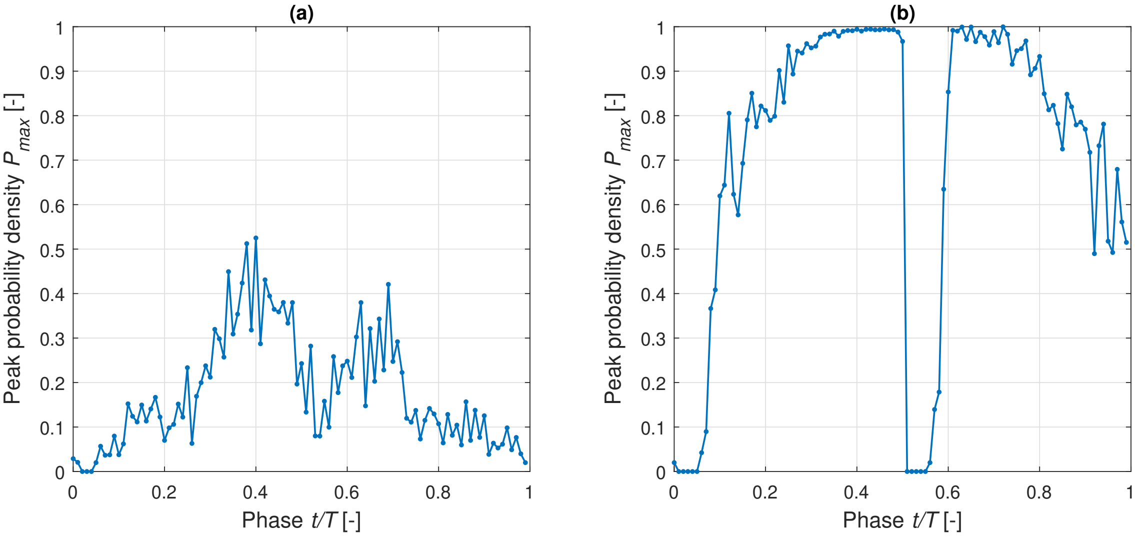

Figure 4.8: Peak probability density P_{max} for the 100 bins over the period: (a) time step $\Delta t/T = 0.005$, (b) time step $\Delta t/T = 0.05$

The parameter C is plotted for various $\Delta t/T$ and various pitching motion amplitudes and frequencies in Fig. 4.9. A steep rise in C from smallest $\Delta t/T$ is observed in all shown cases, reaching an approximately constant level for $\Delta t/T > 0.03$. For comparison, the maximum value of C is determined for all cases in the test matrix and shown in Tab. 4.1. For the range of parameters in the test matrix, the maximum value of C is decreasing with increasing k and decreasing with increasing α_1.

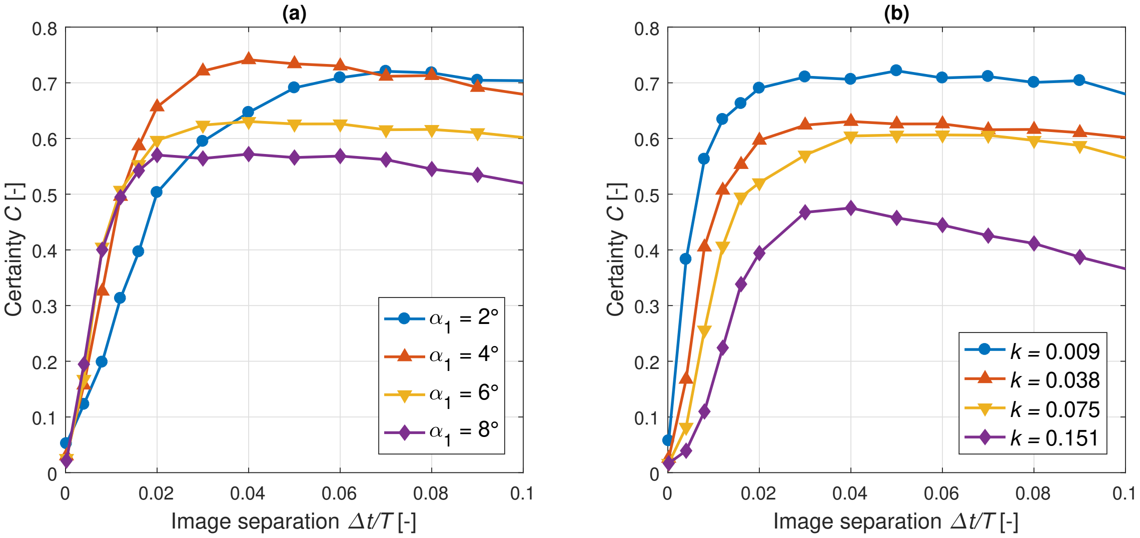

Figure 4.9: (a): Amplitude effects at $k = 0.038$ and (b): Frequency effects at $\alpha_1 = 6°$ on the certainty parameter C for various $\Delta t/T$

	$k = 0.005$	$k = 0.009$	$k = 0.019$	$k = 0.038$	$k = 0.075$	$k = 0.151$
$\alpha_1 = 1°$	0.74	0.80	0.76	0.63	0.52	0.42
$\alpha_1 = 2°$	0.83	0.81	0.78	0.72	0.60	0.46
$\alpha_1 = 3°$	0.85	0.83	0.82	0.78	0.69	0.55
$\alpha_1 = 4°$	-	0.80	0.78	0.74	0.68	0.52
$\alpha_1 = 5°$	-	-	0.71	0.68	0.63	0.48
$\alpha_1 = 6°$	0.74	0.72	0.68	0.63	0.61	0.48
$\alpha_1 = 7°$	0.71	0.69	0.66	0.60	0.57	-
$\alpha_1 = 8°$	0.68	0.68	0.64	0.58	0.56	-

Table 4.1: Value of maximum certainty C for all dynamic test cases

4.3. Optimization of the DIT image separation time step

From the published literature on DIT presented in Sec. 2.2.3, it is expected that the optimization of the DIT image separation time step $\Delta t/T$ is a compromise between the DIT signal strength ΔI (or the confidence parameter C) and the systematic time lag measurement error of the DIT technique. The DIT measurement phase lag sum ΔT_{1+2} is shown over the varying image separation time step size $\Delta t/T$, for various motion frequencies k and amplitudes α_1 in Fig. 4.10. The phase lag sum ΔT_{1+2} is the sum of the phase differences between the DIT transition measurement result and the quasi-steady reference during mid-upstroke (ΔT_1) and mid-downstroke (ΔT_2), i.e. when $x_{tr}/c = 0.285$.

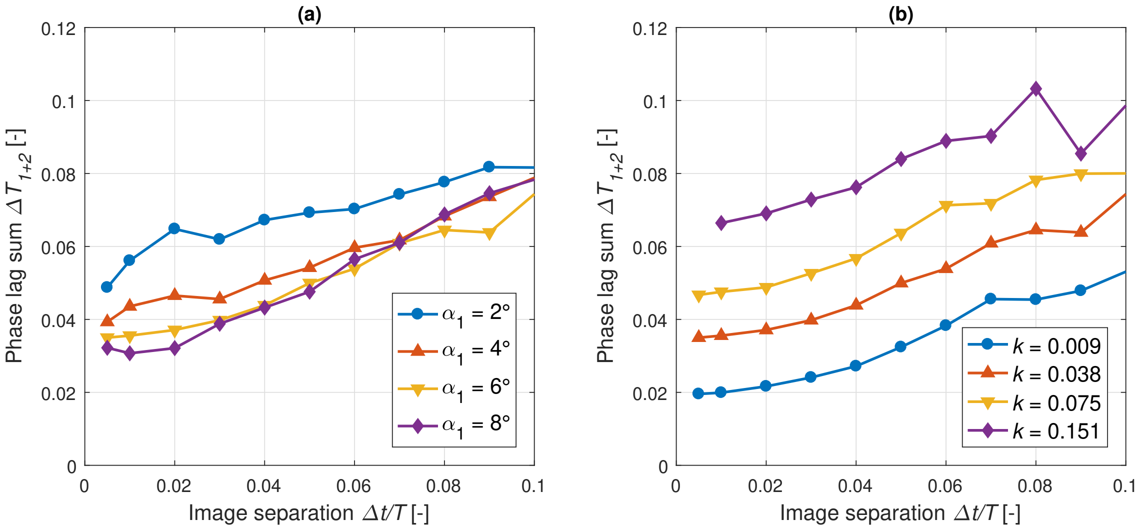

Figure 4.10: (a): Amplitude effects at $k = 0.038$ and (b): Frequency effects at α_1 = 6° on the DIT measurement phase lag sum ΔT_{1+2} for various $\Delta t/T$

Figure 4.10 confirms the assertion from Gardner et al. [20], that the DIT measurement phase lag is systematically increasing with increasing DIT image separation time step. This trend is found with a very similar slope of $\partial(\Delta T_{1+2})/\partial(\Delta t/T)$ for all frequencies and amplitudes in Fig. 4.10 over a large range of $\Delta t/T$. Only for the smallest image separations $\Delta t/T < 0.01$, the lag ΔT_{1+2} appears to remain approximately constant. Note that in this region, the value of ΔT_{1+2} also seems to be affected by some random scatter, or even returns no reasonable value at all for $k = 0.151$. Considering the results for the certainty parameter C shown in Fig. 4.9, this behavior is expected because the number of valid data points is rapidly decreasing towards zero for the smallest values of $\Delta t/T$. This observation is also in good agreement with the discussion of the literature in Sec. 2.2.3, as it is shown that it is only useful to decrease $\Delta t/T$ down to a level where the transition location measurement can be performed with a reasonable level of certainty.

At this point, the optimization procedure of the DIT image separation time step $\Delta t/T$ is defined. The smallest available $\Delta t/T$ that first exceeds 80% of the maximum value of C was used as ideal $\Delta t/T$ for each pitching motion case. The ideal time step size resulting from using this criterion for the optimization is shown for all pitching motion cases of the test matrix in Tab. 4.2 below. For most of the test points, the optimized time step size is around the value of $\Delta t/T \approx 1\%$, only the highest frequencies k at the smallest amplitudes α_1 require much larger time step sizes. A time step size of $\Delta t/T = 1\%$ is therefore recommended for future DIT experiments with similar experimental parameters, when performing another optimization is not possible. This result was also found and published by Wolf et al. [59] in the related DIT study of the same experiment.

	$k = 0.005$	$k = 0.009$	$k = 0.019$	$k = 0.038$	$k = 0.075$	$k = 0.151$
$\alpha_1 = 1°$	1.50	2.00	2.60	3.38	4.00	6.28
$\alpha_1 = 2°$	1.24	1.38	1.76	2.74	3.28	3.56
$\alpha_1 = 3°$	1.00	1.22	1.52	2.00	2.58	3.02
$\alpha_1 = 4°$	-	1.08	1.34	1.62	2.10	2.76
$\alpha_1 = 5°$	-	-	1.10	1.30	1.76	2.02
$\alpha_1 = 6°$	0.82	0.88	1.00	1.18	1.56	1.88
$\alpha_1 = 7°$	0.74	0.78	0.86	1.00	1.38	-
$\alpha_1 = 8°$	0.70	0.76	0.80	1.04	1.24	-

Table 4.2: Optimized image separation time steps $\Delta t/T$ for all dynamic test cases in percents

In Fig. 4.11, several DIT transition measurement results obtained with the optimized $\Delta t/T$ are shown, including the variation of the pitching motion frequency k and amplitude α_1. The results shown in Fig. 4.11 display that a rather large part of the motion period T does not contain any DIT transition measurement result. This concerns primarily the part of the motion period near the downstream turning point of the transition motion, around $t/T = 0$. Here, the boundary layer transition location is in the region on the airfoil model with decreased heating and slowly moving transition. This indicates that the optimization of the DIT image separation time step to reduce the phase lag in the parts of the pitching motion period with the fastest transition movement results in a failure of the DIT algorithm in the parts of the period with the slowest transition movement.

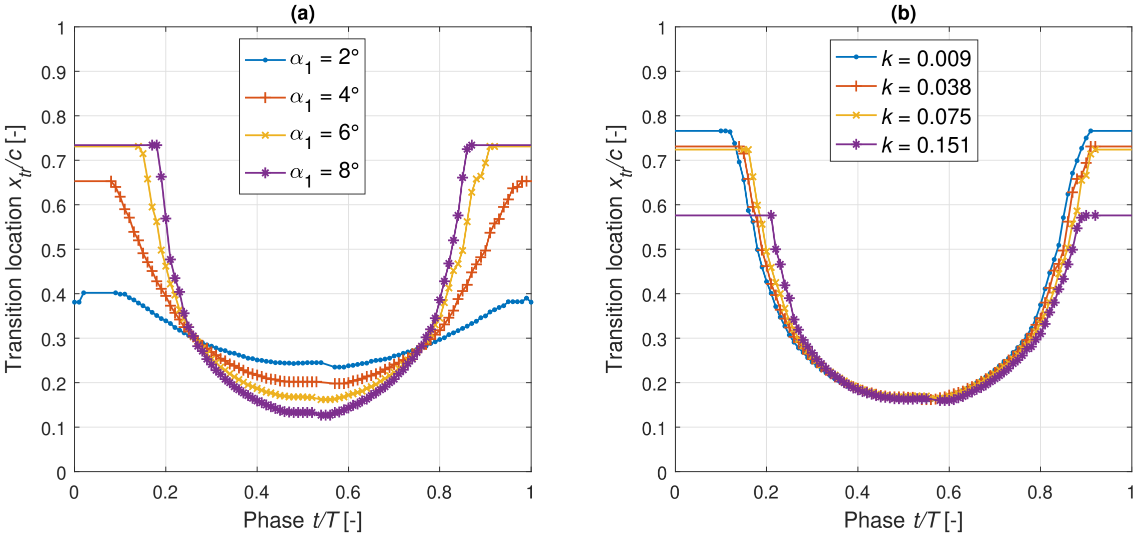

Figure 4.11: (a): Amplitude effects at $k = 0.038$ and (b): Frequency effects at α_1 = 6° on the DIT transition measurement result with the optimized $\Delta t/T$

5

Development of alternative transition measurement schemes

The goal of this chapter is to find improved data processing schemes for detecting unsteady boundary layer transition based on measurements with infrared thermography. The first idea for a new measurement scheme is to design an adaptive approach to the DIT image separation time step. The second idea is to analyze the measurements at fixed locations on the airfoil model surface individually, instead of looking for global effects like with DIT. The two ideas are developed into measurement schemes in the latter two sections of this chapter. The developments are based on a simplified quasi-steady model of the DIT technique and on the analysis of numerical simulation results, as discussed in the first section of this chapter.

5.1. Preliminary steps

5.1.1. Quasi-steady DIT model

The quasi-steady model for DIT is the application of the DIT methodology on the quasi-steady behavior of the transition location. The static transition location, the quasi-steady DIT model transition location and the result from the application of DIT to the static experimental data is shown in Fig. 5.1a. The DIT transition measurement results in Fig. 5.1a are the x/c-locations where the maximum difference in the two subtracted static α intensity distributions occurs. As second part of the design of the quasi-steady DIT model, the value of the maximum absolute intensity difference (the DIT signal ΔI) is predicted. An analytical expression for ΔI is derived by assuming that the subtracted intensity distributions are very similar. Then, the maximum difference ΔI is identical to the slope of the intensity distribution $\partial I/\partial(x/c)$ at the mean α, times the transition movement over the chord length during the DIT time step:

$$\Delta I = -\frac{\partial I}{\partial(x/c)}_{x=x_{tr}} \cdot \frac{\partial x_{tr}/c}{\partial \alpha} \cdot \Delta\alpha \tag{5.1}$$

To test the quasi-steady DIT model expression for ΔI of Eq. 5.1, Fig. 5.1b compares the model ΔI to the experimental ΔI, corresponding to the static DIT transition measurements shown in Fig. 5.1a.

Figure 5.1a shows a good agreement between the transition locations obtained by the three methods. A small error arises in the α-region where the absolute value of $\partial^2(x_{tr}/c)/\partial\alpha^2$ is largest (near $\alpha = -0.5°$ and $\alpha = 2.5°$), due to the piecewise linear reconstruction of α in the DIT methodology. The comparison of the quasi-steady DIT model prediction for ΔI with the experimental DIT signal data points in Fig. 5.1b shows a good agreement, but the absolute value of ΔI is overestimated by the model in the region $0° < \alpha < 2°$. This can be explained with a relatively large value of $\partial(x_{tr}/c)/\partial\alpha$ in this region, which makes the basic model assumption of the similarity between the intensity distributions break down.

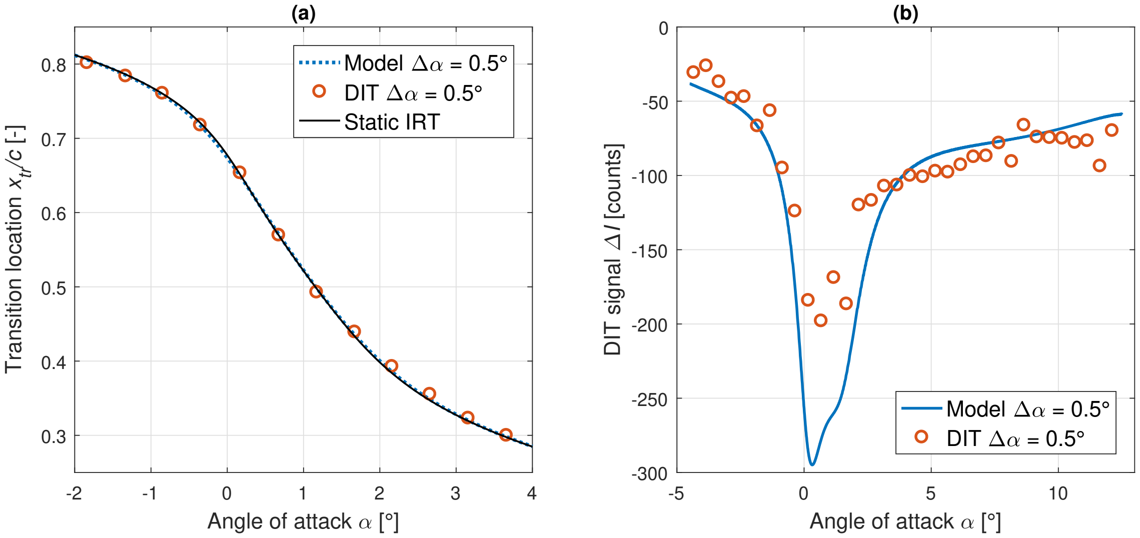

Figure 5.1: Quasi-steady DIT model and validation with experimental data:
(a) IRT/DIT transition location, (b) DIT signal strength

The quasi-steady DIT model is applied to the case $\alpha_1 = 4°$ with three different $\Delta t/T$ in Fig. 5.2. In Fig. 5.2a, the error in the transition measurement due to the piecewise linear reconstruction is observed in a small extent only for the largest selected $\Delta t/T$. The effect of the $\Delta t/T$- variation on the modeled DIT signal in Fig. 5.2b is larger, as it scales linearly with the corresponding $\Delta\alpha$, see Eq. 5.1.

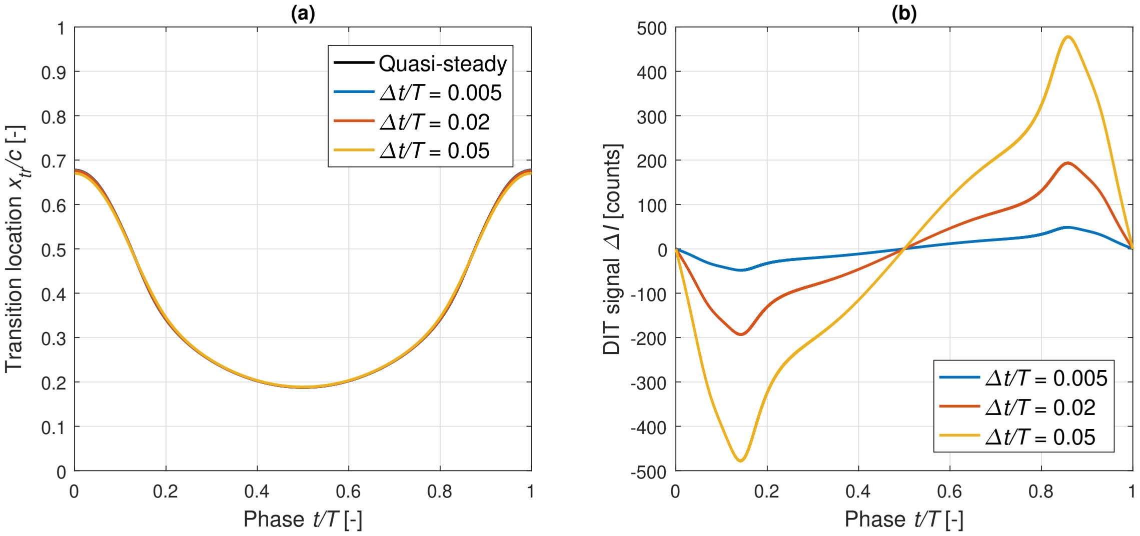

Figure 5.2: Effects of varying $\Delta t/T$ in the quasi-steady DIT model:
(a) effect on modeled DIT transition location, (b) effect on the modeled DIT signal

A noise threshold t_n is introduced as a cutoff signal strength for the DIT model signal ΔI, below which no transition measurement result is returned. To determine suitable values for t_n, the signal-to-noise ratios of Tab. 3.2 are used. Since the methodology for calculating S in Sec. 3.2 cannot be directly transferred to the quasi-steady data, the signal for this data is called pseudo-signal S^* and is shown in Tab. 5.1. The pseudo-signals are computed from a quasi-steady intensity matrix, assembled with static intensity distributions from the nearest static α for the quasi-steady pitching motion.

	$\alpha_1 = 1°$	$\alpha_1 = 2°$	$\alpha_1 = 3°$	$\alpha_1 = 4°$	$\alpha_1 = 5°$	$\alpha_1 = 6°$	$\alpha_1 = 7°$	$\alpha_1 = 8°$
$k = 0$	42	86	140	186	206	212	211	206

Table 5.1: Pseudo-signals for the quasi-steady DIT model test cases

The values for the pseudo-signal S^* of Tab. 5.1 are used to compute appropriate values for t_n for each α_1. The signal-to-noise ratio is varied from $2 < SNR < 100$ in the following analysis. The noise threshold is equal to the noise level, $n = S/SNR = t_n$. The implementation of the noise threshold t_n produces an additional source of error in the quasi-steady DIT model transition results, because x_{tr}/c can not be measured when $\Delta I < t_n$ for a given data point.

As transition measurement error, the RMS of the difference between the quasi-steady transition and the DIT model transition is computed:

$$\epsilon_{RMS} = \sqrt{\sum_{i=1}^{4999} (x_{tr}/c_{i,QS} - x_{tr}/c_{i,mod})^2/4999} \tag{5.2}$$

When no x_{tr}/c value is returned for a certain phase instant because $\Delta I < t_n$, the x_{tr}/c-value for the calculation of ϵ_{RMS} is linearly interpolated from the x_{tr}/c of the previous and next data point where $\Delta I > t_n$.

The behavior of the transition measurement error ϵ_{RMS} over the DIT image separation time step $\Delta t/T$ is shown in Fig. 5.3 for the quasi-steady pitching amplitude $\alpha_1 = 4°$ with three example SNR. The idealized case of $t_n = 0$ ($SNR = \infty$) is shown for reference. It can be seen that the introduction of the threshold t_n only has an effect on ϵ_{RMS} for the smallest time steps, $\Delta t/T < 0.02$ for the selected values of the SNR. For the smallest $\Delta t/T$ towards zero, t_n produces a steep rise in ϵ_{RMS}, as an increasing amount of data points are removed from the measurement result by the noise threshold. The range of $\Delta t/T$ where this steep rise is observed depends on the respective SNR.

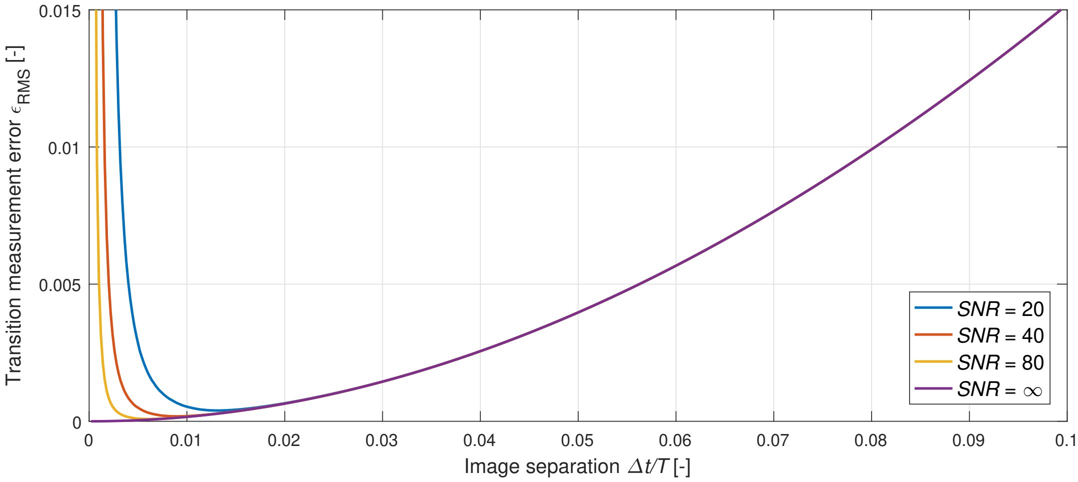

Figure 5.3: Effect of the image separation time step on the transition measurement error ϵ_{RMS} for three different SNR for the quasi-steady DIT model with $\alpha_1 = 4°$

The optimization of $\Delta t/T$ in the quasi-steady DIT model with noise can be performed by detecting the $\Delta t/T$ with the minimum value of ϵ_{RMS} for each SNR and each α_1. The result is the optimized image separation $\Delta t/T$, shown in Fig. 5.4a for the eight pitching motion amplitudes and the considered range of SNR. Notably, as for the results from the more complex optimization of $\Delta t/T$ for the experimental DIT results in Ch. 4, $\Delta t/T \approx 0.01$ for a large part of the relevant SNR region. The value of the error ϵ_{RMS} shown in Fig. 5.4b corresponds to the optimized $\Delta t/T$ from Fig. 5.4a.

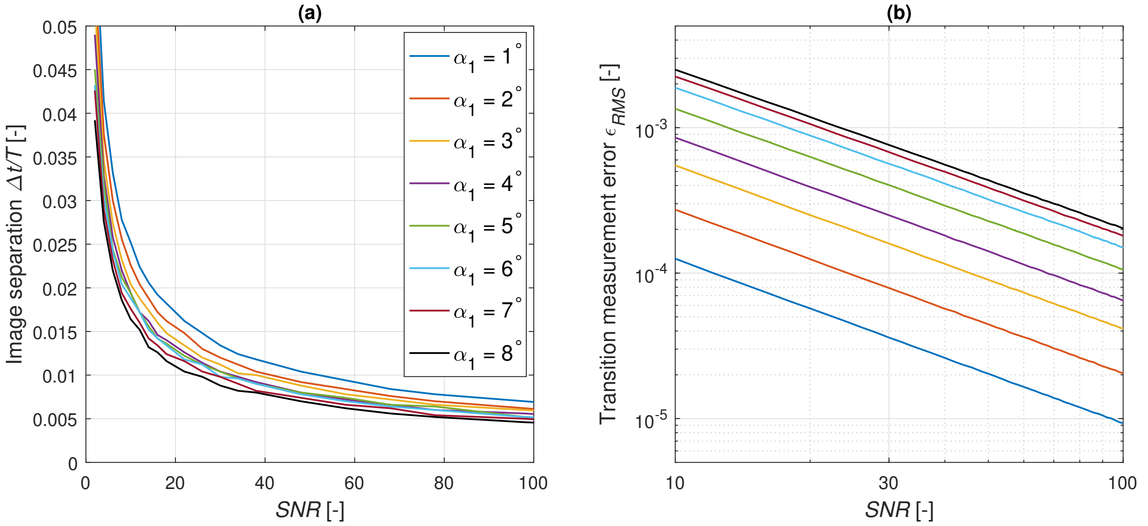

Figure 5.4: (a): Optimization of the image separation time step in the quasi-steady DIT model for various SNR and all α_1, (b): Corresponding value of the quasi-steady transition measurement error ϵ_{RMS}

5.1.2. Unsteady DIT simulation

In the following, DIT is applied to the results from the unsteady heat transfer simulation. To remove outliers from the DIT transition measurement, all DIT data points where $x_{tr}/c > 0.6$ are removed in post-processing. Remaining outliers in the DIT result are removed with a median filter of window size 5. The results for the DIT transition measurement and the DIT signal $\Delta T'$ are shown for three different $\Delta t/T$ in Fig. 5.5. The transition location from the C_f-analysis is shown for reference.

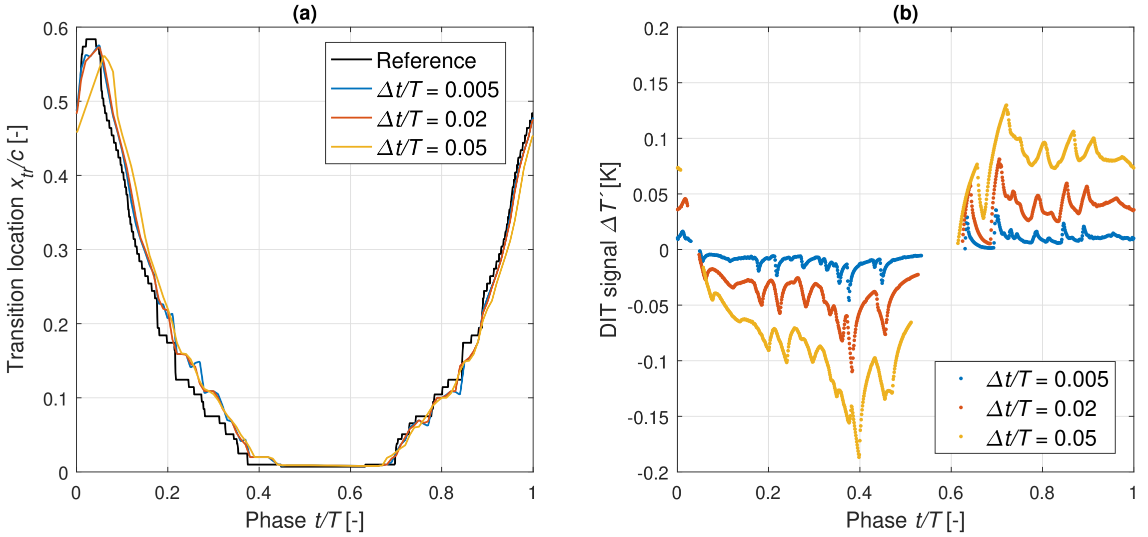

Figure 5.5: Effects of varying $\Delta t/T$ when performing DIT on the simulation data:
(a) effect on the DIT transition location, (b) effect on the DIT signal

The DIT signal in Fig. 5.5b shows the qualitative behavior that is expected from the analysis of the DIT model. However, the DIT signal $\Delta T'$ is affected by the “stepping” motion of the transition location over time and exhibits unphysical spikes. The non-smooth transition movement also produces some scatter in the DIT transition measurements in Fig. 5.5a, in particular for the smaller $\Delta t/T$. A part of the motion period cannot be measured with DIT because the regions with forward and backward moving transition were separated. These missing x_{tr}/c-values are linearly interpolated. Additionally, Fig. 5.5a shows the source of error for DIT transition measurements that was not captured by the quasi-steady DIT model; the phase lag. It can be seen in Fig. 5.5a that the phase lag increases with increasing $\Delta t/T$, as discussed for this data in Sec. 2.2.3 and shown for experimental DIT in Sec. 4.3.

The calculated ϵ_{RMS} over $\Delta t/T$ is shown in Fig. 5.6a. The total error can be split into two components, the phase lag error $\epsilon_{\Delta T}$ and the amplitude measurement error $\epsilon_{RMS,amp}$. The phase lag is determined with a cross-correlation of the DIT transition measurement and the reference transition. The number of samples corresponding to the cross-correlation peak is converted into the time lag in periods and plotted in Fig. 5.6b. The amplitude error $\epsilon_{RMS,amp}$ plotted in Fig. 5.6c is calculated after the phase lag error is corrected by shifting the DIT transition in phase by $\epsilon_{\Delta T}$ and then using Eq. 5.2.

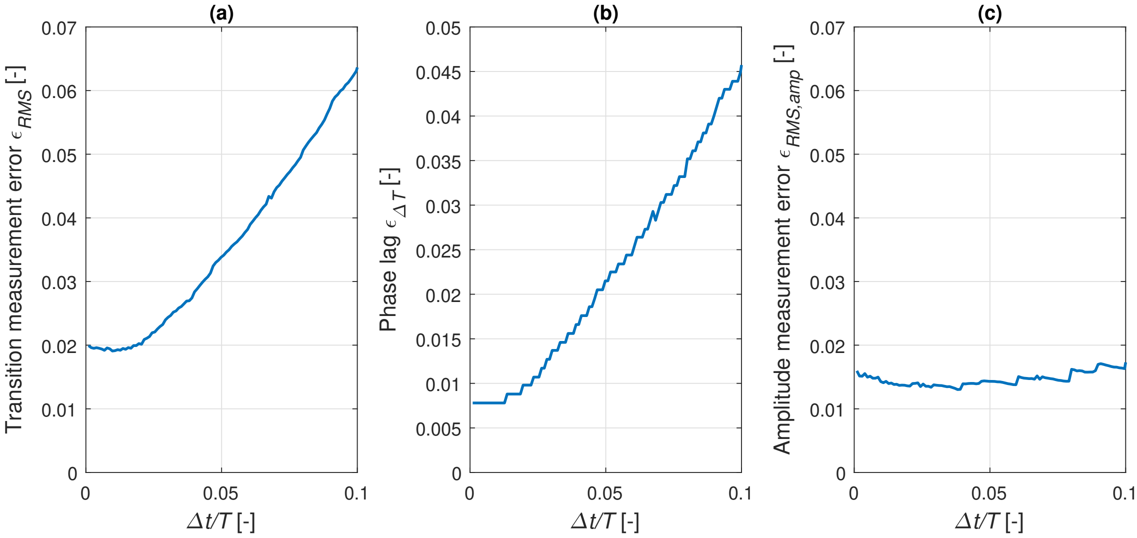

Figure 5.6: DIT transition measurement error over image separation time step for simulation data: (a) total measurement error, (b) phase lag, (c) amplitude measurement error

The total error ϵ_{RMS} in Fig. 5.6a decreases nearly linearly with decreasing time step from $\Delta t/T = 0.1$ until $\Delta t/T \approx 0.02$. Between $0 < \Delta t/T < 0.02$ the total error is approximately constant. When considering the individual error contributions, it can be seen in Fig. 5.6c that the value of $\epsilon_{RMS,amp}$ is not changing more than ± 0.003 with the variation of $\Delta t/T$. Confirming the findings from Gardner et al. [20], the phase lag error in Fig. 5.6b decreases with decreasing $\Delta t/T$. For the smallest $\Delta t/T < 0.01$, this effect diminishes and a phase lag error of $\epsilon_{\Delta t/T} \approx 0.008$ remains. The concluding observation of this error analysis is that using the smallest $\Delta t/T < 0.01$ reduces the phase lag well below 1% of the period, such that the amplitude measurement error remains as the major contribution to the total error.

Figure 5.7 shows the effects of varying $\Delta t/T$ on the DIT results from the simulation data, with added randomly distributed artificial noise at a level corresponding to $SNR = 30$. The DIT results with artificial noise are additionally filtered by rejecting the data points with the smallest values for the DIT signal using a threshold, i.e. $\Delta T' < t_n = n \cdot 10$ for each respective noise level n.

Figure 5.8a shows the total error ϵ_{RMS} over $\Delta t/T$ for three example SNR. The case without artificial noise is shown for reference. For these error plots, only DIT transition measurement results are included where at least 20% of the data points over the period were above the noise threshold t_n. This produces missing values for ϵ_{RMS} for the smallest $\Delta t/T$ because of the respectively smaller $\Delta T'$. The graph in Fig. 5.8a is in good qualitative agreement with the error behavior for the quasi-steady DIT model in Fig. 5.3. The steep rise-behavior for small $\Delta t/T \rightarrow 0$ at $SNR \neq \infty$ from the model is not always included in Fig. 5.8a, due to the rejection of results with too few valid data points. The optimized image separation time step $\Delta t/T$, corresponding to the minimum of ϵ_{RMS} for each SNR, is plotted in Fig. 5.8b. The optimized $\Delta t/T$ for the simulation data with various noise levels is typically around $\Delta t/T \approx 0.01$, similar to that for the quasi-steady DIT model and for the optimization of $\Delta t/T$ in the analysis of the experimental data. Notably, this value is also reached without artificial noise, i.e. $SNR = \infty$. The optimized $\Delta t/T$ is much larger only for $SNR < 10$. As a further contribution to the error analysis of the DIT transition measurements for the simulation data with added artificial noise, Fig. 5.9 shows the total error and the individual contributions of the DIT transition measurement with the optimized $\Delta t/T$ for each SNR.

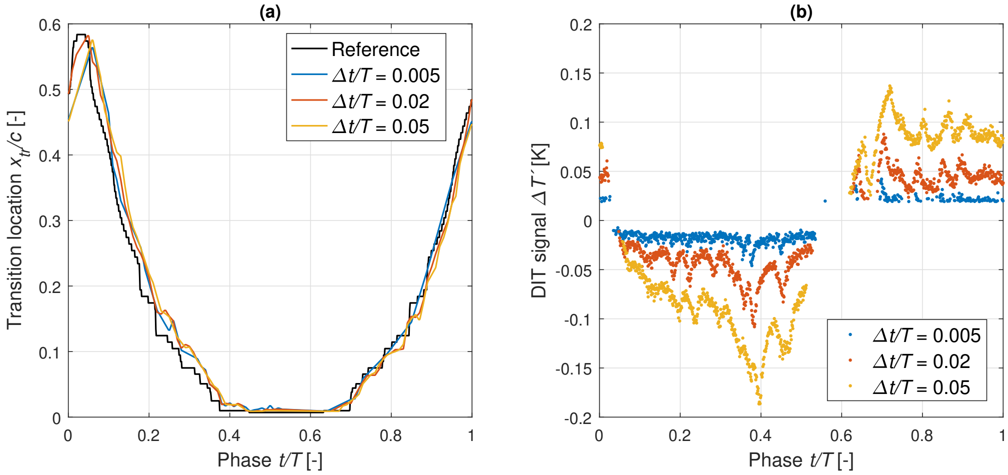

Figure 5.7: Effects of varying $\Delta t/T$ when performing DIT on the simulation data with artificial noise at $SNR = 30$: (a) effect on the DIT transition location, (b) effect on the DIT signal

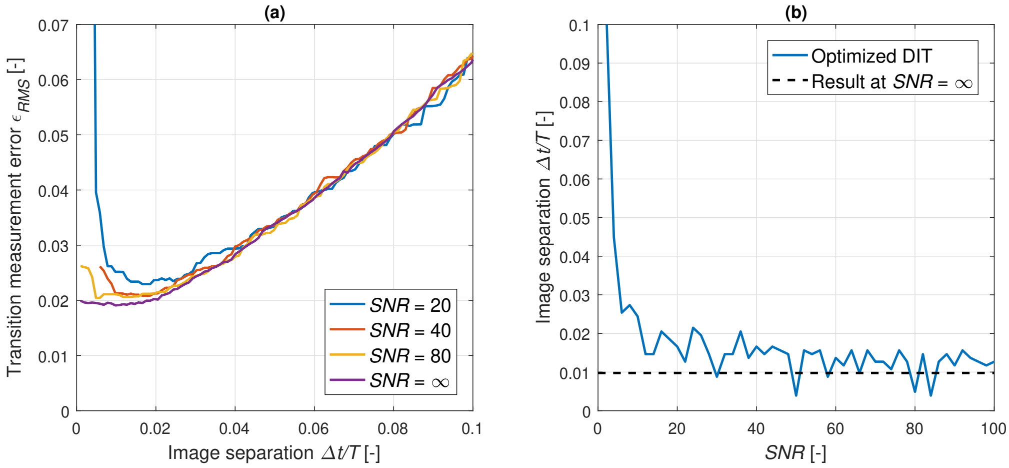

Figure 5.8: (a): DIT transition measurement error over $\Delta t/T$ for various SNR for the simulation data, (b): Optimized DIT image separation time steps over SNR for the simulation data

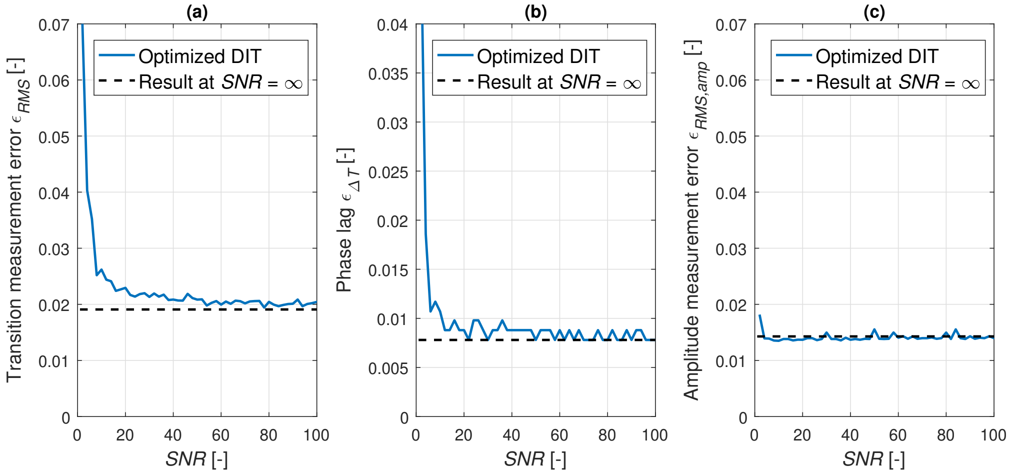

Figure 5.9: DIT transition measurement error over SNR with optimized $\Delta t/T$ for simulation data: (a) total measurement error, (b) phase lag, (c) amplitude measurement error

The amplitude measurement error $\epsilon_{RMS,amp}$ shown in Fig. 5.9c is nearly independent of the SNR and at the same level as for $SNR = \infty$ when $\Delta t/T$ is optimized for the total error ϵ_{RMS}. The phase lag error $\epsilon_{\Delta T}$ in Fig. 5.9b appears to be directly related to the size of the optimized $\Delta t/T$ as seen in Fig. 5.8b, which is expected when considering the nearly linear relation seen in Fig. 5.6b. This means that the phase lag error $\epsilon_{\Delta T}$ is approximately constant at the same level as for $SNR = \infty$ when $SNR > 20$. The total error ϵ_{RMS} shown in Fig. 5.9a behaves similar to the phase lag error $\epsilon_{\Delta T}$, which is expected according to the nearly constant $\epsilon_{RMS,amp}$. Because of this error behavior with respect to SNR, transition measurement results for the simulation data with added artificial noise will be limited to a few example SNR-cases for the rest of this chapter.

5.2. Development of adaptive DIT

Adaptive differential infrared thermography (ADIT) is an alternative approach to DIT, but it is essentially based on the same transition measurement principle, i.e. subtracting two similar thermographic measurements and extracting the transition location as location of the maximum difference between the two. The modification of ADIT is that the image separation time step is automatically selected according to a specified criterion for the measured DIT signal at a given data point. The idea is that the ADIT approach provides a transition measurement with a smaller measurement error compared to conventional DIT, particularly for thermographic measurements with varying signal strength, and that it detects the transition movement nearer to the upstream and downstream turning points.

The criterion for the automated selection of $\Delta t/T$ in the quasi-steady DIT model is based on the DIT signal ΔI in relation to the given noise threshold level t_n. The working principle of ADIT is illustrated by the example shown in Fig. 5.10. In Fig. 5.10a, the modeled DIT signal ΔI for a fixed first phase instant at $t/T = 0.25$ in the case with pitching motion amplitude $\alpha_1 = 4°$ is shown. The ΔI depends on the image separation time step $\Delta t/T$ following Eq. 5.1. The noise threshold t_n corresponding to $SNR = 30$ is indicated in Fig. 5.10a as well. If $\Delta t/T$ is too small, ΔI is below the threshold t_n and the model returns no DIT transition measurement result. The ADIT approach automatically selects the first $\Delta t/T$ for each phase instant t/T_a that produces a sufficient DIT signal $\Delta I > t_n$. Thus, the DIT transition measurement error is reduced as far as possible within the limits of the available signal. Figure 5.10b shows the reference quasi-steady transition and the DIT model transition measurement corresponding to Fig. 5.10a. The principle of ADIT can be extended to all individual phase instants over the period T, meaning that for each phase instant t/T the $\Delta t/T$ is automatically selected to find the first following phase instant that produces a sufficiently large DIT signal $\Delta I > t_n$. Results for the adapted $\Delta t/T$ and the ADIT transition measurement results are shown four example pitching motion cases at a noise level corresponding to $SNR = 30$ in Figs. 5.11a and 5.11b.

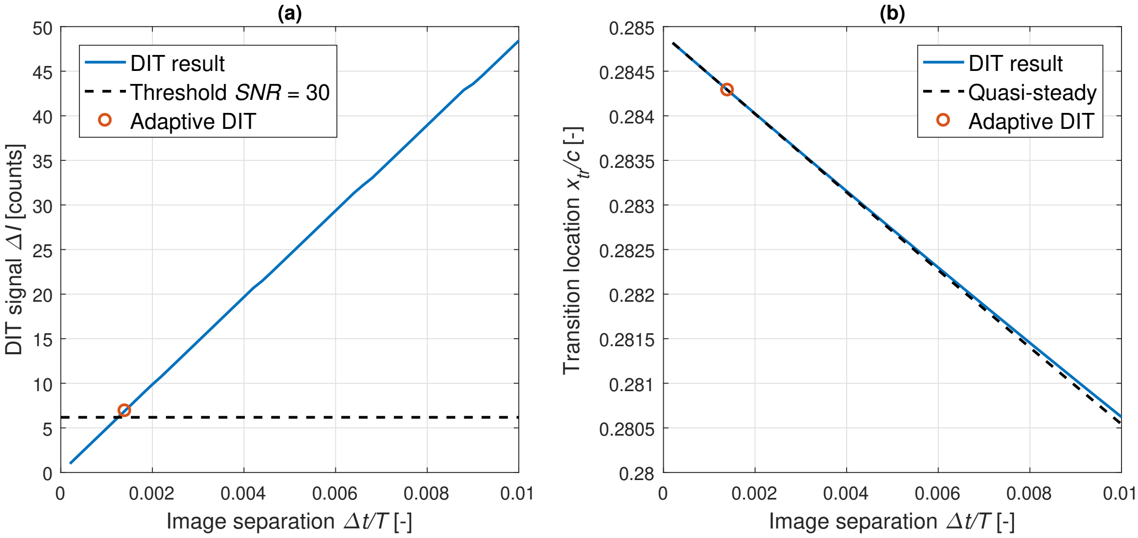

Figure 5.10: Working principle of ADIT (red circle) for the quasi-steady DIT model with $\alpha_1 = 6°$ at $t/T = 0.25$: (a) DIT model signal over $\Delta t/T$, (b) DIT model transition measurement and quasi-steady reference

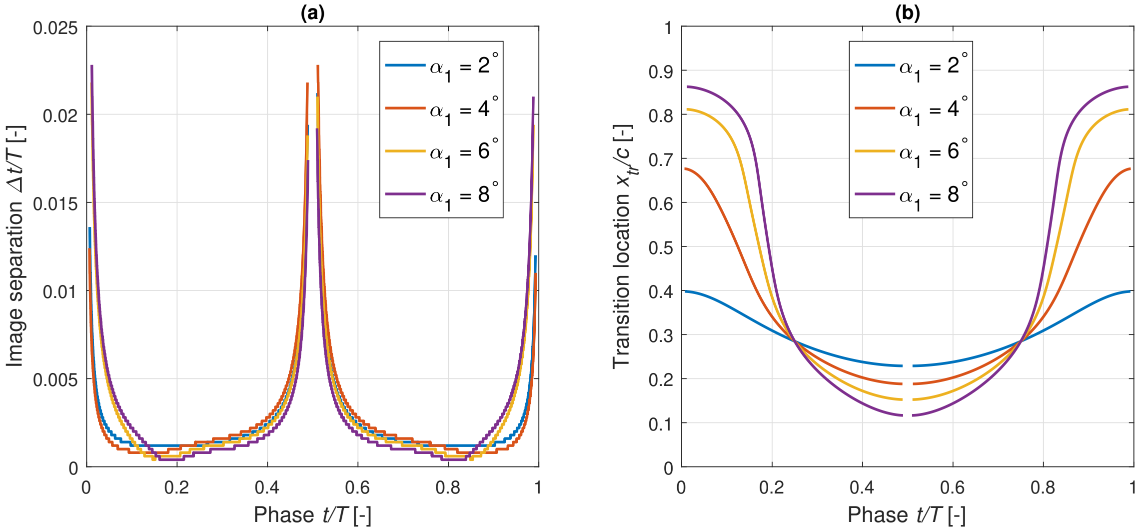

Figure 5.11: Application of ADIT to the quasi-steady DIT model with various α_1 at $SNR = 30$: (a) Automatically selected $\Delta t/T$ over phase, (b) ADIT transition measurement result

The automatically selected, adapted time step size $\Delta t/T$ over phase is shown in Fig. 5.11a. The behavior of $\Delta t/T$ reveals that the ADIT approach results in a better detection of the transition location at the parts of the motion period where the transition movement slows down and therefore ΔI decreases following Eq. 5.1. It can be observed in Fig. 5.11b that ADIT works identically to DIT within each DIT window. The missing segments in the plots at $t/T = 0$ and $t/T = 0.5$ result from the separation of the up- and downstroke for the application of DIT that was also implemented for ADIT. The effect of this separation is that the ADIT algorithm cannot find a suitable $\Delta t/T$ for the data points in this region.

In the next step, the ADIT approach is applied to the eight pitching motion cases of the quasi-steady DIT model and for all SNR that have been used during the optimization of $\Delta t/T$ with the conventional approach to DIT in Sec. 5.1.1. The transition measurement error for ADIT is calculated with Eq. 5.2 using the quasi-steady transition location as reference, missing transition measurement values are linearly interpolated from the neighboring measurements. In Fig. 5.12, the transition measurement error ϵ_{RMS} from ADIT is plotted for the eight α_1 with solid lines and the reference error over SNR from the optimization of conventional DIT as seen in Fig. 5.4 is plotted with dashed lines.

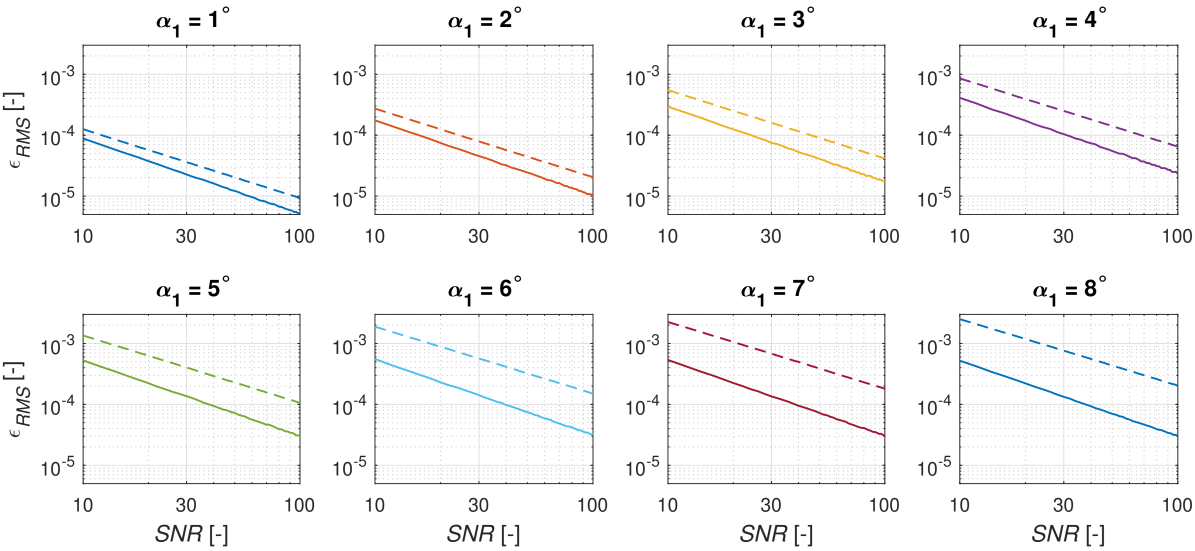

Figure 5.12: Transition measurement error with ADIT (solid) compared to optimized DIT (dashed) for the quasi-steady model

It is shown in Fig. 5.12 that the transition measurement error with ADIT is smaller than the error obtained from the application of optimized DIT for all motion amplitudes α_1 and all considered SNR. The ADIT approach has an increasing effect on the error reduction for increasing pitching motion amplitudes. The pitching motion with $\alpha_1 = 8°$ exhibits both the fastest and the slowest moving transition location over the period of all considered amplitudes α_1. This promotes the application of the ADIT approach, because the time step size $\Delta t/T$ can be adjusted to both extremes, while the optimized constant $\Delta t/T$ is a compromise. For the smallest pitch amplitudes, the transition movement over the period is closer to a sinusoidal motion and the adaptive approach has a smaller effect on the error reduction. The value for the measurement error for small α_1 cases is an order of magnitude smaller than for the $\alpha_1 = 8°$ case, since the major source of error for the quasi-steady DIT model with noise cutoff t_n is the slowly moving transition near the turning points.

The application of ADIT to the simulation data is performed similarly to the application of conventional DIT, and the same processing steps are performed. The difference of ADIT to the conventional DIT implementation is that instead of applying the threshold for the DIT signal of $t_N = n \cdot 10$ in the post-processing to filter the DIT transition measurement results, this same threshold t_n is used in the ADIT approach to select the appropriate DIT time step automatically. In Fig. 5.13a, the functioning of the the ADIT approach is demonstrated for a noise level corresponding to $SNR = 30$. The automatically selected $\Delta t/T$ over the period are plotted as dots, the optimized constant $\Delta t/T$ for this SNR is plotted for reference. In Fig. 5.13b, the DIT transition measurement results for $SNR = 30$ from optimized constant time step DIT and from ADIT are shown in comparison. The transition location from the analysis of C_f is shown as a reference.

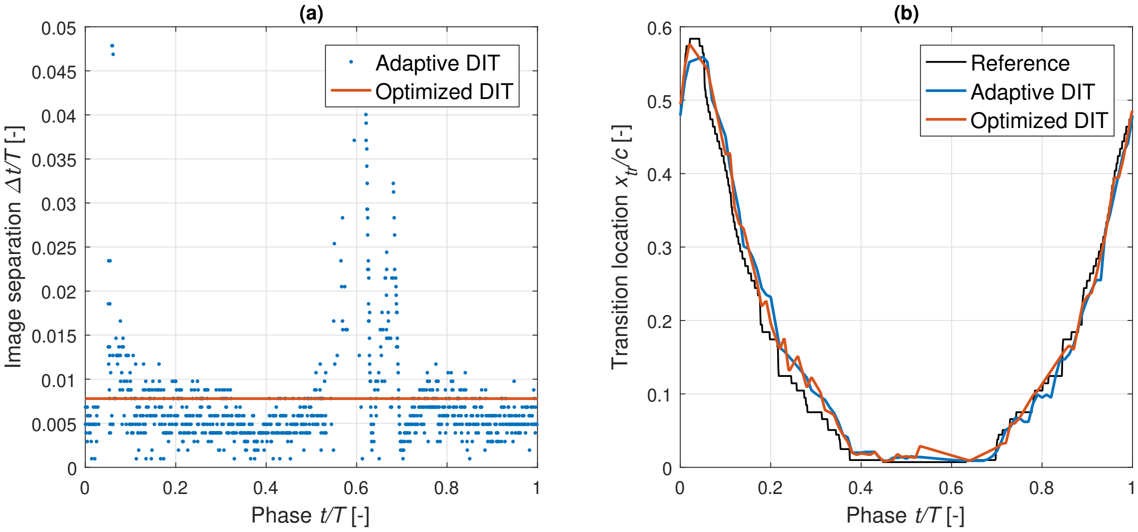

Figure 5.13: Application of ADIT to the simulation results with artificial noise $SNR = 30$: (a) Adapted $\Delta t/T$ compared to the optimized constant $\Delta t/T$, (b) Comparison of the transition measurements with ADIT and optimized DIT

Figure 5.13a shows that ADIT works as designed on the simulation data for the selected noise level. For most of the period, the $\Delta t/T$ from ADIT is smaller than the optimized constant $\Delta t/T$. For the parts of the period with slow or zero transition movement, the adapted $\Delta t/T$ increases. The results from the DIT and ADIT transition measurement in Fig. 5.13b are both flawed by seemingly random scatter during different parts of the period, so that systematic differences between the two approaches can only be searched reliably in the region $0.3 < x/c < 0.5$, and no distinct systematic differences are identified there. Hence, the only observation that can be made from Fig. 5.13b is that the transition measurements from the two different approaches are essentially identical.

The total error ϵ_{RMS} of the ADIT transition measurement is compared to the error ϵ_{RMS} over $\Delta t/T$ from constant time step DIT for the three example SNR of Fig. 5.8. The comparison is shown in Fig. 5.14, in this graph the ADIT error does not vary for a fixed SNR, the constant values are plotted with dashed lines in the color matching the respective SNR. The constant value of ϵ_{RMS} for ADIT is nearly at the same level at the minimum error of conventional DIT, with a maximum difference of $\Delta\epsilon_{RMS} < 0.005$.

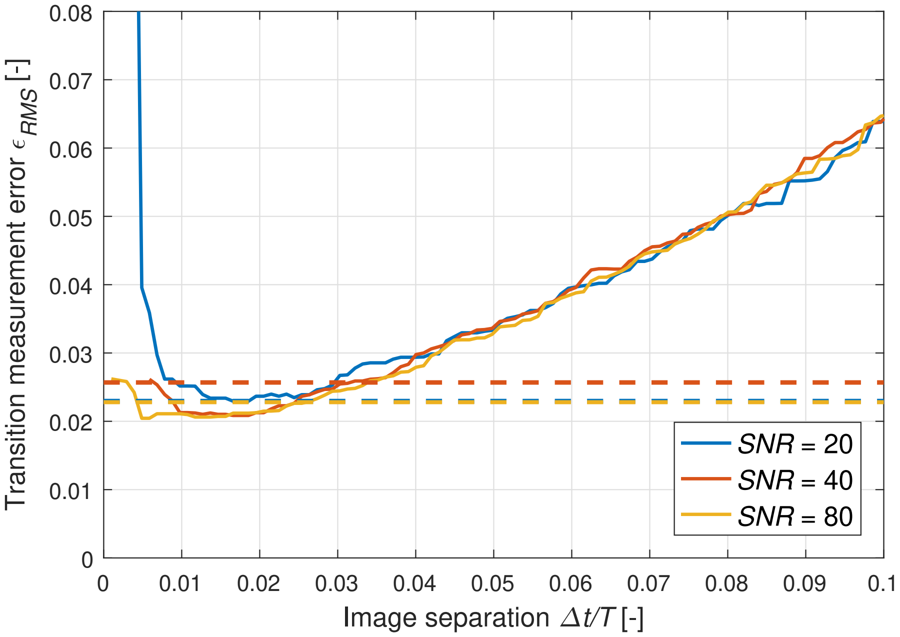

Figure 5.14: Comparison of the total transition measurement error for DIT over varying $\Delta t/T$ (solid lines) and for ADIT (dashed lines) at three example SNR

5.3. Development of local infrared thermography

Local infrared thermography (LIT) is the idea of analyzing the surface temperature signal over time at fixed locations on the surface. This measurement principle is similar to the fast-response transition measurement techniques HFA and σC_p and in contrast to DIT, that analyzes global changes in the surface temperature signal. The required information for the application of LIT to the simulation data is readily available as temperature T' from the top node of the thermal FEM computation. The analysis of the example location $x/c = 0.3$ is shown in Fig. 5.15 and explained in the following.

The skin friction coefficient C_f over phase from the simulation is shown in Fig. 5.15a. The corresponding temporal finite-difference gradient of C_f is shown in Fig. 5.15b. From the results shown in Fig. 3.10 of Sec. 3.3, the phase instants where the transition onset, mean and end pass through the shown location $x/c = 0.3$ are known and indicated in the graphs as well. Figure 5.15c shows the temperature over phase, the finite-difference temperature gradient with respect to the phase $\partial T'/\partial(t/T)$ is shown in Fig. 5.15d. In the latter two graphs, the extrema of the two curves are marked in addition to the indication of the phase instants at which the C_f-transition passes through the observed location.

In the center of the motion period $(0.13 < t/T < 0.93)$ the shown location $x/c = 0.3$ experiences turbulent flow, in the beginning and end of the period the flow there is laminar. It can be observed in Fig. 5.15a that the occurrence of boundary layer transition is the most distinct feature of the $C_f(t/T)$ curve, it is accompanied by a steep rise in C_f during the transition to turbulence and the corresponding steep drop during relaminarization. The dominance of this feature on $C_f(t/T)$ is reflected in the local skin friction gradient of Fig. 5.15b. The occurrence of boundary layer transition produces a positive and a negative peak and the global extrema of $\partial C_f/\partial(t/T)$ agree with the phase instants of transition to turbulence and relaminarization, i.e. $(\partial C_f/\partial x)_{max}$. The finite-difference gradient of the skin friction coefficient also reveals that the way the coupled CFD/FEM simulation has been set up has some detrimental effects on the plausibility of the produced results for C_f. Several spikes appear in the $\partial C_f/\partial(t/T)$ signal that are associated with the propagation of the transition front.

The temperature curve of Fig. 5.15c is increasing when the boundary layer flow is laminar and decreasing when the boundary layer flow is turbulent. The peaks of the temperature curve are therefore intuitively connected to the occurrence of boundary layer transition to turbulence or relaminarization. The analysis of the temperature signal at $x/c = 0.3$ reveals that the transition from laminar to turbulent flow forms a more distinct peak in the temperature T' compared to the relaminarization. When comparing the phase instants of the extrema of T' to the transition phase instants, it can seen that the maximum is very close to the $(\partial C_f/\partial x)_{max}$ transition instant, while the minimum leads the $(\partial C_f/\partial x)_{max}$ transition instant in phase and is in a better agreement with the transition end determined from C_f. Even though the exact relation between the $C_f(t/T)$ and the $T'(t/T)$ curves is non-trivial, it can be identified in Fig. 5.15c that the change of the skin friction over time is the cause for the varying T' signal. This relation is then overlayed with the temperature response of the material. This overlay is the reason why the $T'(t/T)$-curve is not nearly symmetric around $t/T = 0.5$, like it is observed in the aerodynamics in terms of $C_f(t/T)$.

The local temperature gradient $\partial T'/\partial(t/T)$ seen in Fig. 5.15d forms two distinct peaks with a steep rising edge and a smooth decay. It is observed that both peaks are correlated to the phase instants of $(\partial C_f/\partial x)_{max}$. The local transition to turbulence produces a smaller absolute value for the negative peak that slightly lags the $(\partial C_f/\partial x)_{max}$ transition instant, whereas the local relaminarization produces a maximum value that correlates very well with the $(\partial C_f/\partial x)_{max}$ transition phase instant. The most notable effect of the thermal inertia on the temperature gradient is that the distinct peaks of $\partial C_f/\partial(t/T)$ are spread over a larger part of the period for $\partial T'/\partial(t/T)$.

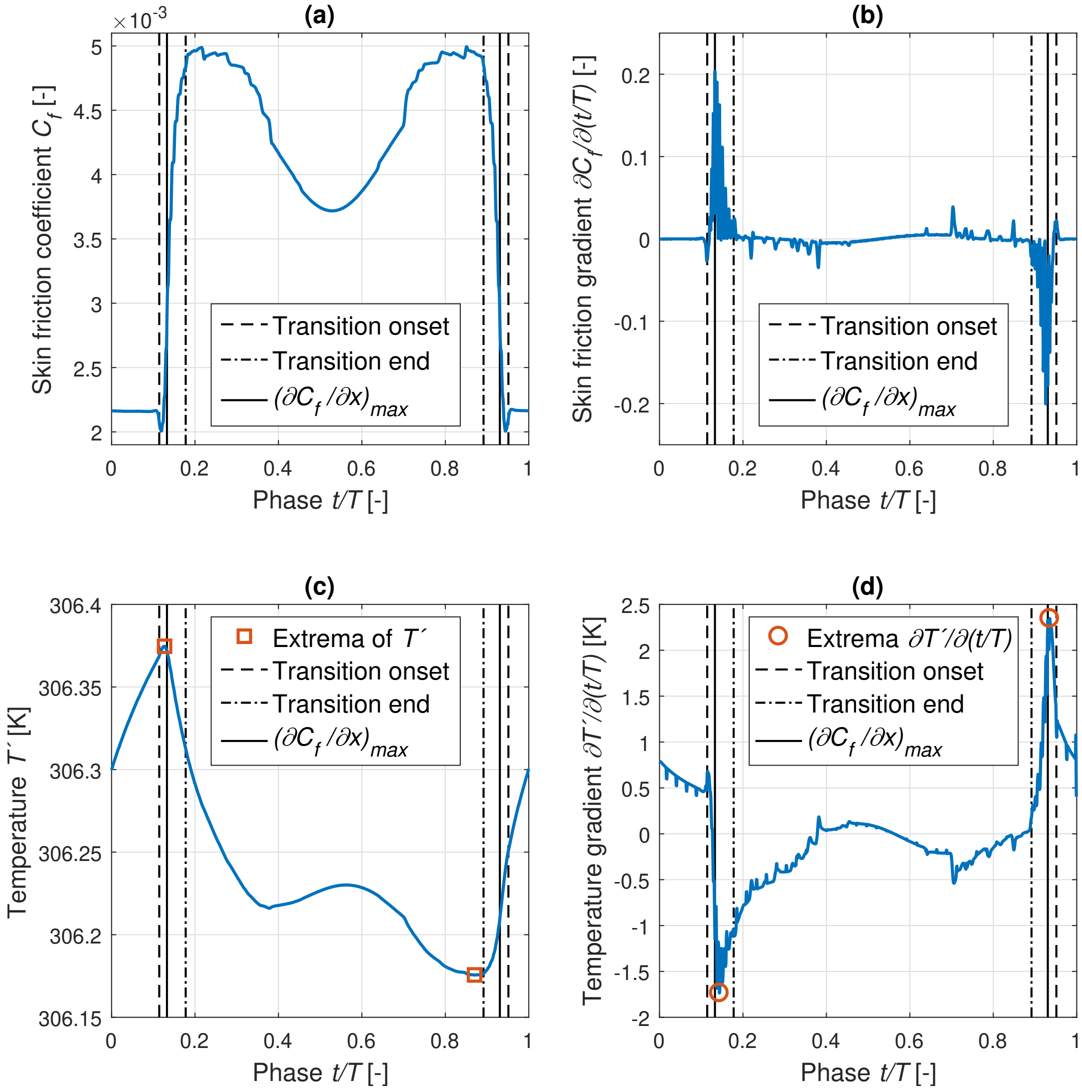

Figure 5.15: Principle of local infrared thermography for the simulation data at $x/c = 0.3$:
(a) local skin friction, (b) local skin friction gradient, (c) local temperature, (d) local temperature gradient

The reference transition for the simulation data and the phase instants of the extrema of T' and $\partial T'/\partial(t/T)$ are compared in Fig. 5.16a and Fig. 5.16b respectively, for all discrete locations from the simulation data until $x/c = 0.7$. The investigation of the local temperature signal at discrete locations produces values that correlate well with the reference transition location, when the extrema of T' and of $\partial T'/\partial(t/T)$ are considered for all chord locations that experience boundary layer transition. The agreement of the gradient extrema with the reference transition is very good during the upstroke and the downstroke. The agreement of the extrema of T' with the reference transition is very good during the upstroke and fair during the downstroke. Some outliers are produced near the motion turning points.

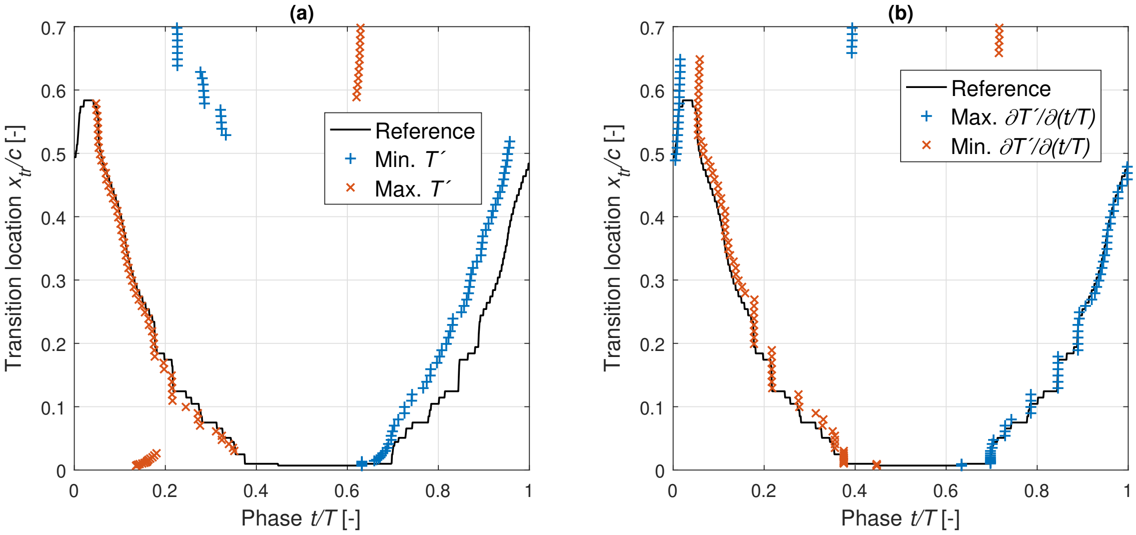

Figure 5.16: (a): Extrema of the local temperature, (b): Extrema of the local temperature gradient, in comparison to the reference transition from the simulation data

6

Comparison and validation of the transition measurement schemes

In this chapter, the transition measurement results from ADIT and LIT for the experimental data are compared to the optimized DIT results. Afterwards, the transition measurement results based on infrared thermography are compared to reference transition measurements from the σC_p-technique.

6.1. Comparison of the alternative schemes with optimized DIT

6.1.1. Adaptive DIT compared to optimized DIT

The general working principle of ADIT on the experimental data is demonstrated in this subsection for the example motion case with $\alpha_1 = 6°$ and $k = 0.038$. The noise threshold for the DIT signal t_n that is used to select the appropriate $\Delta t/T$ in the ADIT approach is specified differently than as it was introduced in Ch. 5. In the application of ADIT to the experimental data, t_n is adapted for each time step $\Delta t/T$ to be $t_n(\Delta t/T) = \Delta I_{noise}(\Delta t/T) + 5$, where $\Delta I_{noise}(\Delta t/T)$ is the minimum DIT signal that is found over the entire period T for the respective $\Delta t/T$. As an additional constraint, the maximum allowed image separation time step is $\Delta t/T = 0.1$. The implementation of ADIT for the example motion case is illustrated in Fig. 6.1. The working principle of ADIT is demonstrated by the adapted $\Delta t/T$ shown in Fig. 6.1a in comparison to the optimized constant $\Delta t/T$. The functioning of the ADIT approach is illustrated in Fig. 6.1b, where the values of P_{max} for each bin in the post-processing procedure of the ADIT and optimized DIT data points are shown for the considered example case.

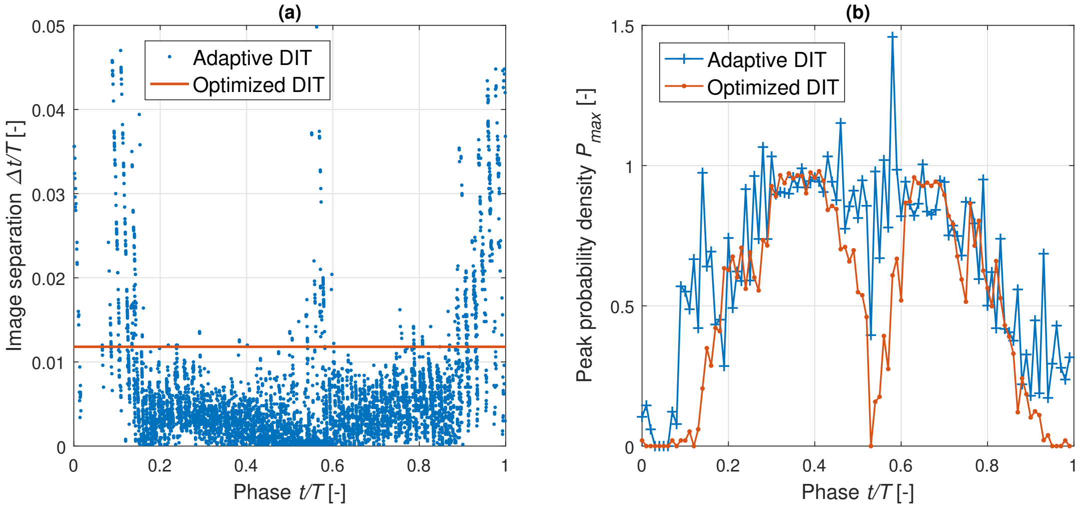

Figure 6.1: Application of ADIT to the experimental test case with $\alpha_1 = 6°$ and $k = 0.038$: (a) Adapted $\Delta t/T$ compared to the optimized constant $\Delta t/T$, (b) Peak probability density P_{max} per bin with ADIT and optimized DIT

The comparison of the automatically selected $\Delta t/T$ with the optimized constant $\Delta t/T$ for the experimental example case shown in Fig. 6.1a is similar to the same comparison for the simulation data in Fig. 5.13a. For the largest part of the period, the adapted time step is smaller than the optimized constant $\Delta t/T$. When the transition movement slows down near the motion turning points, the DIT signal strength ΔI decreases and the adapted time step $\Delta t/T$ increases accordingly. This effect is observed to a larger extent for the downstream transition motion turning point around $t/T = 0$. In Fig. 6.1b, it can be deduced from the $P_{max}(t/T)$ that the ADIT method produces more valid transition measurement data points over the period, i.e. more data points that are not filtered with the post-processing algorithm. Several ADIT data points accumulate when the transition movement speed is changing and $\Delta t/T$ is adapted accordingly, causing an increase of $P_{max} > 1$ there.

The effect that the ADIT measurement scheme produces on the filtered transition measurement results is illustrated in Fig. 6.2. This graph shows the result for the example motion case $\alpha_1 = 6°$ and $k = 0.038$, obtained from the ADIT methodology with the identical post-processing procedure as for optimized DIT. For reference, the quasi-steady transition for the motion case $\alpha_1 = 6°$ is shown as well. In Fig. 6.2, the transition measurement results from ADIT and optimized are found to be essentially identical for $0.15 < t/T < 0.9$. Only small differences can be registered in the region $0.8 < t/T < 0.85$. As distinctive difference between the two transition measurements, ADIT is able to reproduce the transition motion around the downstream turning point, while optimized DIT is not. Considering the behavior of the quasi-steady transition at the downstream turning point, the transition measurement results from ADIT in this region appear correct.

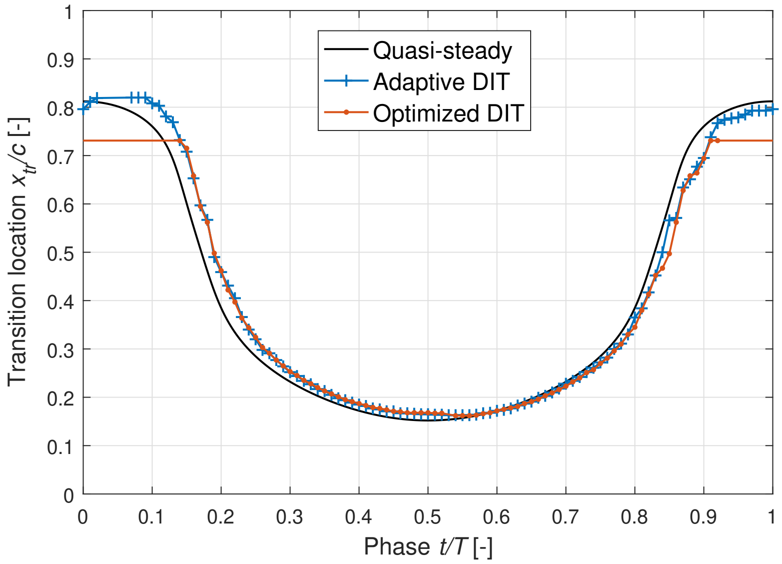

Figure 6.2: Transition measurement result from ADIT for $\alpha_1 = 6°$ and $k = 0.038$, compared to the optimized DIT transition measurement and the quasi-steady transition

The application of ADIT to the example motion case shows that ADIT measures transition over a larger part of the motion period than optimized DIT. The measurement accuracy is equivalent to optimized DIT transition measurements in the part of the period where both techniques produce results. It is concluded from the comparison of ADIT and optimized DIT that the ADIT approach produces superior transition measurement results compared to optimized DIT. This conclusion can be extended to all pitching motion test cases in the test matrix. The frequency and amplitude effects on the transition measurements with ADIT are shown in Fig. 6.3. In Sec. 6.2, the results from ADIT are compared to reference transition measurements from the σC_p technique.

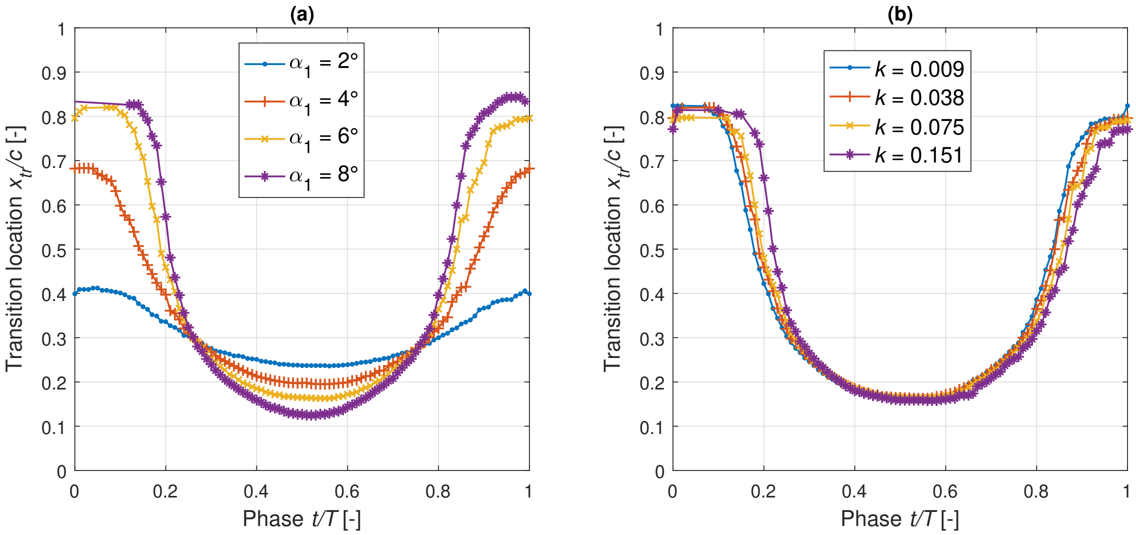

Figure 6.3: (a): Amplitude effects at $k = 0.038$ and (b): Frequency effects at α_1 = 6° on the unsteady boundary layer transition measured with ADIT

6.1.2. Local infrared thermography compared to optimized DIT

Local infrared thermography as introduced in Sec. 5.3 is based on evaluating the surface temperature signal at a fixed location x/c on the model surface. For the application of LIT to the experimental data, the radiation intensity I data is analyzed instead of the temperature T'. The same pre-processed data from the optimization of DIT is used for the implementation of the LIT approach, with an additional processing step. The data processing procedure is described for the example location $x/c = 0.31$ in the motion case with $\alpha_1 = 6°$ and $k = 0.075$ and illustrated in Fig. 6.4. In the original data processing scheme described in Ch. 3, the temperature drift corrected radiation intensity signal over time $I(t)$ at $x/c = 0.31$ (shown in Fig. 6.4a) is ordered in phase with the simultaneously measured $\alpha(t)$ (see Fig. 6.4b). Because this ordered signal is too noisy for a meaningful computation of the finite-difference gradient, a moving-average smoothing (window size $\pm 1\%$ of the period T) is performed, resulting in the intensity signal shown in Fig. 6.4c. Then, the finite-difference intensity gradient $\partial I/\partial(t/T)$ can be computed, see Fig. 6.4d. For the location presented in Fig. 6.4, the boundary layer flow in the center of the phase $0.24 < t/T < 0.78$ is turbulent, and at the beginning and end of the phase at $x/c = 0.31$ the flow is laminar (consider Fig. 3.8). The intensity signal in Fig. 6.4c is increasing when the experienced flow is laminar and decreasing when turbulent, as seen in Sec. 5.3 for the simulation data. The analysis of the intensity gradient shown in Fig. 6.4d reveals two distinct peaks at the phase instants of local transition to turbulence and local relaminarization. These observations are in good agreement with the findings from the analysis of the temperature signal of the simulation data seen in Fig. 5.15.

The LIT approach to measuring unsteady boundary layer transition is implemented for the example motion case with $\alpha_1 = 6°$ and $k = 0.075$. The peak detection of I and $\partial I/\partial(t/T)$ is applied to all 561 sampled chord locations, corresponding to the spanwise averaged pixel location in the infrared camera measurements. The processing procedure of the detected peaks to a transition measurement result follows three steps. First, the analysis of the detected peaks is restricted to the region where transition occurs. Secondly, the transition locations x_{tr}/c are extracted for each point in phase t/T, when multiple transition locations are associated to the same t/T the median x_{tr}/c is used. As last step, the resulting transition movement over the period is median filtered to remove outliers. This methodology is applied to the intensity gradient $\partial I/\partial(t/T)$ in Fig. 6.5. The transition measurement with optimized DIT is shown for comparison. The parts of the period where no x_{tr}/c was measured are not linearly interpolated in this graph. There is no qualitative difference between the results from the intensity gradient peak analysis and DIT. The only difference is that the DIT measurement appears smoother, which can be accredited to the more elaborate post-processing algorithm for optimized DIT (consider Sec. 4.2). Based on the analysis of the simulation results and on Fig. 6.5, it is concluded that performing DIT with a small image separation time step $\Delta t/T$ and detecting the peaks of the intensity gradient are equivalent operations that produce very similar transition measurement results.

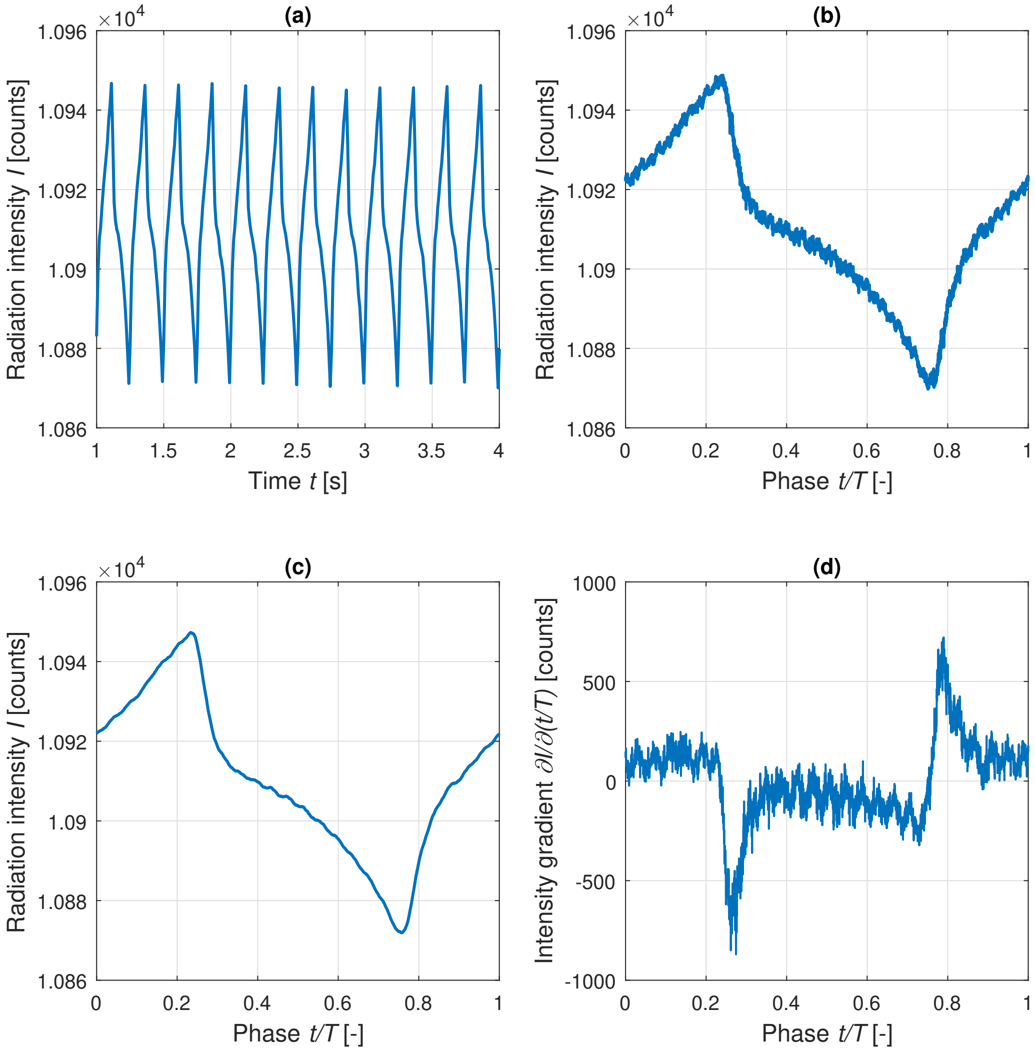

Figure 6.4: Application of LIT to experimental data from the case $\alpha_1 = 6°$ and $k = 0.075$: (a) processed intensity signal over time, (b) signal ordered in phase, (c) smoothed intensity signal, (d) intensity gradient

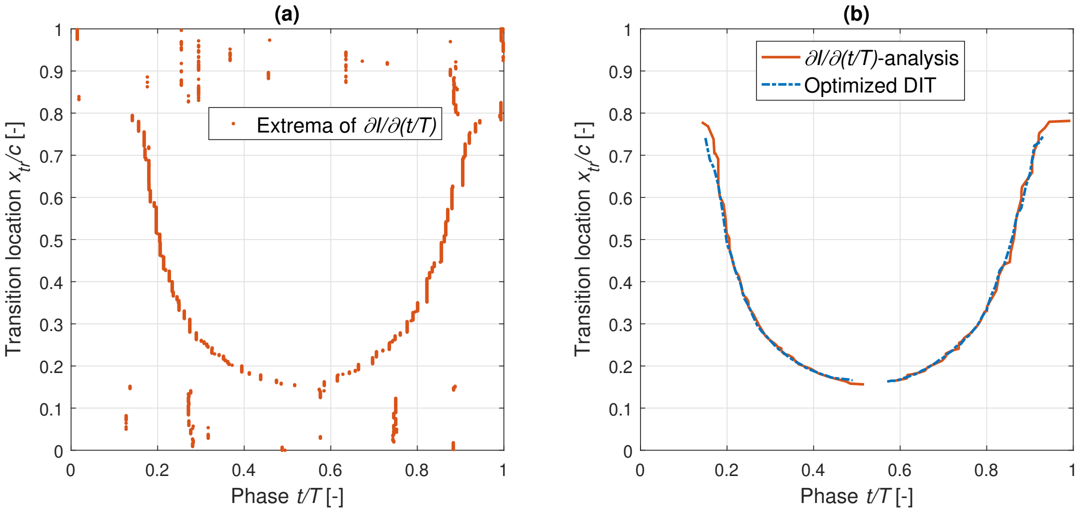

Figure 6.5: (a): Detected extrema in the intensity gradient signal, (b): Filtered transition measurement, in comparison to optimized DIT results for the motion case with $\alpha_1 = 6°$ and $k = 0.075$

The transition measurement results with LIT are shown in Fig. 6.6. The key difference between the LIT and the optimized DIT transition measurement results in Fig. 6.6b is a positive phase shift for DIT of ca. $0.02 < \Delta T < 0.03$, otherwise the results are similar qualitatively to each other. This confirms that LIT is a valid transition measurement technique. Filtered results from the application of LIT to several pitching motion cases are compared to the results from ADIT and σC_p in Sec. 6.2.

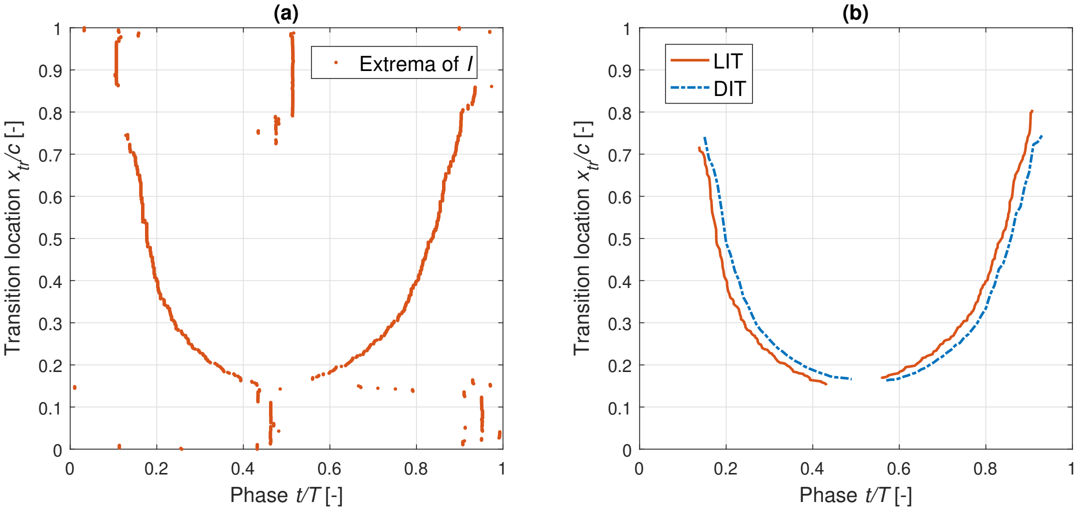

Figure 6.6: (a): Detected extrema in the intensity signal, (b): Filtered LIT transition measurement, in comparison to optimized DIT results for the motion case with α_1 = 6° and $k = 0.075$

The LIT approach can be extended from the previously shown one-dimensional analysis to measuring boundary layer transition on the two-dimensional projection of the model surface. For that, the infrared measurement data processing procedure is adjusted from the analysis of spanwise averaged data to analyzing single pixels. The individual results of the intensity peak detection per pixel are interpolated to a boundary layer transition front by marking each pixel as “transitional” for the determined extremum phase instant over $\pm 1\%$ of the period. Then, the median location of the transitional pixels for each streamwise pixel array is extracted for each frame. Figures 6.7, 6.8 and 6.9 show the boundary layer transition front determined with LIT for three different pitching motion cases. The figures include six graphs each, showing three phase instants t/T on the upstroke (a, c, f) and three t/T on the downstroke (b, d, e). Flow is from left to right, darker regions are cooler and the boundary layer transition front is shown in white. Note that the thickness of the boundary layer transition region in these graphs is arbitrarily selected to be 17 pixels and has no physical meaning. The six example phase instants are selected such that images shown side by side are from the same instantaneous angle of attack. The boundary layer transition fronts measured with LIT reveal that unsteady transition is triggered earlier in the model center and near the fiducial markers, as seen in the static example image in Fig. 3.3. Two observations of the unsteady behavior of the transition front can be made for all three motion cases. The first observation is that the turbulent wedge in the model center is changing considerably in length for different transition locations. When the transition front is near the leading edge, the overall behavior is nearly uniform over the span, and when it is further downstream, the turbulent wedge has a large influence on the qualitative behavior of the transition front. The second observation concerns the differences between up- and downstroke. Considering the phase instants $t/T = 0.15$ (a) and $t/T = 0.85$ (b) for all three motion cases, it can be observed that the turbulent wedge is more pronounced during the upstroke (local transition to turbulence) than during the downstroke (local relaminarization). From the results for $\alpha_1 = 6°$ and $k = 0.075$ shown in Figs. 6.7a and 6.7b, it can be determined that the transition measurement difference between the spanwise region that was used for the one-dimensional analysis schemes and the most upstream transition point is ca. 120 pixels during the upstroke and ca. 70 pixels during the downstroke. While the most upstream transition point is nearly identical in Figs. 6.7a and 6.7b, the transition measurement difference in the evaluated spanwise region differs by ca. 70 pixels or $\Delta x/c \approx 0.09$. Neither of these features of the non-uniform boundary layer transition front, nor the visible surface defects on the airfoil model decrease the effectiveness of the LIT technique for the application on the entire model surface.

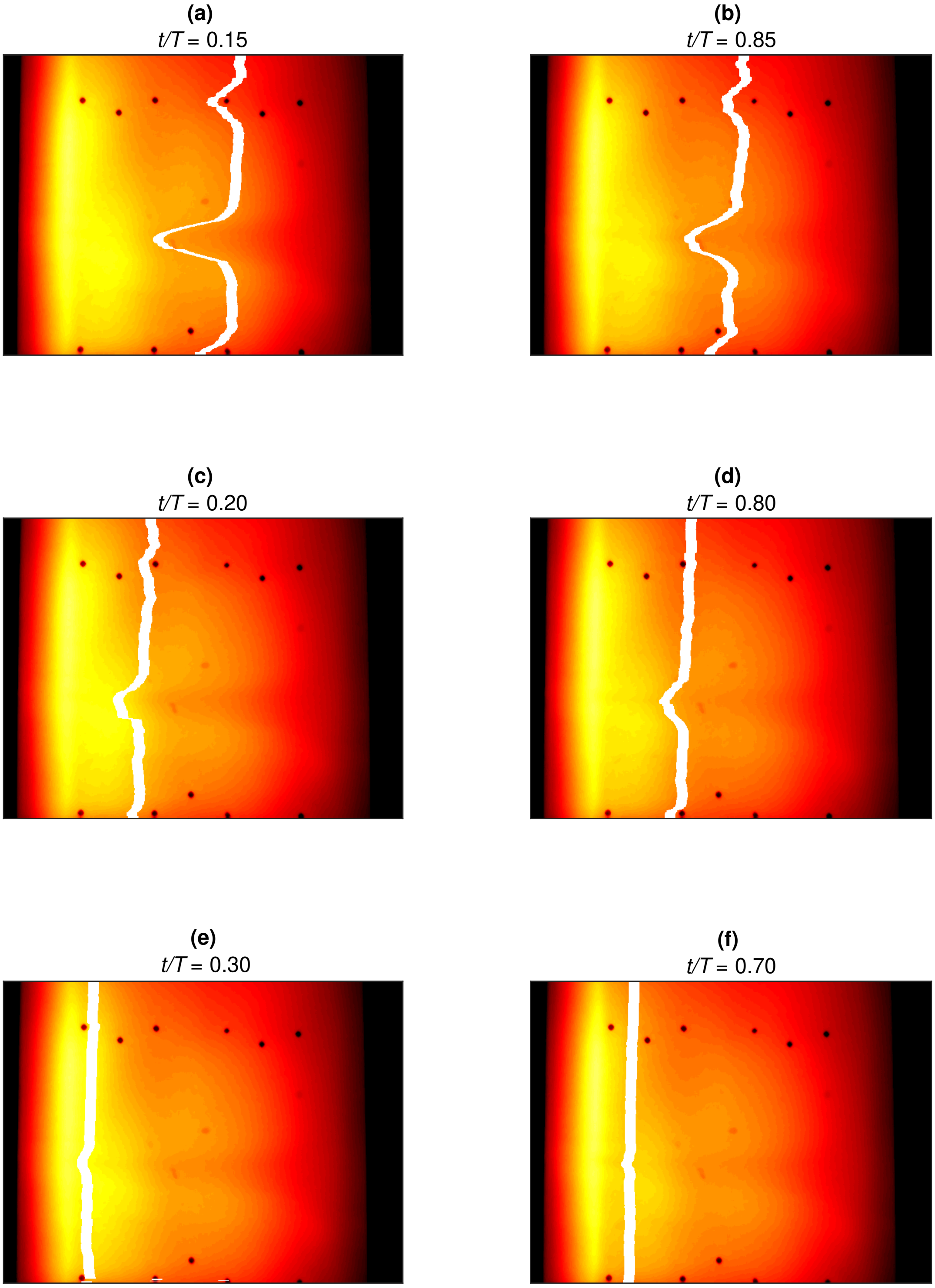

Figure 6.7: Pixelwise application of LIT for the pitching motion case with $\alpha_1 = 6°$ and $k = 0.075$: Two-dimensional unsteady boundary layer transition front measured at six t/T

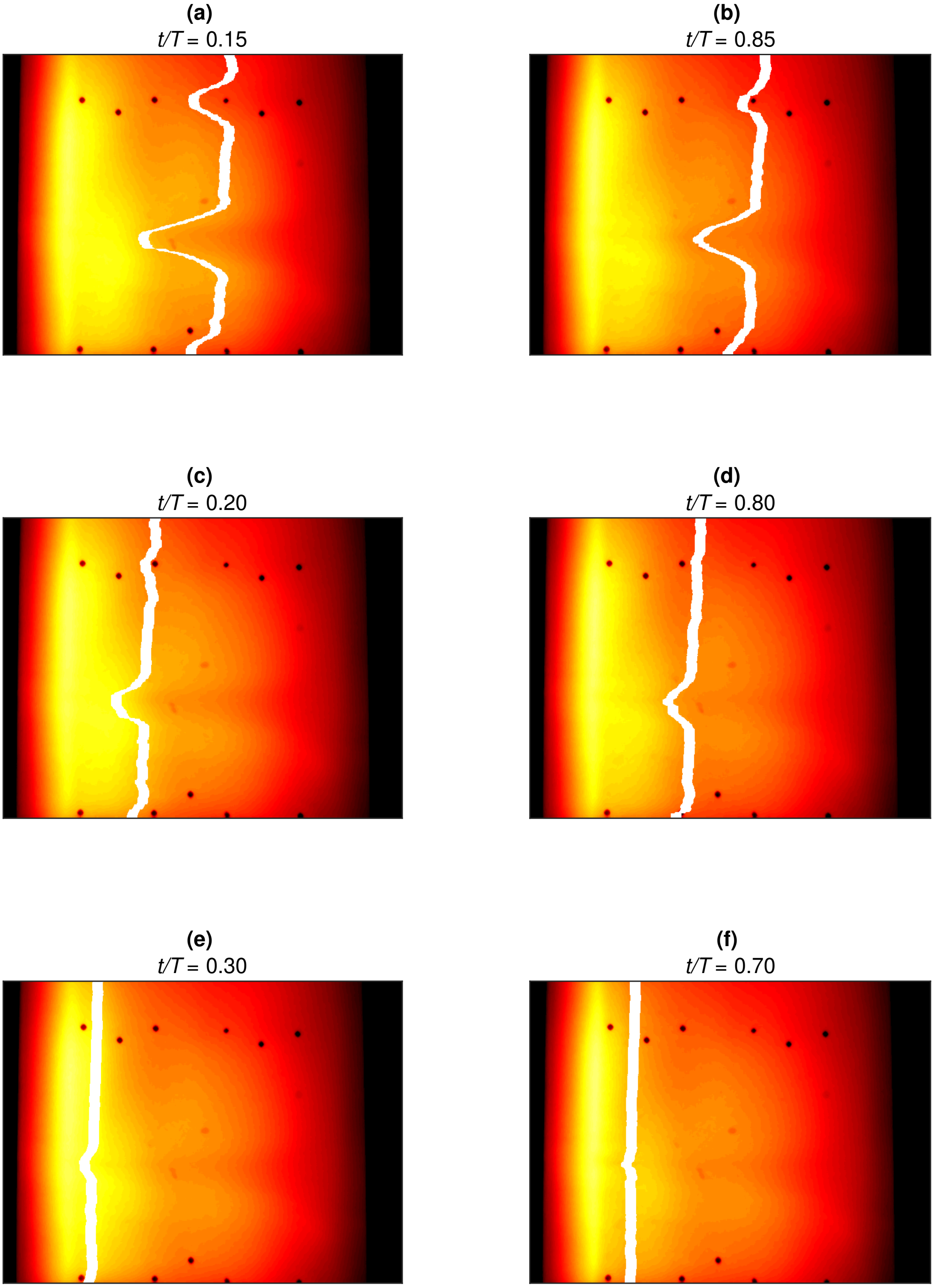

Figure 6.8: Pixelwise application of LIT for the pitching motion case with α_1 = 6° and $k = 0.038$: Two-dimensional unsteady boundary layer transition front measured at six t/T

(a) *t/T* = 0.15 **(b)** *t/T* = 0.85

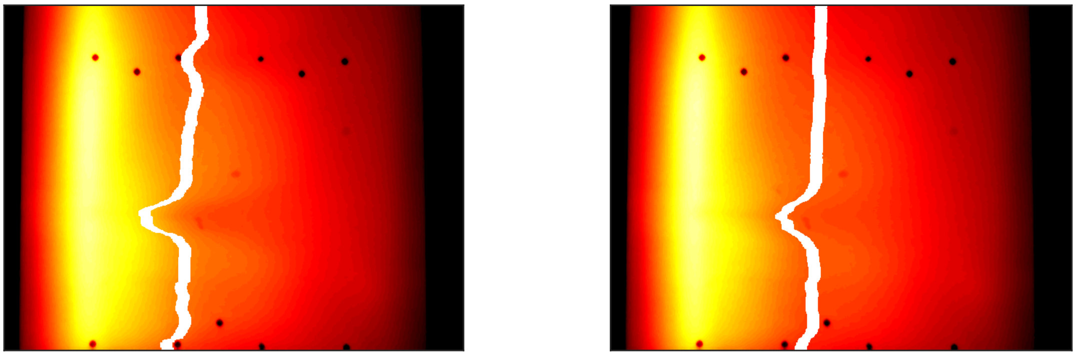

(c) *t/T* = 0.20 **(d)** *t/T* = 0.80

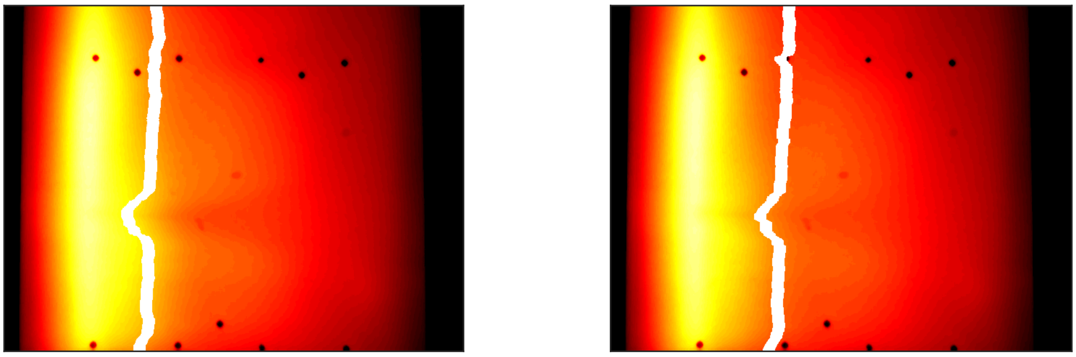

(e) *t/T* = 0.30 **(f)** *t/T* = 0.70

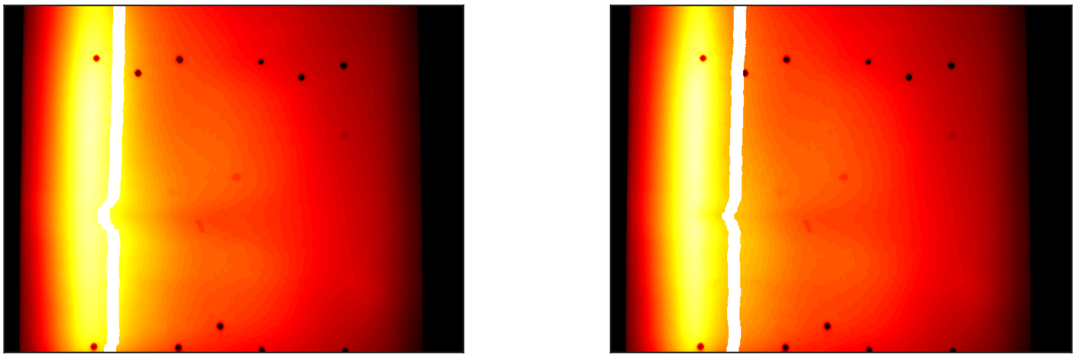

Figure 6.9: Pixelwise application of LIT for the pitching motion case with α_1 = 4° and $k = 0.038$: Two-dimensional unsteady boundary layer transition front measured at six t/T

6.2. Validation with σC_p pressure signal analysis

In Figs. 6.10 to 6.15, the transition measurement results from LIT and ADIT are shown together with reference transition measurements from the fast-response σC_p-technique. The shown results cover the range of pitching motion parameters from $\alpha_1 = 4°$ to $\alpha_1 = 8°$ and from $k = 0.009$ to $k = 0.151$. The six figures each include two graphical representation of the same measurement results, the transition location plotted over phase (a) and in a hysteresis plot over the angle of attack α (b). The hysteresis plots are particularly useful to investigate the frequency effects on the transition measurement results, while the phase plots are more appropriate to investigate the behavior of the transition location during the upstroke and the downstroke separately. Even though a large range of experimental parameters is shown in the graphs, the observations of the differences and similarities between LIT, ADIT and σC_p are similar for all graphs. The following observations are made:

- The σC_p-measurements downstream of $x/c = 0.65$ show a characteristic step compared to the measurements further upstream. This step is observed in all pitching motion cases and produces transition measurements further upstream than expected from a smooth curve during the beginning and end of the motion period near $t/T = 0$. An equivalent effect was observed in the static transition polar in Fig. 3.6.
- The transition measurements from LIT and ADIT show a good qualitative agreement during the upstroke and the downstroke. It is noted that ADIT is able to reproduce the entire transition motion over the phase while LIT is not. Two distinct differences between the LIT and ADIT transition measurements are identified. The LIT measurements lead the ADIT measurements in phase by up to $\Delta t/T = 0.05$ and the measurements from LIT and ADIT show qualitative differences near the motion turning points.
- The comparison of the results from LIT with the reference transition measurements from σC_p suggests that during the upstroke and the downstroke, the measurements from LIT near the motion turning point do not capture the onset of the transition motion in the changed direction. Instead, LIT measures additional transition locations after the motion has stopped on the motion downstroke.
- The LIT measurements lead the σC_p transition points in phase during the downstroke by up to $\Delta T = 0.05$, during the upstroke this phase difference is systematically reduced to $0 < \Delta T < 0.03$.
- The results from ADIT and σC_p are in good qualitative and quantitative agreement. Both techniques reproduce the entire transition movement without exhibiting distinct overall systematic measurement errors and with a small level of random scatter in the data.
- While the measurements from ADIT and σC_p are in excellent agreement for the downstroke, a considerable difference between ADIT and σC_p is observed during the upstroke. A systematic measurement phase lag of around $\Delta T \approx 0.03$ is introduced, which results in a transition measurement difference of up to $\Delta x_{tr}/c \approx 0.07$ during mid-upstroke.

This last point is the most considerable difference between the ADIT transition measurements and the σC_p reference measurements. The phase lag during the motion upstroke causes significant differences in the transition measurement with ADIT and σC_p. A possible explanation for this difference is the variation in the dynamic behavior of the turbulent wedge during the up- and downstroke, which was identified with the two-dimensional implementation of LIT. In these results, it was found that the length of the turbulent wedge is distinctively different during the motion upstroke and the downstroke. In fact, when considering all sources of error for DIT that were analyzed in this study, the non-uniform transition front is the only coherent explanation for this difference between ADIT and σC_p. The truncation error that was found in the quasi-steady DIT model is much smaller in magnitude than the observed difference and it is suggested from the analysis of the numerical simulation data that the systematic phase lag error of DIT is reduced to $\epsilon_{\Delta T} < 0.01$ with ADIT for fast moving transition fronts. As opposed to these small differences, the analysis of the differences in length of the turbulent wedge between up- and downstroke in Sec. 6.1.2 were found to be at the order of magnitude of the transition measurement difference between ADIT and σC_p. To confirm these considerations, a quantitative analysis of the two-dimensional transition front based on the LIT measurements is recommended for future studies.

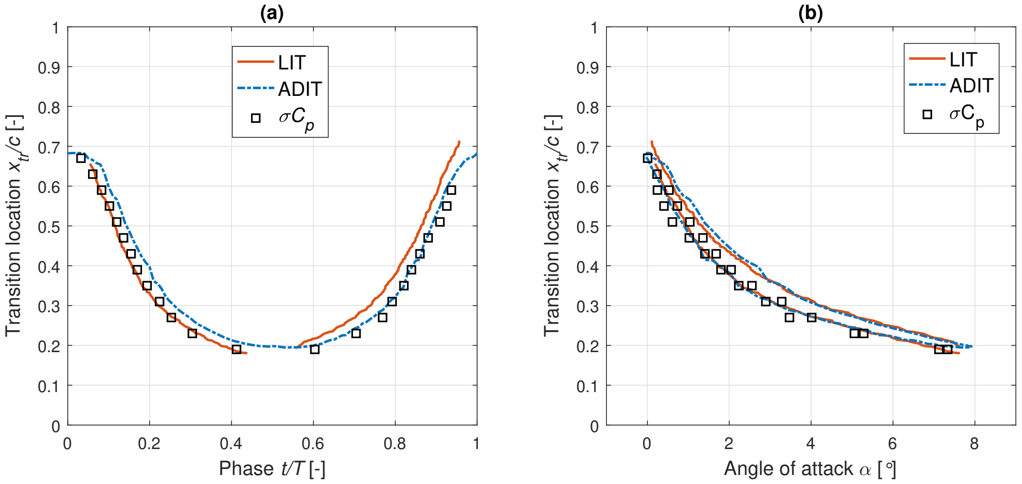

Figure 6.10: Comparison of transition measurements with LIT, ADIT and σC_p for the pitching motion α_1 = 4° and $k = 0.038$

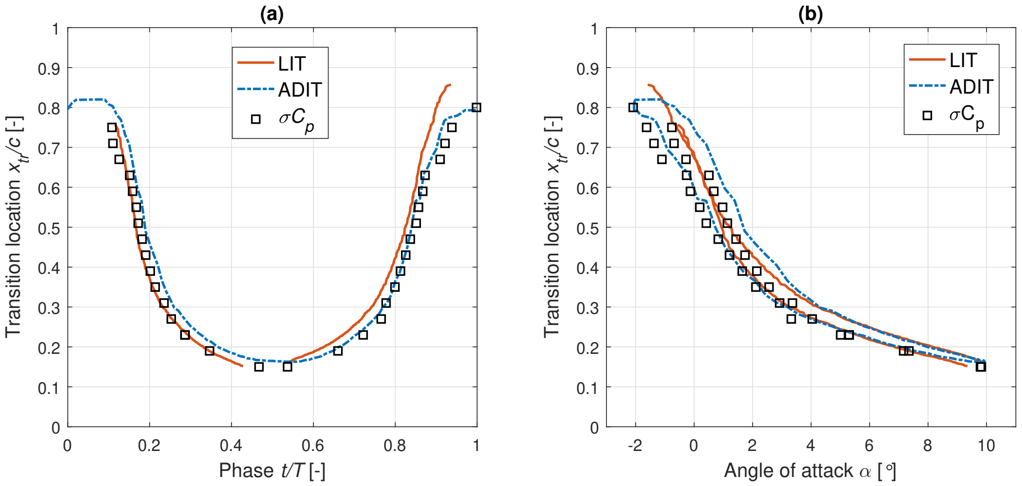

Figure 6.11: Comparison of transition measurements with LIT, ADIT and σC_p for the pitching motion α_1 = 6° and $k = 0.038$

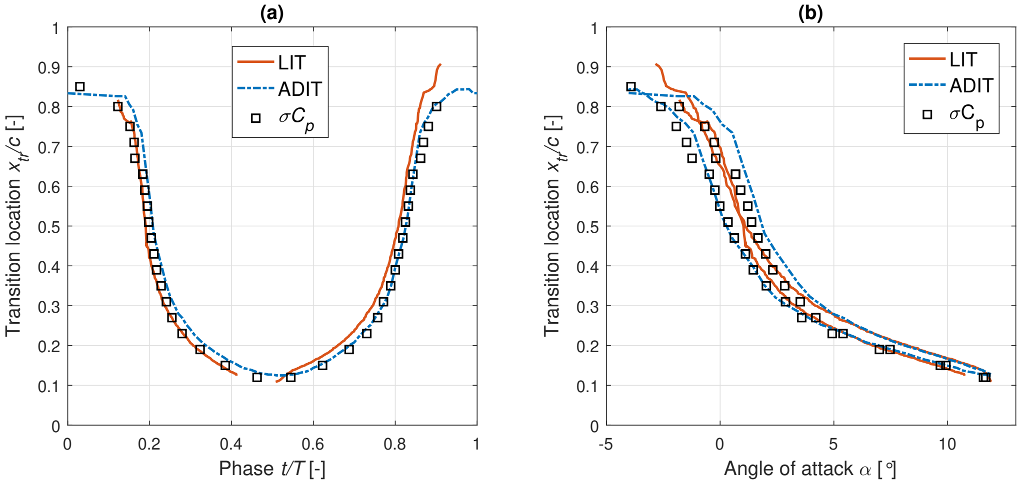

Figure 6.12: Comparison of transition measurements with LIT, ADIT and σC_p for the pitching motion α_1 = 8° and $k = 0.038$

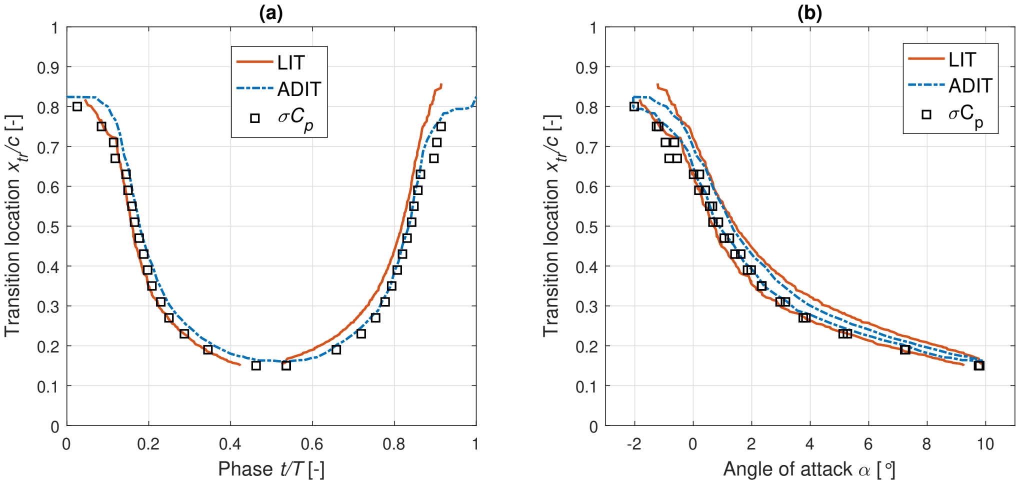

Figure 6.13: Comparison of transition measurements with LIT, ADIT and σC_p for the pitching motion α_1 = 6° and $k = 0.009$

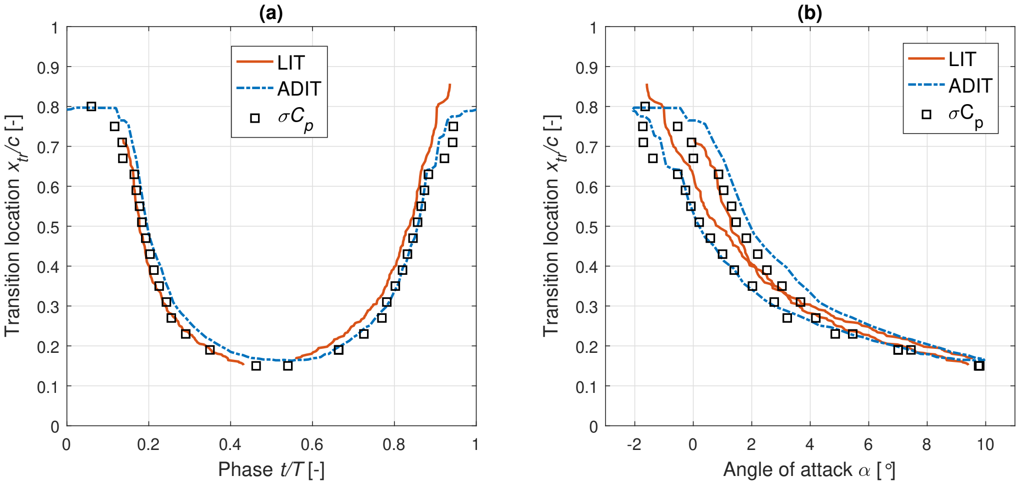

Figure 6.14: Comparison of transition measurements with LIT, ADIT and σC_p for the pitching motion α_1 = 6° and $k = 0.075$

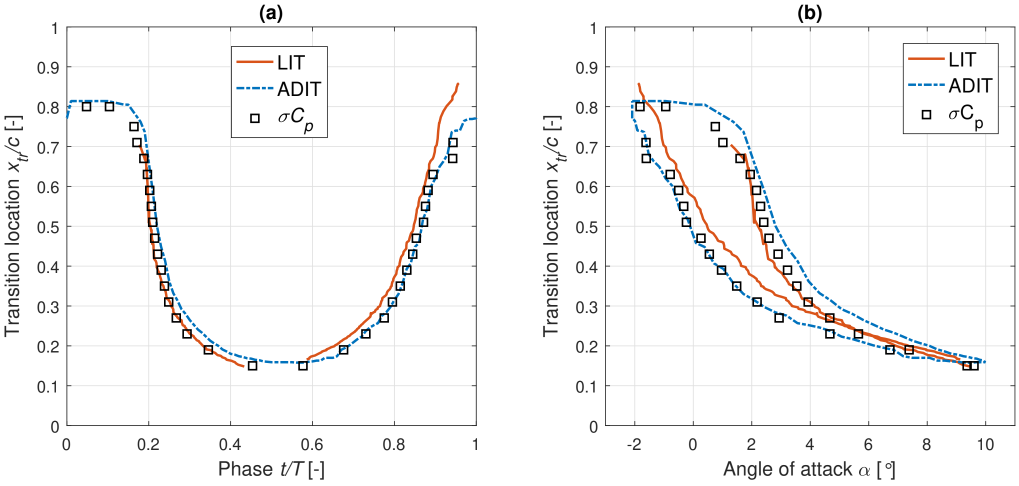

Figure 6.15: Comparison of transition measurements with LIT, ADIT and σC_p for the pitching motion α_1 = 6° and $k = 0.151$

7

Conclusions

In this study, the capabilities of boundary layer transition detection based on infrared thermography measurements in periodic unsteady, subsonic aerodynamic processes have been advanced. First, the established DIT technique was optimized based on recommendations from the literature for an experimental data set. The experimental data was measured with an infrared camera on a pitching airfoil model in an open test section, closed circuit wind tunnel at $Re = 1 \cdot 10^6$ and $Ma = 0.15$ with the range of parameters $1° \leq \alpha_1 \leq 8°$ and $0.25\,\mathrm{Hz} \leq f \leq 8\,\mathrm{Hz}$ (corresponding to $0.005 \leq k \leq 0.151$ and $0.016 \geq Fo \geq 0.0005$) for the pitching motion. The DIT image separation time step $\Delta t/T$ was selected based on the requirement that $\Delta t/T$ should be as small as possible to reduce the systematic transition measurement error of DIT, but large enough to yield a number of valid data points above the noise level. The optimal $\Delta t/T$ for the application of DIT for this setup was found to be typically around $\Delta t/T = 0.01$ for a large range of pitching motion parameters.

As an alternative transition measurement scheme, the individual DIT image separation time step sizes over the period were automatically adapted. With the adaptive DIT approach, $\Delta t/T$ is increased starting from the smallest value until it just exceed the noise threshold. The ADIT approach reduced the transition measurement error of a quasi-steady DIT model compared to the optimized constant time step approach to DIT. In the analysis of results from a numerical simulation, the characteristic phase lag error of DIT could be observed. The ADIT approach was successfully implemented for the simulation data, yielding equivalent transition measurements compared to optimized DIT. Ultimately, the ADIT approach was implemented for the data from the wind tunnel experiment. The experimental results from ADIT were equivalent to the optimized DIT transition measurements for most of the pitching motion period. The ADIT approach exhibited its biggest advantage in being able to measure the fast transition movement with low error and also measure transition in the low-signal region of the downstream turning point. The ADIT transition measurement scheme produces the most accurate and complete transition measurements with infrared thermography and is an improvement over the conventional constant time step DIT.

A second alternative approach to measuring unsteady transition with infrared thermography was developed in this study. Local infrared thermography analyses of the infrared thermography measurements at fixed locations over time, measuring the extrema of the local temperature signals. The temperature signal of the numerical simulation results shows that the surface temperature decreases during the part of motion period where the boundary layer flow is turbulent and increases when the flow is laminar, as expected with the different skin friction levels for the two boundary layer states and Reynolds analogy that connects the skin friction to the convective heat transfer level. Because of the slow temperature response of the airfoil model surface material relative to the motion frequency, the surface temperature does not reach an equilibrium but is continuously increasing and decreasing. Instead of analyzing the peaks of the temperature signal, the extrema of the temporal gradient of the temperature signal can be analyzed as well. The gradient shows two distinct peaks on the up- and downstroke. The transition measurement based on these peaks was found to be equivalent to the result obtained from DIT with a small image separation time step.

The LIT approach was transferred from the numerical simulation data to the experimental data and provides a valid unsteady boundary layer transition measurement result. It was demonstrated that the LIT technique can be extended from the analysis of a streamwise intensity vector to a pixelwise application, hence measuring unsteady boundary layer transition on the two-dimensional projection of the entire model surface. LIT is computationally cheaper than the peak detection of the intensity gradient or DIT, and it is therefore suited best for the application on the entire model surface. Several observations of the two-dimensional behavior of the transition front could be made. In particular, the dynamics of the turbulent wedge in the airfoil model center were observed to vary significantly between up- and downstroke of the motion and for different streamwise positions of the transition front. The LIT technique exploits the key advantage of infrared thermography over the fast-response discrete sensor techniques for measuring unsteady boundary layer transition; the spatial resolution. Therewith, LIT allows the examination of the unsteady two-dimensional behavior of the boundary layer transition front in a level of detail that could not be measured with any other technique before.

The overall agreement of the ADIT results with reference measurements from σC_p is very good. The agreement of LIT with σC_p is fair, the major difference is a phase lead, which is expected from the LIT methodology. The largest difference between ADIT and σC_p was found to be a phase lag of ADIT that is observed only during the pitching motion upstroke. This difference could be explained with the varying length of the turbulent wedge, using the measurements of the two-dimensional transition front with LIT.

To put this study into the context of the relevant research field, it is useful to refer back to the research question: *“Can the unsteady boundary layer transition location on a pitching airfoil model be determined efficiently under various motion amplitude and frequency conditions by using infrared thermography?”* The first part of the answer is that no detrimental effects for performing DIT or LIT were found in the examined range of pitching motion parameters. The analysis of the experimental data with DIT was automated with an elaborate post-processing algorithm. The DIT technique was optimized based on recommendations from the literature. The agreement of DIT with the fast-response measurement technique σC_p is given with small remaining differences. Additionally, this study resulted in two new measurement schemes for unsteady transition with infrared thermography. The adaptive approach to DIT produced the best combined spatial and temporal measurements of unsteady boundary layer transition on a pitching airfoil in very good agreement with results from the σC_p-technique. The LIT approach resulted in measurements of the two-dimensional transition front that are a considerable advancement over any other available transition measurement technique. The analysis of these measurements delivers a sound explanation for the remaining differences between the results from DIT and σC_p. In the future, the improved transition measurement schemes using infrared thermography can be scaled from the simplified aerodynamic problem of this study to the full-scale helicopter rotor. For this, flight experiments have been conducted at the DLR in Braunschweig in June 2018.

Figure 7.1: Flight experiments with two helicopters for unsteady boundary layer transition measurements on the main rotor of the *EC 135*, conducted at DLR Braunschweig in June 2018

Bibliography

[1] I. H. Abbott and A. E. von Doenhoff. *Theory of Wing Sections: Including a Summary of Airfoil Data*. Dover Books on Aeronautical Engineering. Dover Publications, 1959.

[2] D. P. Aeschliman, R. H. Croll, and D. W. Kuntz. Shear-stress-sensitive liquid-crystals for hypersonic boundary-layer transition detection. *Journal of Spacecraft and Rockets*, 32(5):749–757, 1995.

[3] K. Asai, H. Kanda, T. Kunimasu, T. S. Liu, and J. P. Sullivan. Boundary-layer transition detection in a cryogenic wind tunnel using luminescent paint. *Journal of Aircraft*, 34(1):34–42, 1997.

[4] T. Astarita and G. M. Carlomagno. *Infrared thermography for thermo-fluid-dynamics*. Experimental Fluid Mechanics Series. Springer Berlin Heidelberg, 2012.

[5] T. Astarita, G. Cardone, and G. M. Carlomagno. Spiral vortices detection on a rotating disk. In *Proceedings of the 23rd Congress of the International Council of the Aeronautical Sciences*, pages 364.1–364.8, Toronto, Canada, September 2002.

[6] F. Avallone, F. F. J. Schrijer, and G. Cardone. Infrared thermography of transition due to isolated roughness elements in hypersonic flows. *Physics of Fluids*, 28(2):024106, 2016.

[7] H. Blasius. Grenzschichten in Flüssigkeiten mit kleiner Reibung. *Zeitschrift für Mathematik und Physik*, 56(1):1–37, 1908.

[8] J. M. Brandon, G. S. Manuel, R. E. Wright, and B. J. Holmes. In-flight flow visualization using infrared imaging. *Journal of Aircraft*, 27(7):612–618, 1990.

[9] C. Brücker, J. Spatz, and W. Schröder. Feasability study of wall shear stress imaging using microstructured surfaces with flexible micropillars. *Experiments in Fluids*, 39(2):464–474, 2005.

[10] D. S. Bynum, F. K. Hube, C. M. Key, and P. M. Dyer. Measurement and mapping of aerodynamic heating in VKF tunnel B with an infrared camera. Technical Report AEDC-TR-76-54, Arnold Engineering Development Center, 1976.

[11] G. M. Carlomagno and G. Cardone. Infrared thermography for convective heat transfer measurements. *Experiments in Fluids*, 49(6):1187–1218, 2010.

[12] C. J. Chocol. Remote infrared imagery of shuttle during entry. In *Proceedings of the Joint Automatic Control Conference*, pages 251–255, Denver, Colorado, June 1979. American Institute of Chemical Engineers.

[13] A. Dhungel, Y. Lu, W. Phillips, S. V. Ekkad, and J. Heidmann. Film cooling from a row of holes supplemented with antivortex holes. *Journal of Turbomachinery*, 131(2):021007, 2009.

[14] N. S. Dougherty Jr. Influence of wind tunnel noise on the location of boundary-layer transition on a slender cone at mach numbers from 0.2 to 5.5. Technical Report AEDC-TR-78-44, Arnold Engineering Development Center, 1980.

[15] H. Dowell. *A Modern Course in Aeroelasticity*. Solid Mechanics and Its Applications. Springer Berlin Heidelberg, 5th edition, 2014.

[16] C. Eder. *Analyse der Differenz-Infrarotthermographie*. Master's thesis, Universität der Bundeswehr München, 2016.

[17] Y. W. Gao, Q. L. Zhu, and L. Wang. Measurement of unsteady transition on a pitching airfoil using dynamic pressure sensors. *Journal of Mechanical Science and Technology*, 30(10):4571–4578, 2016.

[18] A. D. Gardner and K. Richter. Boundary layer transition determination for periodic and static flows using phase-averaged pressure data. *Experiments in Fluids*, 56(6):119, 2015.

[19] A. D. Gardner, C. C. Wolf, and M. Raffel. A new method of dynamic and static stall detection using infrared thermography. *Experiments in Fluids*, 57(9):149, 2016.

[20] A. D. Gardner, C. Eder, C. C. Wolf, and M. Raffel. Analysis of differential infrared thermography for boundary layer transition detection. *Experiments in Fluids*, 58(9):122, 2017.

[21] E. Gartenberg and A. S. Roberts. Twenty-five years of aerodynamic research with infrared imaging. *Journal of Aircraft*, 29(2):161–171, 1992.

[22] E. Gartenberg and R. E. Wright. Boundary-layer-transition detection with infrared imaging emphasizing cryogenic applications. *AIAA Journal*, 32(9):1875–1882, 1994.

[23] M. Grawunder, R. Ress, and C. Breitsamter. Thermographic transition detection for low-speed wind-tunnel experiments. *AIAA Journal*, 54(6):2012–2016, 2016.

[24] C. C. Heister. Laminar-turbulent transition prediction for helicopter rotors in hover and forward flight – a RANS based investigation of transition mechanisms using empirical criteria. In *38th European Rotorcraft Forum*, Amsterdam, Netherlands, September 2012.

[25] FLIR Systems Inc. FLIR SC7000 Series. `http://www.flir.co.uk/science/display/?id=50093`, Accessed on 30.06.2018.

[26] F. P. Incropera, D. P. DeWitt, T. L. Bergman, and A. S. Lavine. *Fundamentals of Heat and Mass Transfer*. John Wiley & Sons Inc., 6th edition, 2007.

[27] A. Kus, S. Schneider, M. Hollands, R. Rammer, O. Dieterich, and M. Priems. GRC1: An advanced five-bladed bearingless main rotor – dynamics and acoustics from draft to flight test. In *74th AHS Forum*, Phoenix, Arizona, May 2018. American Helicopter Society.

[28] T. Lee and S. Basu. Measurement of unsteady boundary layer developed on an oscillating airfoil using multiple hot-film sensors. *Experiments in Fluids*, 25(2):108–117, 1998.

[29] J. G. Leishman. *Principles of Helicopter Aerodynamics*. Cambridge aerospace series. Cambridge University Press, 2nd edition, 2006.

[30] L. M. Mack. Boundary-layer linear stability theory. Technical Report AGARDograph 709, Advisory Group for Aerospace Research and Development, 1984.

[31] W. J. McCroskey. Unsteady airfoils. *Annual Review of Fluid Mechanics*, 14(1):285–311, 1982.

[32] C. Mertens, C. C. Wolf, and A. D. Gardner. Unsteady boundary layer transition detection with local infrared thermography. In *21st DGLR STAB symposium*, Darmstadt, Germany, November 2018. Deutsche Gesellschaft für Luft- und Raumfahrt.

[33] C. B. Merz, C. C. Wolf, K. Richter, K. Kaufmann, A. Mielke, and M. Raffel. Spanwise differences in static and dynamic stall on a pitching rotor blade tip model. *Journal of the American Helicopter Society*, 62(1), 2017.

[34] D. J. Monson, G. G. Mateer, and F. R. Menter. Boundary-layer transition and global skin friction measurement with an oil-fringe imaging technique. Technical Report 932550, Society of Automotive Engineers, 1993.

[35] J. A. Noble and D. E. Boylan. Heat-transfer measurements on a 5-deg sharp cone using infrared scanning and on-board discrete sensor techniques. Technical Report AEDC-TSR-78-V51, Arnold Engineering Development Center, 1978.

[36] A. Overmeyer, J. T. Heineck, and C. C. Wolf. Unsteady boundary layer transition measurements on a rotor in forward flight. In *74th AHS Forum*, Phoenix, Arizona, May 2018. American Helicopter Society.

[37] D. J. Peake, A. J. Bowker, S. J. Lockyear, and F. Ellis. Non-obtrusive detection of transition region using an infra-red camera. In *AGARD CP 224, Symposium on Laminar-Turbulent Transition*, Lyngby, Denmark, May 1977. Advisory Group for Aerospace Research and Development.

[38] L. Prandtl. Über Flüssigkeitsbewegung bei sehr kleiner Reibung. In *III. Internationaler Mathematiker-Kongress*, Leipzig, 1905. B. G. Teubner Verlag.

[39] M. Raffel and C. B. Merz. Differential infrared thermography for unsteady boundary-layer transition measurements. *AIAA Journal*, 52(9):2090–2093, 2014.

[40] M. Raffel, C. B. Merz, T. Schwermer, and K. Richter. Differential infrared thermography for boundary layer transition detection on pitching rotor blade models. *Experiments in Fluids*, 56(2):30, 2015.

[41] R. Ricci and S. Montelpare. A quantitative IR thermographic method to study the laminar separation bubble phenomenon. *International Journal of Thermal Sciences*, 44(8):709–719, 2005.

[42] K. Richter and E. Schülein. Boundary-layer transition measurements on hovering helicopter rotors by infrared thermography. *Experiments in Fluids*, 55(7):1755, 2014.

[43] K. Richter, S. Koch, A. Goerttler, B. Lütke, C. C. Wolf, and A. Benkel. Unsteady boundary layer transition on the DSA-9A rotor blade airfoil. In *Proceedings of the European Rotorcraft Forum 2015*, Munich, Germany, September 2015.

[44] K. Richter, C. C. Wolf, A. D. Gardner, and C. B. Merz. Detection of unsteady boundary layer transition using three experimental methods. In *54th AIAA Aerospace Sciences Meeting*, San Diego, California, January 2016. American Institute of Aeronautics and Astronautics.

[45] M. Röger. A periodic-transient method for high-resolution heat transfer measurement on two-dimensional curved surfaces. *Journal of Heat Transfer*, 129(12):1638–1654, 2007.

[46] P. Sagaut. *Large Eddy Simulation for Incompressible Flows: An Introduction*. Scientific Computation series. Springer Berlin Heidelberg, 1st edition, 2013.

[47] H. Schlichting and K. Gersten. *Boundary-Layer Theory*. Springer Berlin Heidelberg, 10th edition, 2016.

[48] E. Schülein. Experimental investigation of laminar flow control on a supersonic swept wing by suction. In *4th Flow Control Conference*, Seattle, Washington, June 2008. American Institute of Aeronautics and Astronautics.

[49] D. W. Stallings and D. B. Carver. Infrared and phase-change paint measurements of heat-transfer on the space shuttle orbiter. Technical Report AEDC-TSR-78-V13, Arnold Engineering Development Center, 1978.

[50] T. Theodorsen. General theory of aerodynamic instability and the mechanism of flutter. Technical Report 496, National Advisory Committee for Aeronautics, 1935.

[51] H. Thomann and B. Frisk. Measurement of heat transfer with an infrared camera. *International Journal of Heat and Mass Transfer*, 11(5):819–826, 1968.

[52] W. Tollmien. Über die Entstehung der Turbulenz. 1. Mitteilung. In *Nachrichten von der Gesellschaft der Wissenschaften zu Göttingen*. Weidmannsche Buchhandlung Berlin, 1929.

[53] C. Tropea (Editor), A. L. Yarin (Editor), and J. F. Foss (Editor). *Springer Handbook of Experimental Fluid Mechanics*. Springer Handbooks. Springer Berlin Heidelberg, 2007.

[54] J. L. van Ingen. The e^N method for transition predicition. Historical review of work at TU Delft. In *Proceeding of the 38th Fluid Dynamics Conference and Exhibit*, Seattle, Washington, June 2008. American Institute of Aeronautics and Astronautics.

[55] S. von Hoesslin, M. Stadlbauer, J. Gruendmayer, and C. J. Kähler. Temperature decline thermography for laminar-turbulent transition detection in aerodynamics. *Experiments in Fluids*, 58 (9):129, 2017.

[56] T. von Kármán and W. R. Sears. Airfoil theory for non-uniform motion. *Journal of the Aeronautical Sciences*, 5(10), 1938.

[57] F. M. White. *Viscous Fluid Flow*. Series in Mechanical Engineering. McGraw-Hill, 3rd edition, 2006.

[58] WMF Wikimedia Foundation. Bo105 rotor head, published under the creative commons license. `https://commons.wikimedia.org/wiki/File:Bo105_Rotorkopf_0570b.jpg`, 2007.

[59] C. C. Wolf, C. Mertens, A. D. Gardner, C. Dollinger, and A. Fischer. Optimisation of differential infrared thermography for unsteady boundary layer transition measurement. In *44th European Rotorcraft Forum*, Delft, Netherlands, September 2018.

[60] S. Zuccher and W. S. Saric. Infrared thermography investigations in transitional supersonic boundary layers. *Experiments in Fluids*, 44(1):145–157, 2008.